Summer 2019

On the performance of X-band dual-polarization radar-rainfall estimation algorithms during the SMAPVEX-16 field campaign

John R. Brammeier
University of Iowa

ON THE PERFORMANCE OF X-BAND DUAL-POLARIZATION RADAR-RAINFALL ESTIMATION ALGORITHMS DURING THE SMAPVEX-16 FIELD CAMPAIGN

by

John R. Brammeier

A thesis submitted in partial fulfillment
of the requirements for the Master of Science
degree in Civil and Environmental Engineering in the
Graduate College of
The University of Iowa

August 2019

Thesis Supervisor: Professor Witold F. Krajewski

ACKNOWLEDGEMENTS

A special thanks goes out to all members of the Iowa Flood Center, and IIHR, who navigate the state's political currents and work tirelessly to improve safety and quality of life of everyday Iowans like myself. I have learned indispensable skills from my time here so far, and I deeply appreciate the help and community available in this lab.

The notable efforts of Witek Krajewski, Larry Weber, and Joe Bolkcom to keep the Iowa Flood Center well-represented at the State house never ceases to impress me, and I appreciate the time they submit for the people of Iowa. To the many wonderful international students working at the IFC, thank you for sharing your cultures and perspectives with me. If you decide to stay, I hope you are able to find your unique piece of the American dream. If you decide to return home, I'm sure you will find success there as well.

Finally, a special thank-you to Radek Goska, the man who has four kids, and no time, but managed to teach me more about computer programming than anyone, as well as being a good friend to chat with.

ABSTRACT

Soil moisture estimates from space on a continuous spatial domain could afford researchers with insight about agricultural productivity, flood vulnerability, and biological processes. To evaluate satellite soil moisture estimates, the SMAPVEX-16 experiment was one of a suite of verification data collection campaigns for NASA's Soil Moisture Active Passive satellite. Soil moisture and its role in rainfall partitioning are of great interest to researchers at the Iowa Flood Center [IFC], which was founded in Iowa City, Iowa after a devastating flood event in 2008. A network of two dual-pol capable X-band radar units owned by the IFC, as well as five tipping bucket rain gauges, complemented by 15 from the USDA's Agricultural Research Service were deployed in Central Iowa from May to August 2016 to monitor precipitation on a fine spatiotemporal domain. The data from this particular experiment was analyzed.

Several radar-rainfall algorithms were assembled with a focus on assimilating multivariate radar data. Different variables allow researchers to overcome problems due to signal attenuation by X-band radars, and process radar observations into rainfall accumulations by several methods popular in the literature. Special techniques for accumulating instantaneous rainfall rates at discrete observation intervals were employed to account for the movement of storms. The rain totals between the observation points were estimated and the accumulations were compared to the rain gauge totals.

Methods of rain rate calculation that assimilate many sources of data, such as radar reflectivity, differential reflectivity, and specific differential phase shift yielded the best results.

PUBLIC ABSTRACT

Soil moisture can be estimated from space, but when NASA sends a multi-million dollar investment up there, they need a way to test the quality of their results. A field campaign was devised to estimate one of the biggest factors for soil moisture, rainfall, over Central Iowa in the growing season of 2016. A network of radar units from the University of Iowa was deployed to measure the precipitation near the ground during this time in support of the verification efforts of NASA's Soil Moisture Active-Passive satellite. The radar network employed offers a unique flexibility in scanning capability, mobility, and affordability, which could someday help small watersheds or urban areas with detection and prediction of flash flood events.

Rainfall was estimated by several unique methods converting radar measurements, with care taken to correct for the effects of signal weakening due to hail and heavy rain. This report discusses the qualities of each method, and how they compare to ground-based data from rain gauges, which were densely stationed across the experimental domain. Recommendations are made as to which products and methods to use, accordingly, the best results come from methods that assimilate several sources.

TABLE OF CONTENTS

LIST OF FIGURES

LIST OF TABLES

1. INRODUCTION

Although precipitation is a vital component of the hydrologic cycle, contributing heavily to deadly floods, or stable production of crops, it is difficult to measure on a continuum in space and time. Satellite and radar products exploit our knowledge of electromagnetic scattering to infer the presence of raindrops in a dielectric medium. However, these are costly undertakings, and the cost requires compromises to be made, especially with the Next Generation Radar Weather Surveillance Radar 1988 Doppler network [NEXRAD WSR 88-D]. The chosen parameters and scale of the NEXRAD network must successfully provide information to identify severe weather near any of the locations under its domain.

Flooding, however annually threatens both urban and rural areas, but the NEXRAD network is not optimally suited for capturing hydrologic input from precipitation on a scale relevant to urban areas or small watersheds. The spatial resolution of these radars is limited by the carrier frequency, and the temporal resolution of precipitation products is limited by the National Weather Service's required scan angles during rainfall. Moreover, in mountainous or crowded urban areas, beam blockage creates areas of the radar domain where no hydrologic information is visible. This is problematic for hydrologists because in order to model a stream or river, hydrologic variables should be observed at all points over the stream watershed. Toward that point, the farther a radar beam has to travel to the maximum observing range, the more opportunity for obstruction by signal attenuation, ground clutter, or partial beam blockage. Finally, the WSR-88D is immobile, with a 30-ft antenna, mounted on a tall tower. These problems can be mitigated by a denser network of radars which (1) have no mandatory scans; (2) observe rainfall close to the ground level; (3) can be moved to new locations; and (4) cost less than current radar networks.

This is why the University of Iowa was motivated to propose and purchase a small network of X-band mobile radar units for hydrologic monitoring. These radars supply researchers with exciting opportunities to visualize rainfall fine spatial resolution, fine temporal resolution, and near-ground-level observations. They are also mobile, and can be assembled in any way to fit the terrain, or visibility needs. These radars were involved in two high-profile NASA-Sponsored campaigns, where their ruggedness and reliability was evaluated [IFloods, and SMAP-VEX16]. Data from these campaigns were collected processed, and compared to other references like ground-based rain gauges, S-band radar units, and video disdrometers.

While these radars provide finer detail, which is good for small watersheds and urban areas, the higher carrier frequency introduces problems with signal attenuation due to the scattering interactions between these waves and hydrometeors. Attenuation in this context refers to the tendency of a slightly conducting dielectric medium to take energy from incoming electromagnetic waves, causing the reflected or backscattered electric field amplitude to decrease upon scattering. This is not because of any mechanical or electrical defect of the radar, but a product of the traveling radar pulse and the propagation medium itself. However, amplitude-based products are not the only available products for estimating rainfall. Using dual-polarization capabilities, one can use the differential propagation phase shift to infer characteristics about raindrops in a particular resolution pixel of the radar beam. The scattering effects responsible for attenuating the radar beam do not affect the differential propagation phase shift. Conveniently, ground obstacles like towers, trees, or vehicles do not affect differential propagation phase shift either.

With these issues in mind, this thesis will assemble an algorithm to estimate rainfall by limiting the impact of signal attenuation, utilizing methods of data assimilation, merging information from multiple radars into one grid, and calibrating the radar instruments. Data from disdrometers was used to estimate theoretical parameters of the storm itself. Also, a platform for algorithm comparison is introduced, using radar and gauge data from the campaigns, and projecting them onto a geo-spatial map interface.

This thesis will be concerned with processing algorithms, which invert reflected power from hydrometeors into estimates of rainfall rate. The simplified underlying requirements of a radar processing algorithm will be laid out, followed by a description of the SMAPVEX-16 field campaign, where environmental data was collected for comparison with rain gauge estimates of rainfall accumulation. Next, a more detailed discussion of which products are most relevant and applicable to rainfall estimation is provided. The results of the data analysis from the field campaign will be introduced, as well as discussion about which algorithm generated the most reliable, least biased, and accurate estimates of rainfall accumulation. Effort was made to keep the discussion more general in the main body of the thesis, but if the reader would like descriptions of radiation scattering, subroutines involved in the algorithm, or the interactive radar browser, discussion of these specific topics are in the appendix.

2. OVERVIEW OF THE X-BAND RADAR-RAINFALL ALGORITHM

Although X-band radar units are less costly, and offer fine spatial resolution, and flexible scanning sectors, the development of an algorithm for estimating rainfall should account for some limitations, which are specific to X-band.

At X-band frequency especially, the scattering behavior of raindrops must be well understood, and potential challenges anticipated. The first chapter of the Appendix dives into the specifics of how radar waves scatter from raindrops, but for general discussion of radar algorithms, it is imperative to understand Rayleigh scattering. The Rayleigh scattering regime comes from optical physics, and is the basis for assumptions made when processing radar data. The assumptions from Rayleigh scattering have implications in the size and magnitude of an abstract quantity called the "backscattering cross section". The backscattering cross section of a hydrometeor sounds like a bland, generic term, but Figure 2.1 attempts to provide a visual representation of what it means. The important difference between the two scattering regimes in Figure 2.1 is the amount of energy scattered back in the direction of the incoming radar pulse.

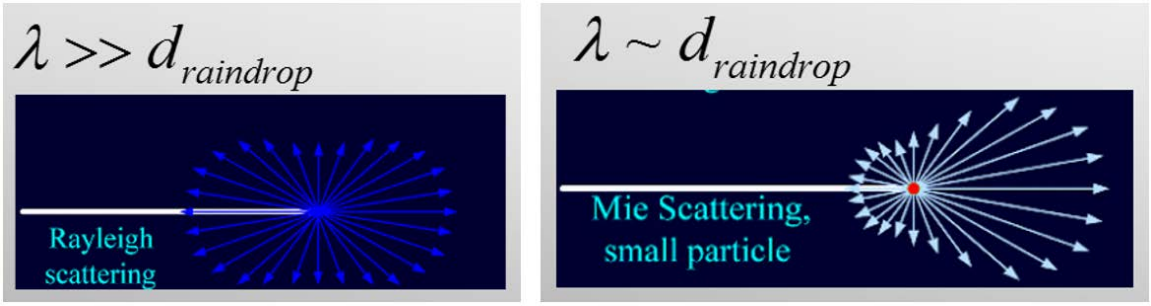

Figure 2.1: Two relevant scattering regimes for radar algorithms.

For Rayleigh scattering, the amount of power reflected back is generally the same as that which is scattered forward. Also, the power reflected is related by a power law to the diameter of the scattering body. This is expressed in mathematical terms in equation A.1.11. When Rayleigh

scattering is not present, then Mie scattering is the governing process, and significantly less power is scattered back to the radar. In radar meteorology, Mie scattering usually takes control when raindrop sizes are more than 1/10 the radar pulse's wavelength (Doviak and Zrnic 2006). The mathematical description of Mie scattering has been analytically solved, but it is much more complicated and tedious, relying on infinite series of coefficients. The X-band radars at the Iowa Flood Center have a carrier wavelength of 3.1 cm. Doviak and Zrnic point out that large raindrops can reach sizes between 3 and 5 mm, so Mie scattering is troublesome for the Xpol units. This is why radar moments based solely on the amplitude of the returning signal are not reliable at X-band.

Therefore, the algorithms in this thesis rely on methods that assimilate data from multiple measurements of the same storm conditions. Whether it is attenuation correction procedures, estimation of differential phase shift, or eventually rainfall rate estimation, data assimilation is necessary for every X-band radar algorithm. One popular way to do this is utilize polarization diversity. In other words, some radars account for the horizontal component of the reflected power as well as the vertical component. Although this chapter is meant to be a general explanation of some radar concepts relevant to building a radar-rain fall algorithm, a refresher on dual-polarization techniques are discussed in Appendix A, particularly Figures A.2 and A.3.

Dual polarization at X-band provides a different suite of radar moments. A critical dual-pol moment for masking non-meteorological echoes, such as wind turbines, or ground clutter is the cross-polar correlation coefficient. In the context of the S-band radar, its popular use is identifying tornadic debris signatures, since the debris produces more diverse signal characteristics than raindrops (Doviak and Zrnic 2006).

However, it is not directly used for calculating rainfall rate, so it is not extensively discussed in this thesis, but it is useful for identifying the ground, or human-built structures, as opposed to raindrops. It also differentiates frozen precipitation from liquid. Figure A.2.1 provides a flowchart illustrating the role of the cross-polar correlation coefficient for the Xpol radar units.

It finds use in the X-band algorithms by data masking. Since returns from ground objects are always from the same location, they cause a bias in rainfall estimation over time, therefore it is vital to identify and deal with them.

The most important dual-pol moment for X-band is differential propagation phase shift, or Φ_{dp}. Since this product is determined by the relative phase difference between horizontal and vertically-polarized radar beams it is independent of amplitude, and therefore said to be immune to attenuation and Mie scattering effects (Sachidananda and Zrnic 1986). The only requirement is that a signal returns to the radar without complete extinction. Because of how Φ_{dp} resists attenuation, it is popular as a reference for correcting attenuation, and estimating true reflectivity, or estimating rainfall directly.

Differential phase shift, although it is useful at X-band, brings its own suite of obstacles. Since X-band radars often encounter situations where Rayleigh scattering is violated by the real-world conditions, Mie scattering effects must be filtered from Φ_{dp}. Hubbert and Bringi (1995), Testud et al. (2000), Bringi and Chandresekar (2001), Anagnostou et al. (2004), and Schneebeli and Berne (2012) all offered potential solutions to this filtering problem. The backscatter differential phase shift is not as directly related to hydrometeor shape and size as the propagation phase shift, so it creates a bias in rainfall estimates. Filtering of differential phase data is therefore included in each algorithm within this thesis. This is done practically in one of a few ways. Hubbert and Bringi (1995) recommended a set of coefficients for a finite impulse response

filter. This filter mimics transforming spatial data into the wavenumber domain, and removing the effect of small wavenumber signals, but works faster, as it is a weighted average. This approach was geared more toward C-band radars, and is not included in the phase estimation routines mentioned in this thesis.

An alternative approach is least-squares regression on a moving window along the radar beam. Compared to the other algorithms, this does not directly filter differential phase data, but estimates its slope through the noise in the data.

Finally, there is Kalman filtering, a data assimilation technique which uses assumptions about error covariance to weight the prediction in favor of the observations, or in favor of the theory. This is discussed in chapter 4.2.

Once phase shift has been filtered, providing an estimate of only the propagation effects within the radar beam, we know that changes in the Φ_{dp} are due to rainfall. Therefore, we can relate rainfall rate to the spatial derivative of Φ_{dp} with respect to radar range. This spatial derivative is known as K_{dp}, and is the focus of most of Chapter 4. Empirical raindrop simulation studies used in Testud et al (2000) and displayed in textbooks like Bringi and Chandrasekar (2001) show that K_{dp} is proportional to signal attenuation. At the X-band wavelength in particular, this relationship is linear. One algorithm in this thesis is dedicated to estimating specific attenuation by exploiting this linear relationship. Specific attenuation can be integrated along the range, and added to reflectivity to correct it. Since specific attenuation is proportional to something in Rayleigh scattering theory known as the extinction cross section, researchers like Ryzhkov et al. (2014) suggest calculating rainfall directly from specific attenuation. The extinction cross section is given in equation 4.7.

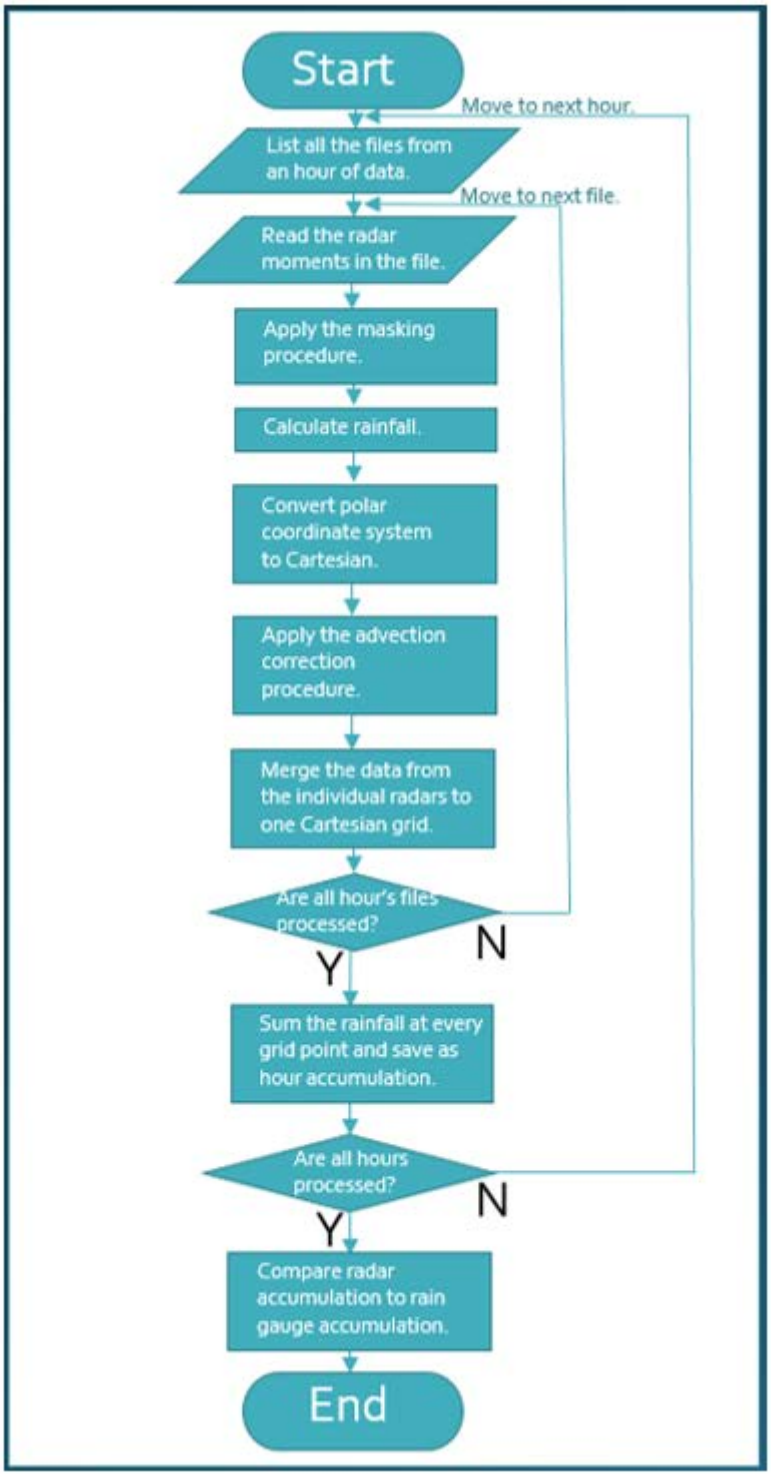

Figure 2.2: Overview of the radar-rainfall algorithm.

The ground reference for the algorithms in this thesis was a network of 20 rain gauges owned by the Iowa Flood Center and the USDA's Agricultural Research Service. These gauges

do not directly measure rain rate, but instead rainfall accumulation over an interval of time. The algorithms for the X-band radar units estimate rainfall rate, so these products should be integrated in time to more closely match the nature of what the rain gauges measure. Integrating rain rates through time poses a problem in that the radar is only able to observe the environment in one snapshot at a time. The radar leaves most of the environment unmeasured at any given time. In order to fill in the temporal latency between rainfall files, an advection correction method is applied. This method identifies the size of the time gap between two files, projects the previous file onto the domain of the new file, and finds a displacement vector that maximizes the statistical correlation between the two files. That vector is scaled by the desired time interval, and the temporal gaps are filled in by the sequentially-advected fields of rainfall. A graphical representation is included in Figure D.1. The result is rainfall estimates with minute resolution in time. The two radar's estimates are mosaicked together in the way shown in Figure E.2. The mosaics are accumulated to the hourly time scale, which is more comparable to the mechanism and time-resolution of rain gauges.

With all the radar moments covered, it is necessary to test their performance. Chapter 3 describes the SMAPVEX-16 field campaign. The radars were calibrated by scanning vertically during rainfall, to dynamically estimate the changing channel discrepancy in received power between the horizontal polarization and the vertical polarization. This calibration using specific varieties of scans was built into the rainfall algorithm.

3. THE SMAPVEX-16 EXPERIMENT

Prior to the launch of Soil Moisture Active Passive [SMAP] in 2015, critical campaigns took place via aircraft, ground sensors, and radio instruments to support the validation and calibration of algorithms to be used aboard SMAP. Experience from existing missions carrying radiometers on board motivated serious research efforts to deal with space-based soil moisture estimation errors. A multi-pronged approach was devised, involving measurements from airborne radar, and field-based investigations of soil roughness and moisture. The following is a discussion of some experiments which led up to the SMAPVEX-16 experiment.

Radio interference problems on the Soil Moisture and Ocean Salinity (SMOS) satellite motivated an investigation into radiometer sensitivity (Park et al. 2008). Data were collected via aircraft over Tennessee in the fall of 2008 and 2009, during SMAPVEX08, to test the brightness temperature sensitivity of a prototype imaging radiometer. Panciera et al. (2014) detailed the SMAPEx experiments of 2010 and 2011, which involved testing the performance of the synthetic aperture radar instrument over Southeastern Australia, offering new sources of soil moisture data collected at L-band, which at the time, few other satellite products offered. Next, SMAPVEX12 produced airborne radar measurement data over an agricultural area south of Winnipeg, Canada. It was also emphasized that improvements should be made in estimating soil moisture in forested locations. McNairn et al. (2015) summarize this experiment, where researchers investigated the soil-moisture conditions across varying vegetation conditions, from June 2012 to July 2012. The choice was made for SMAP to employ L-band wavelengths to mitigate the effects of signal attenuation. However, changing vegetation still alters the apparent roughness of the earth's surface, which has a measurable effect on how SMAP estimates soil moisture. SMAPVEX15 was another test of the radiometer instrument over the Walnut Gulch

experimental watershed, in Arizona, from August 2nd to 18th. (Colliander et al. 2017) A suite of ground-based data was also collected with the help of observation networks run by the USDA's Agricultural Research Service [ARS] in nearby Tucson. This experiment took place shortly after the loss of the radar instrument aboard SMAP, so priorities of the experiment changed accordingly. Some of the goals of SMAPVEX 15 were to investigate the effect of signal diversity on retrieving information from coarser resolution grids. In other words, Researchers wanted information on up-scaling returns to a different resolution with larger cells in the grid.

Finally, with similar objectives in mind as the previous campaigns, SMAPVEX 16 featured similar satellite measurements to SMAPVEX12, but over both Winnipeg, and Central Iowa. The objective of SMAPVEX16 was to dig deeper into regions where the error of SMAP's soil moisture estimates was markedly high. In addition to the radiometer data, soil roughness, precipitation, and vegetation levels were recorded in May, June and August of 2016. There was as desire for multiple forms of soil moisture estimates for validating the SMAP soil moisture estimates. Since precipitation is the biggest driver of soil moisture, the Iowa Flood Center's X-band radar network, with the ability to monitor precipitation on a near-continuous spatial scale, had a place in the SMAPVEX-16 experiment.

In support of the Soil Moisture Active-Passive verification experiment of 2016 (SMAP-VEX 16), the Iowa Flood Center [IFC] deployed two radars which operate at X-band (9.41 GHz) to make precise precipitation measurements on a scale finer than typically used before, in an area surrounding the SMAP-VEX 16 experiment domain, centered in Hardin County, Iowa. Radar operators chose the scanning sectors of both radars such that the South Fork Iowa River watershed received overlapping radar coverage. The South Fork Iowa River watershed was an outstanding site for study because it is small enough to be adequately monitored by a network of

two radars. Also, it is well-instrumented with USGS and Iowa Flood Center Stream gauges, measuring stream discharge with fine temporal resolution.

Fine resolution is vital for places well within the continental United States, especially Iowa, where nocturnal convective thunderstorms are responsible for a large portion of the water budget input (Song et. al. 2005). Huff and Shipp (1969) describe the higher decay in spatial correlation associated with convective style storms, which exist as isolated cells, developing and dissipating quickly compared to longer-lasting stratiform events. This is another reason why high resolution data are desirable for hydrologic studies. Using a network of two radars, estimates of minute rainfall rate, and hour accumulation were generated with fine spatial resolution down to the level of 50 m. While other estimates of rainfall rate existed over the South Fork watershed during this study, this is the only dataset offering resolution finer than the scale of an agricultural field.

Comparison experiments were conducted between the merged radar-precipitation product, and 20 tipping-bucket rain gauges located throughout the experiment domain. The goal was to assess the agreement with ground-based point-measurements. As a complement to the radar and tipping buckets, a vertical profiler and a pair of digital video disdrometers were deployed in the research domain. With this host of instrumentation, the SMAP-VEX 16 experiment offers a dataset tracking precipitation at scales ranging from the size of farm fields to that of individual raindrops. Figure 3.1 illustrates the location of the general domain, within the state of Iowa. Figure 3.2 zooms in closer, revealing the rain gauge network, which was operated concurrently with the radar network.

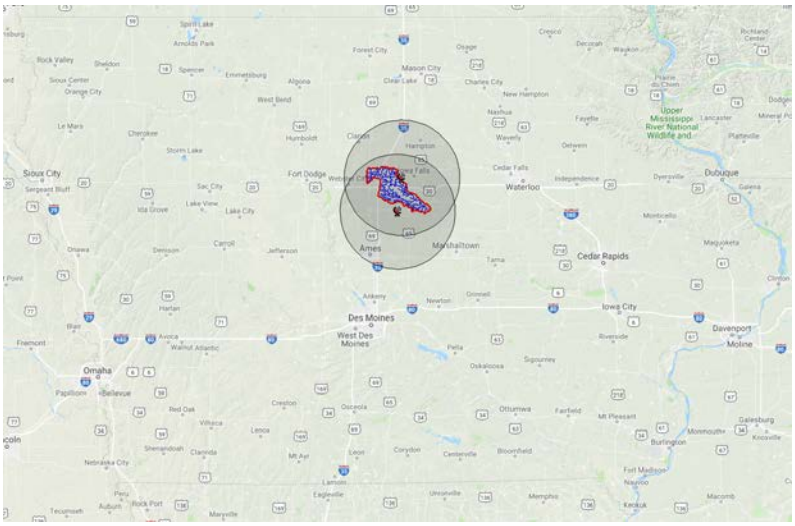

Figure 3.1: The location of the SMAP experiment domain in Central Iowa.

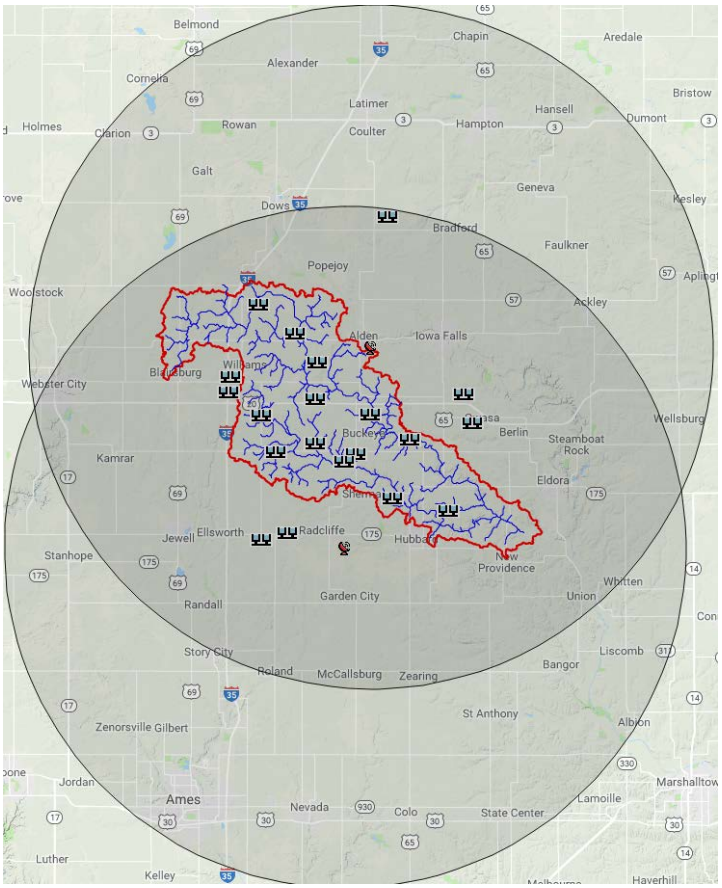

Figure 3.2: A close-up version of Figure 3.1, showing radar and rain gauge locations around the watershed.

Instrumentation

Rain gauge and radar data were collected for two weeks in late spring, May 24-Jun 6 and mid-summer Aug 1 – Aug 14. The two periods of the experiment allow for comparison of conditions during the maize crop's early stages, and its fully grown stage. Technical and electronics issues affected the collection of radar data primarily in the first phase of the experiment. The analysis in this study will examine data from the second phase of the experiment.

Two mobile X-band radar units resided north and south of the watershed, XPOL-2 and XPOL-3 [Xpol North, and Xpol South] where they sampled swaths reaching over and beyond the experimental watershed. Each radar unit was mounted on a trailer and pedestal (Figures 3.6 and 3.7), allowing a 360 degree range of scanning, as well as the ability to scan vertically from zero degrees to 90. With a nominal range of 40 km, they collected data over the watershed with range resolution of 75 m. The 6-foot dish antenna, and 3-cm wavelength contribute to a beam width of 1.4 degrees. However, data was sampled with azimuth resolution of half a degree, so some beam overlapping was present. Both radars possess polarimetric capabilities, with a horizontal and vertical receiving channel built into the antenna. Background processes on each radar server checked MRMS data for rainfall in the area, alerting the operators to warm up and start the radars when rainfall was nearby.

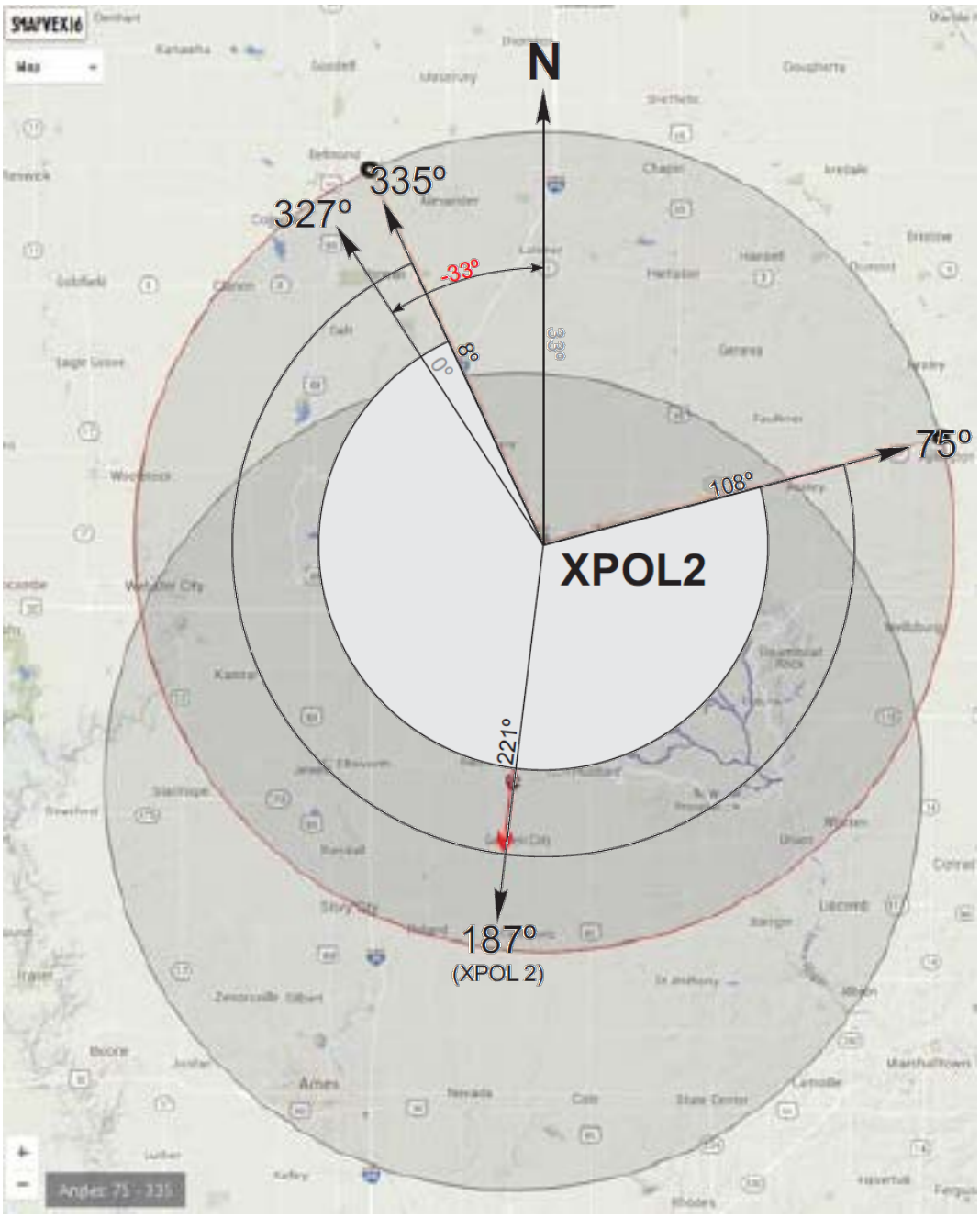

Figure 3.3: Location, and scanning sector of Xpol North.

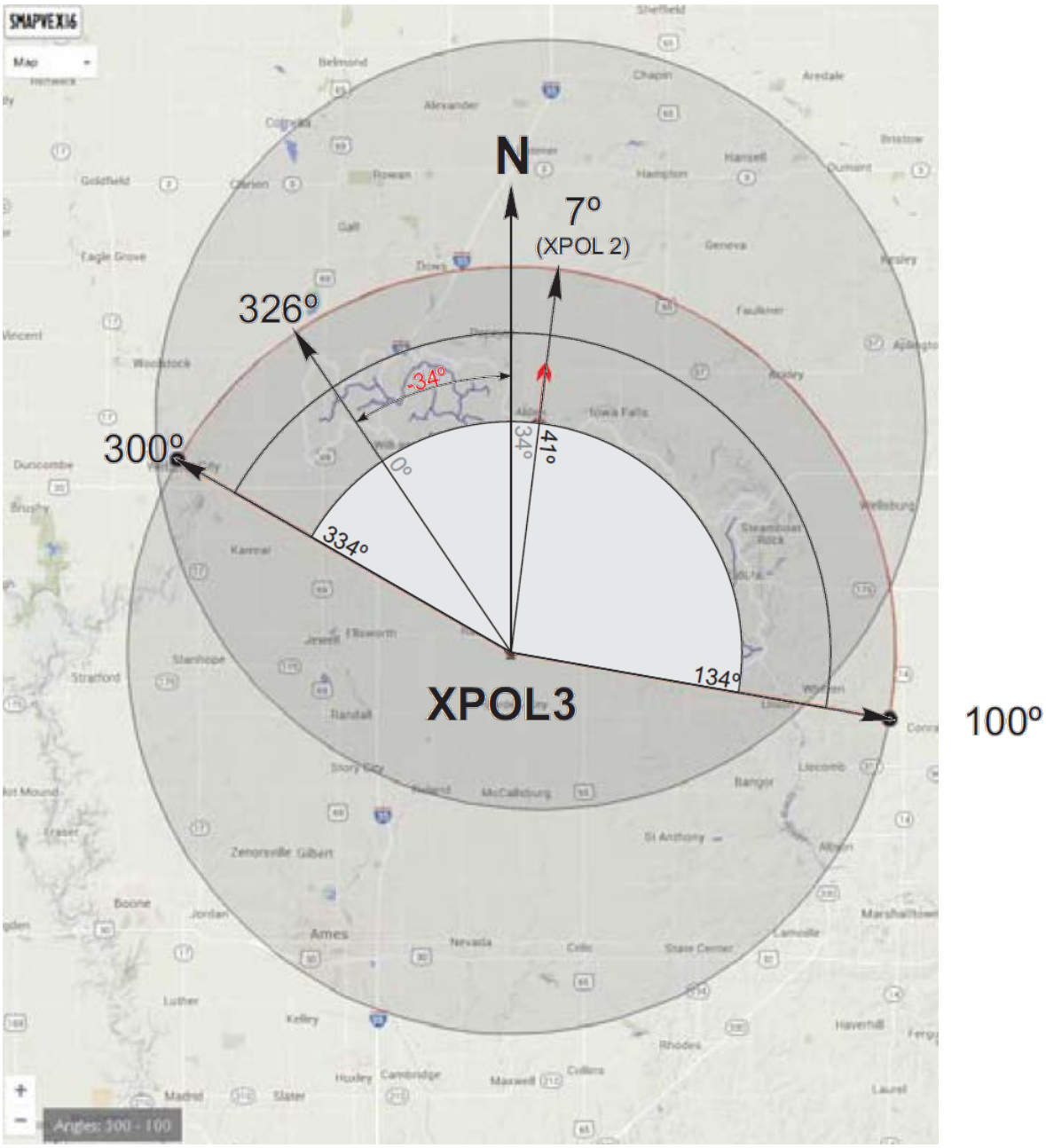

Figure 3.4: Location, and scanning sector of Xpol South.

Stationed in proximity to the radar units two Automated Parsivel Unit (APU) video disdrometers, shown in Figure 3.5, collected precise raindrop size distributions throughout the experimental period. The data collected include raindrop diameter distributions, and velocity distributions.

A vertically-pointed radar, a METEK MRR-2 Micro Rain Radar, operating at K-band, scanned the sky in a vertical profile as storms passed over, providing another source of data comparison for the mobile radar units. This radar had a 70 cm dish diameter, beam width of 2 degrees, operated on a 24 GHz carrier frequency, and recorded data at a range gate resolution of 35m. It had a maximum of 30 range gates, so its farthest observing range was 1050 m. Within this range, the vertical profiler measured reflectivity, terminal drop velocity, and spectrum width. The vertically-pointing radar was located within the South Fork Iowa River watershed, at 42.4704N, 93.3809W, between both X-band radars, to act as a reference while the X-pol units were in RHI mode.

The South Fork Iowa River watershed was densely-monitored with IFC and ARS rain/soil sensors monitoring the rainfall. Both the IFC and ARS stations employed tipping-bucket rain gauges. The setup for the IFC gauge station features two buckets placed in tandem for instrument redundancy. For both types of stations, the measurement resolution provided by one tip was 0.01 in, or 0.254 mm.

Comparing the data from radar and rain gauges brings a few inherent differences to light. Rain gauges collect rainfall reaching the ground, reporting 15-minute accumulation values, indexed by a timestamp corresponding to the end of the 15-minute interval. Radar data is converted to instantaneous rainfall rate, and associated with the time taken to scan the sector, which can be variable. Furthermore, depending on distance from the radar, rainfall estimates can originate from hundreds of meters above the surface. One approach to make these data more comparable is to interpolate the rain gauge data on a 2-D grid, with identical resolution as the radar product.

Ignoring the difference in resolution volume constitutes the second approach. Mandapaka et al (2009) used a simulation study to demonstrate that the correlation structure of rainfall measurement error fields remains very similar from near point to spatial scales of a few kilometers. Since the resolution of the Xpol product is well within this limit, we have reasonable confidence in expecting similar error correlation structure among the rain gauges and the radar units.

Data Types

Products from the Xpol units immediately available after collection included horizontal and vertical reflectivity, differential reflectivity, raw differential polarization backscatter phase angle, cross-polarization correlation coefficient, horizontal and vertical raw power, and signal to noise ratio. Doppler shift velocity was available for some of the radar data collected, but not all. There are vertical profiles of reflectivity, cross-polar correlation, and Zdr available, but on an interval of about once every 30 minutes.

The METEK MRR-2 Vertical profiler collected terminal velocity data during rainfall events, as well as reflectivity and spectral width. By sampling a 4 profiles within 10 seconds, this instrument shed light on the drop size distribution through time.

Figure 3.5: Left, the METEK MRR-2 Vertical K-band radar profiler stationed at Vierkandt Farms. Right, the Automated Parsivel Unit APU03 disdrometer deployed near XPOL-2. Photo credit: Daniel Ceynar.

Figure 3.6: Xpol-2 unit deployed south of Alden, Iowa in May 2016. Photo credit: Daniel Ceynar.

Figure 3.7: Xpol-3 Mobile radar unit deployed at Hindman Farms near Radcliffe, Iowa in May 2016. Photo credit: Daniel Ceynar.

While in Plan-Position-Indicator mode [PPI] the mobile radars scanned at 3 degrees, and 4 degrees elevation across the experimental domain. Range-height- indicator [RHI] scans were also intermittently executed in the direction of the sister radar, between 0 and 20 degree elevations. Finally, vertical profiles of reflectivity [VPR], and differential reflectivity were observed along with the RHI scans. VPR scans allowed for tracking of the polarization channel agreement during the data-analysis phase, and were a form of quality control. The value of Z_{dr} channel correction was calculated by minimizing the absolute value of the median conditional Z_{dr} at different reflectivity thresholds. This calculated value was then catalogued as a function of time, and used to estimate an appropriate calibration constant. Every time a vertical profile was observed with enough rainfall present to get a reliable estimate, the calibration offset value was updated.

Quality Control Techniques

Any physical radar system encounters difficulty emitting only a narrow focused beam away from the influence of topography or buildings. Since the refractive index of air is temperature-sensitive, certain weather phenomena lead to situations where the propagation path of the radar pulses intercept the ground. Moreover, side lobes (regions of higher intensity directed microwaves outside the volume of the main beam) often intercept the ground. Given the two-radar configuration of the SMAP-VEX experiment, one radar is always observing the volume of sky above the other. These special locations within the polar coordinate domain can be represented by a subset of the Cartesian domain generated in the advection-correction stage, and the ground-clutter susceptible area can simply be swapped for the signal observed by the other radar at that location. Since disdrometers were deployed nearby each radar, we have a data source to quantify the accuracy of this approach.

The Xpol radars sometimes required close supervision, especially during the hot and humid days of the experiment. Heating of the internal hardware would put the instruments out of calibration, or shut them down entirely.

Therefore, comparisons in this study were done only with periods of record where both the rain gauges, and the radar units were operating for the entire hour. Data were only removed from analysis when one of the radar was down at the time of observation.

4. METHODS OF DATA PROCESSING

The advantage of dual polarization stems from the fact that raindrops have been observed to grow wider as they become more massive. This leads to geometric anisotropy in their collective backscattering cross sections. This effect was systematically quantified by Pruppacher and Beard in 1970. However, more information is required to estimate rainfall rate. If one draws a control volume containing a rain-producing storm, but excluding the ground, the rainfall rate can be empirically derived.

For a simple example, assume a collection of N uniformly sized drops of diameter D are falling with velocity V from a control volume of height h over some area of size A. Because of how rainfall is typically measured in units of depth, we are looking to calculate the time rate of change of water volume falling out of the control volume divided by the area A.

$$R = \frac{V}{h} * N\pi \frac{D^3}{6} * \frac{1}{A} \tag{4.1}$$

We basically have the volume of water removed from a unit control volume of air per unit time. If we want to be more true to the real world, we need to consider diversity in raindrop size, and non-uniform falling speeds. This motivated researchers to seek out convenient functions which relate diameter to terminal velocity, and the probability of observing a raindrop of a given size. Equation 4.1 can be reformed to the following form.

$$R = \frac{\pi}{6hA} \sum_{i=1}^{N} V_i D_i^3 = \frac{\pi}{6} \int_0^\infty V(D) N(D) dD, \tag{4.2}$$

where N(D) is the number density per unit volume of drops of a size D. Equation 4.2 assumes the existence of some smooth relationship between terminal velocity and drop diameter, which show general success (Atlas and Ulbrich 1977). However, Lee et al. (2004) elaborate that the assumptions made about drop size and velocities introduces uncertainty, and the business of simplifying drop distributions comes with consequences. One popular assumption is that raindrop diameter is exponentially distributed, as it provides a manageable expression for the integral in 4.2 if *V(D)* is a power-law model. It is on this basic assumption that earlier researchers derived reflectivity-rainfall relations.

Recall the Rayleigh scattering equation in A.11. Rayleigh scattering explains that the backscattering cross section is proportional to the 6th moment of drop diameter inside the resolution volume. We then have the following.

$$\sum_i \sigma_i = \frac{\pi^5 |k|^2}{\lambda^4} \sum_i D_i^6 = \frac{\pi^5 |k|^2}{\lambda^4} \int_0^\infty D^6 N(D) dD, \tag{4.3}$$

One can use the properties of the 3-parameter gamma pdf (Ulbrich 1983) to surmise the following expression only if *N(D)* is exponentially or gamma distributed.

$$N(D, \alpha, \beta) = N_0 D^\alpha e^{-\beta D}, \tag{4.4}$$

where α,β are greater than or equal to 0, then equation 4.5, which uses the help of the gamma function, provides a value for the integral.

$$\Gamma(\alpha+1)\beta^{-\alpha} = \int_0^\infty D^\alpha e^{-\beta D}\, dD, \tag{4.5}$$

where the gamma function can be evaluated iteratively to the desired error tolerance. However, if the parameter α is chosen to be an integer, the expression in 4.5 reduces to $\alpha!\beta^{-\alpha-1}$. This may add some level of convenience, but α is rarely an integer in practice. The gamma function can be calculated by the following series.

$$\Gamma(x) = e^{-\gamma x}\frac{1}{x}\lim_{n\to\infty}\prod_{k=1}^{n}\frac{e^{\frac{x}{k}}}{1+\frac{x}{k}}, \tag{4.6}$$

where γ is the Euler-Mascherioni constant = 0.5772156649...

This method of obtaining an exact calculation for the integral term in rainfall rate, or backscatter cross section is what leads researchers to assume exponential or gamma distributions for raindrop diameter, as well as power-laws, or polynomial models for terminal velocities. The take-home message of equation 4.5 is that the solution to the integral in equation 4.2 and 4.3 takes the form of a power law. This was of particular interest to Marshall and Palmer (1948) leveraged this idea of using power laws to back out an early version of the Z-R relationship. Since the backscattering cross section reduces to a power law under some assumptions, and the rainfall rate reduces to a power law under the same assumptions, there was good reason to believe that the backscattered power was related to rainfall by power law.

Although the Z-R relationship was an early method of estimating rainfall via radar products, two very serious problems cause the dispersion of Z-R-derived vs actual rainfall rate residual to skyrocket. The first problem is glaringly visible in the Rayleigh scattering law. The backscatter is proportional to the sixth power of drop diameter. This means that the incremental

change in backscatter cross section is proportional to six times the drop diameter to the fifth power. In short, inverting reflectivity to drop diameter, to estimate the drop distribution parameters causes uncertainty to propagate quickly with every small input error. This is not to say that the drop size distribution, say estimated by a disdrometer, is a bad estimator of reflectivity, but rather reflectivity may be badly estimated by radar due to small errors in the estimated backscatter cross section due to beam filling, beam blockage, or other artifacts. Second, if the signal is attenuated, an amplitude-based product like reflectivity will have a large error due to underestimation.

Researchers have also investigated the extinction cross section, which is proportional to the third moment of the drop size distribution, as given on page 40 of Doviak and Zrnic (2006).

$$\sigma_{ext} = -\frac{\pi D^3}{\lambda} \mathrm{Im}(-k) \tag{4.7}$$

Scattering simulations, and empirical studies have linked the extinction cross section to specific differential phase shift.

Rhyzhkov et al (2014) suggested specific attenuation as a superior estimator of rainfall rate compared to reflectivity because it is nearly linearly related to the extinction cross section, and is related to K_{dp} as well. (Testud et al., 2000, Bringi and Chandrasekar 2001, Anagnostou et al., 2004)

Reflectivity-Rainfall

The result of calculating Specific attenuation along the radar beam and integrating with respect to range, was used to correct the base horizontal reflectivity. The attenuation-corrected reflectivity was then placed into the standard Z-R relationship to estimate instantaneous rainfall rate. Researchers have known that a radar signal de-amplifies at an exponential rate, as it

propagates through even a slightly conducting medium. Hitschfeld and Bordan (1954) elucidated the expected behavior of an attenuating radar signal. However, the solution proposed is not always numerically stable. The standard in the U.S. is the following equation $Z = 300 * R^{1.4}$, which when solved for rainfall, and adjusted for Z in decibel units estimates rainfall rate is given by:

$$R = 0.00333 * \left(10^{\frac{Z}{10}} \right)^{0.714} \tag{4.8}$$

K_{DP}-Rainfall

Many researchers prefer phase-based measurements, which are less adversely affected by signal attenuation (Matrosov et al. 2002, Park et al. 2005, Ryzhkov et al. 2014, Diederich et al. 2015).

If the horizontal axis of a large raindrop is always greater in size than the vertical drop axis, then the horizontally polarized component of an incoming radar pulse should lag in phase more than that of the vertical component. This effect should cause Φ_{dp} to increase monotonically, and K_{dp} to be positive at all times. However, phase shifting due to backscattering may be significant at X-band during heavy rainfall. (Hubbert and Bringi, 1995, Zrnic and Ryzhkov, 1996, Keenan et al. 2001) Moreover, the presence of vertically-oriented hailstones can exist in rain cores as well. Both of these situations cause Φ_{dp} to decrease, and K_{dp} to sometimes drop below zero, contrary to how theory predicts.

The larger the marginal gain in phase difference between polarization channels, the more intense the rainfall must be. This profile of differential phase shift is the reference profile for constraining the attenuation correction scheme. Methods for estimating this particular dual-

polarization product, K_{dp} must overcome limitations due to signal noise. This thesis focuses on two methods of calculating K_{dp}.

Finite differencing is a popular and simple estimate of slope, but does not necessarily perform well on a noisy data set. This approach is not used here, as the X-band radars do not provide smooth enough curves of Φ_{dp}.

$$K_{dp} = \frac{\Phi(r_1) - \Phi(r_0)}{2(r_1 - r_0)}, \tag{4.9}$$

where r_1 and r_0 are distance from the radar, and Φ is the differential propagation phase shift, recorded by the radar.

Moving-Window Least-Squares Regression

Regression slope calculation selects a buffer of points along the Φ_{dp} profile, and fits a line to the points, with a slope which minimizes the residual between the line and the points. This is more costly computationally, but provides a robust estimate of slope, minimizing the squared discrepancy between the individual data points, and a linear model, which attempts to explain some of the observed variation between radar range and Φ_{dp}.

$$K_{dp} = \frac{\mathrm{cov}(\Phi_{dp}, r)}{2\,\mathrm{var}(r)} \tag{4.10}$$

When selecting the buffer length of r or Φ_{dp}, Ryzhkov et al. (2014) and Mishra et al. (2016) used selection systems based on the observed reflectivity. The intense rainfall tends overpower the noise in the signal, and fewer points are needed in estimating the regression slope.

Lower rainfall intensity allows for more noise relative to the Φ_{dp} signal slope, and more points are required for a good estimate. The specifics for determining the range of sizes of optimal buffer lengths in this method are ad-hoc however.

Kalman Filtering Approach

In the business of smoothing a signal, and predicting signal characteristics through high levels of noise, Kalman (1960) suggested a useful data assimilation method, capable of linear filtering. Since our understanding of K_{dp} comes directly from Maxwell's equations, and sophisticated scattering simulations, we have a solid understanding of the prediction error and sensitivity of scattering processes. When our measurements are in question due to noise or contamination, more weight can be put into theory predictions when estimating the state of a linear system. An important distinction for the notation of the upcoming section is that δr stands for the range gate spacing, while δ_{hv} represents backscatter differential phase shift.

For the case of K_{dp}, we use the general Kalman filter form to define the states of the system in equations 4.11 and 4.12.

$$Z(r) = F_r S(r) + \varepsilon_Z \tag{4.11}$$

$$S(r+\delta r) = T_r S(r) + \varepsilon_S \tag{4.12}$$

where **Z** is a matrix representing the measured state of the system at range r, **F** is the observation model matrix, which defines the linear relationship between the state variables. The error term ε_z stems from the errors in observations.

$$Z(r) = \begin{bmatrix} \Psi_{dp}(r) \\ \Psi_{dp}(r+\delta r) \\ c \end{bmatrix} \tag{4.13}$$

In equation 4.13, c is a constant, which does change based on rainfall intensity. This is because backscatter differential phase shift, δ_{hv} is related to K_{dp} in a non-linear way. The constant c changes such that a piecewise linear function describes the relationship between K_{dp} and δ_{hv}. Schneebeli et al (2014) provided Figure 4.1 to describe this approach. Since the Kalman filter is only applicable to linear models, this decreases accuracy, but is a necessary assumption.

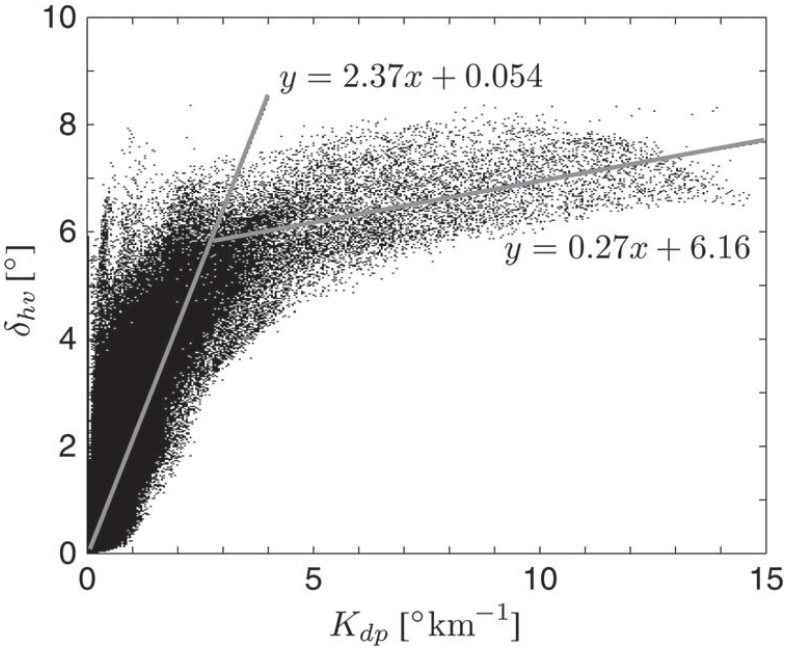

Figure 4.1: Backscatter differential phase shift vs. K_{dp}, published by Schneebeli et al (2014).

The matrix **S** represents the state of the system, whether measured, or predicted by theory, or a mixture of both. **S** in equation 4.11 represents the state of the system. **S** in equation 4.12 represents the estimated state at the next range gate involving the measurements and the theoretical model.

$$S(r) = \begin{bmatrix} K_{dp}(r) \\ \delta_{hv}(r) \\ \Phi_{dp}(r) \\ \Phi_{dp}(r+\delta r) \end{bmatrix} \tag{4.14}$$

The linear relationships between the variable of interest are woven together in the matrix **F**.

$$F = \begin{bmatrix} -2\delta r & 1 & 0 & 1 \\ 2\delta r & 1 & 1 & 0 \\ -b & 1 & 0 & 0 \end{bmatrix} \tag{4.15}$$

For the matrices **Z** and **F**, c = 2.37, and b = 0.054 when Kdp < 2.5^{o}km^{-1}. Next, c = 0.27, and b = 6.16 when Kdp > 2.5^{o}km^{-1}. These parameters are specific to X-band, and values for S- and C-band are available in Schneebeli et al. (2014).

The transition matrix **T** is responsible for going from the current state to the forward-propagated state. In this instance, we are referring to this transition matrix only in the context of the Kalman filter, not in scattering theory, where a similar-sounding transmission matrix is discussed. The error term ε_s contains the error of the forward-propagated state estimates.

$$T = \begin{bmatrix} 1 & 0 & 0 & 0 \\ 0 & 1 & 0 & 0 \\ 0 & 0 & 0 & 1 \\ 2\delta r & 0 & 0 & 1 \end{bmatrix} \tag{4.16}$$

An assumption used here is that K_{dp} at one range gate equals K_{dp} at the following gate. This is not strictly correct at all, but K_{dp} changes relatively slowly from range gate to range gate, so this approach is not perfect, but still useful.

The utility of Kalman filtering is to infer the next state by weighting measurements vs. theory predictions. The following equation utilizes the matrix **K** known as the Kalman gain. Subscripts of "*r*" are used to indicate that the matrix changes for each range gate, and the calculation is repeated.

$$S^{(+)}(r) = S^{(-)}(r) + K_r\left[Z(r) - FS^{(-)}(r)\right] \tag{4.17}$$

In equation 4.3.10, the superscript (+) represents a state already processed through the filter process. The superscript (-) represents a state being fed into the filter in order to calculate something with script (+). Each of these states are associated with a covariance matrix **P**. In order to calculate $\mathbf{P}^{(+)}$, one must calculate the Kalman gain and $\mathbf{P}^{(-)}$. The matrix **P** depends on $\mathbf{C}(\varepsilon_s)$, and the Kalman gain depends on both $\mathbf{C}(\varepsilon_s)$ and $\mathbf{C}(\varepsilon_z)$. Schneebeli et al. (2014) calculated $\mathbf{C}(\varepsilon_s)$ and $\mathbf{C}(\varepsilon_z)$ for x band radars, and most of the variability in these matrices at X band comes from the radar's range resolution. These calculations are based on T-matrix scattering simulations. The Xpol's 75-m range resolution is substituted for δr, and the exact numerical matrix used in the calculation is provided.

$$C(\varepsilon_s) = \begin{bmatrix} (.11+1.56\delta r)^2 & (.11+1.85\delta r)^2 & 0 & (.01+1.10\delta r)^2 \\ (.11+1.85\delta r)^2 & (.18+3.03\delta r)^2 & 0 & (.01+1.23\delta r)^2 \\ 0 & 0 & 0 & 0 \\ (.01+1.10\delta r)^2 & (.01+1.23\delta r)^2 & 0 & (-.04+1.27\delta r)^2 \end{bmatrix} = \begin{bmatrix} 0.051529 & 0.06187656 & 0 & 0.00855625 \\ 0.06187656 & 0.16187656 & 0 & 0.01045506 \\ 0 & 0 & 0 & 0 \\ 0.00855625 & 0.01045506 & 0 & 0.09287256 \end{bmatrix}_{XPOLS} \tag{4.18}$$

$$C(\varepsilon_z) = \begin{bmatrix} \sigma^2_{\Psi_{dp}} & 0 & 0 \\ 0 & \sigma^2_{\Psi_{dp}} & 0 \\ 0 & 0 & 1.57 \end{bmatrix} = \begin{bmatrix} 4 & 0 & 0 \\ 0 & 4 & 0 \\ 0 & 0 & 1.57 \end{bmatrix}_{XPOLS} \tag{4.19}$$

With $\mathbf{C}(\varepsilon_S)$ and $\mathbf{C}(\varepsilon_Z)$ defined, one can calculate the covariance matrices, and the Kalman gain.

$$P_{S_r}^{(+)} = (I - K_r F) P_{S_r}^{(-)} \tag{4.20}$$

$$P_{S_r}^{(+)} = T P_{S_{r-1}}^{(+)} T^T + C(\varepsilon_S) \tag{4.21}$$

$$K_r = P_{S_r}^{(-)} F^T \left[F P_{S_r}^{(-)} F^T + C(\varepsilon_Z) \right]^{-1} \tag{4.22}$$

Finally, we can calculate the forward-propagated state according to the classical Kalman filtering technique, in equation 4.17. An example of this is shown in Figure 4.2, where filtered differential phase is overlaid with its raw profile. It is important to note that this technique has a spin-up and spin-down time, which was accounted for by a spatial offset in the processing algorithm. The size of the spin-up offset for the Xpol radars was 13 range gates.

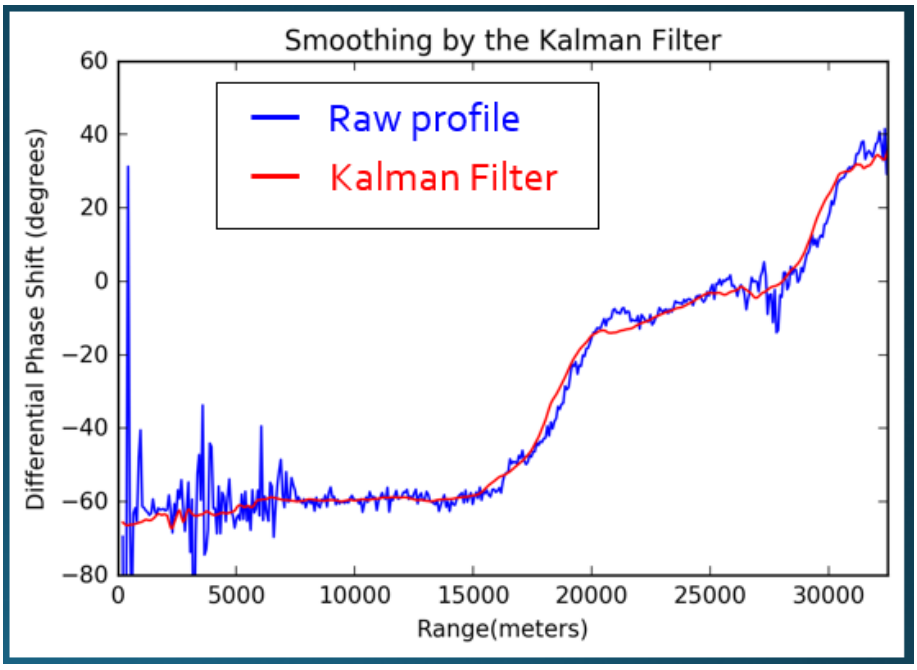

Figure 4.2: Example of the Kalman filter approximating the propagation phase shift from a raw Ψdp profile.

Ryzhkov et al (2014) suggested power law transformations for K_{dp}. The relationship in equation 4.23 is used in the data processing steps of the Xpol radars.

$$R = 16.9 * K_{DP}^{0.80} \tag{4.23}$$

Specific Attenuation-Rainfall

Once K_{dp} is calculated, one can use the linear relation between K_{dp} and specific attenuation, used in Ryzhkov et al. The problem is, that the constant of proportionality between specific attenuation and K_{dp} takes a range of values depending on the rainfall pattern observed (Bringi and Chandrasekar 2001.) From the radar data, the profiles of Φ, and Z are considered known for the length of the beam.

The following equations, described in Bringi and Chandrasekar, calculate an optimal proportionality constant between specific attenuation and K_{dp} given Φ_{dp} and Z. This is done by calculating a synthetic version of Φ_{dp} from an assumed power law relationship between reflectivity and specific attenuation. The routine uses many values of alpha, estimating a profile of $\Phi_{dp,}$ comparing it to the real Φ_{dp}, and calculating the summed discrepancy along every range gate. This summed discrepancy, Δ, is shown in equation 4.28, and the proportionality constant which produces the smallest Δ is chosen.

In other words, select the value of α which corresponds to the minimal summed residual between the estimated Φ_{dp} profile and the one observed by the radar. At X-band, α is usually bounded between 0.2 and 0.4 (Bringi and Chandrasekar 2001.)

The optimization process (the four equations above for a specified range of values for α) is meant to be repeated for each azimuth angle in the radar scan. This serves as another method to assimilate the radar data, exploiting the self-consistency of radar moments. In order to take advantage of this added insight, researchers generally choose one of the following options when estimating rainfall with a system affected by attenuation. Option one is to integrate specific attenuation over the range, and correct the attenuated reflectivity, estimating rainfall from the corrected reflectivity. Option 2 is to estimate rainfall rate directly from specific attenuation. Both options have strengths and shortcomings, especially because assumptions were made in these derived products.

$$K_{dp}(r) = \frac{A(r)}{\alpha} \tag{4.24}$$

$$\Phi_{dp}(r) = 2\int_{0}^{r} K_{dp}\, dr \tag{4.25}$$

$$I(r_0, r) = 0.46b\int_{r_0}^{r} [Z'(r)]^b\, dr \tag{4.26}$$

$$A(r) = \frac{[Z'(r)]^b (1 - \exp[-0.23b\alpha[\Phi_{dp}(r_m) - \Phi_{dp}(r_0)]])}{\left(I(r_0, r_m) - I(r_0, r)(1 - \exp[-0.23b\alpha[\Phi_{dp}(r_m) - \Phi_{dp}(r_0)]])\right)} \tag{4.27}$$

$$\Delta = \sum_{i=1}^{N} |\, \Phi_{dp}(r_i) - \Phi_{dp(const)}(r_i, \alpha, b)\,|, \tag{4.28}$$

Ryzhkov et al (2014) suggested power law transformations for specific attenuation *A*, and is used in the processing routine of the Xpol radars.

$$R = 43.0 * A^{0.76} \tag{4.29}$$

Multi-Parameter Rainfall

Different dual pol moments have different strong suits when estimating rainfall. At X-band frequencies, reflectivity and differential reflectivity can provide reliable estimates of rainfall if the raindrops are below 3 mm (Matrosov et al. 2002). However something more is needed for very intense rainfall, which is common in Iowa during the summer convective season (Song et al. 2004; Market et al. 2001). Vivekanandan et al. (1999) highlighted the ability of K_{dp} to overcome limitations posed by partial beam occlusion, and signal returns from ground clutter. K_{dp}'s resistance to signal attenuation means that it can provide reliable estimates in very heavy rain. Matrosov et al. (2002) suggested a multi-parameter algorithm to intrinsically handle the variability in drop shape, and rainfall intensity, which uses reflectivity and differential reflectivity for the light rain estimates, and K_{dp} to account for intense convective cores. Anagnostou et al. (2004) improved this algorithm, and suggested the following form which is tuned specifically for rainfall in Iowa.

$$R = 63.7 Z^{-0.16} Z_{dr}^{-0.07} K_{dp}^{1.12} \tag{4.30}$$

5. RESULTS OF THE SMAP CAMPAIGN

Phase 1 of the SMAPVEX-16 campaign lasted for two weeks from May 24, 2016 to June 6, 2016, where the crop vegetation was expected to have a minimal influence on the SMAP Satellite's estimates of soil moisture. Phase 2 was also a two-week operation lasting from August 1, 2016 to August 14, 2016. During this time, the crop vegetation was at full height. These distinctions were more important for the SMAP satellite's estimation of soil moisture, rather than the Xpol units' estimation of rainfall.

Phase 1 of the campaign provided ample opportunities for rainfall observations. However, the data quality was poor. Issues arose with the radar processing, particularly keeping a constant frequency as the temperature of the magnetron changed. Z_{dr} and Z_h did not follow an expected relationship. There were unusually low observations of reflectivity during thunderstorms, and the correlation coefficient rose above 1, which is not theoretically reasonable. Both Xpol North and Xpol South had this effect during phase 1, and the data is not high enough quality for analysis.

Phase 2 showed more reasonable data, without the issues encountered in phase 1. Phase 2 involved three large rainfall events in the two week experiment, and most of the analysis springs from these events on August 4th, August 11th, and August 12th. Figure 5.1 shows when both radars were operating, as well as MRMS-estimated mean areal rainfall over the basin. August 4th and 11th showed mostly convective thunderstorm events, while August 12th provided a mostly stratiform event, lasting almost the entire day.

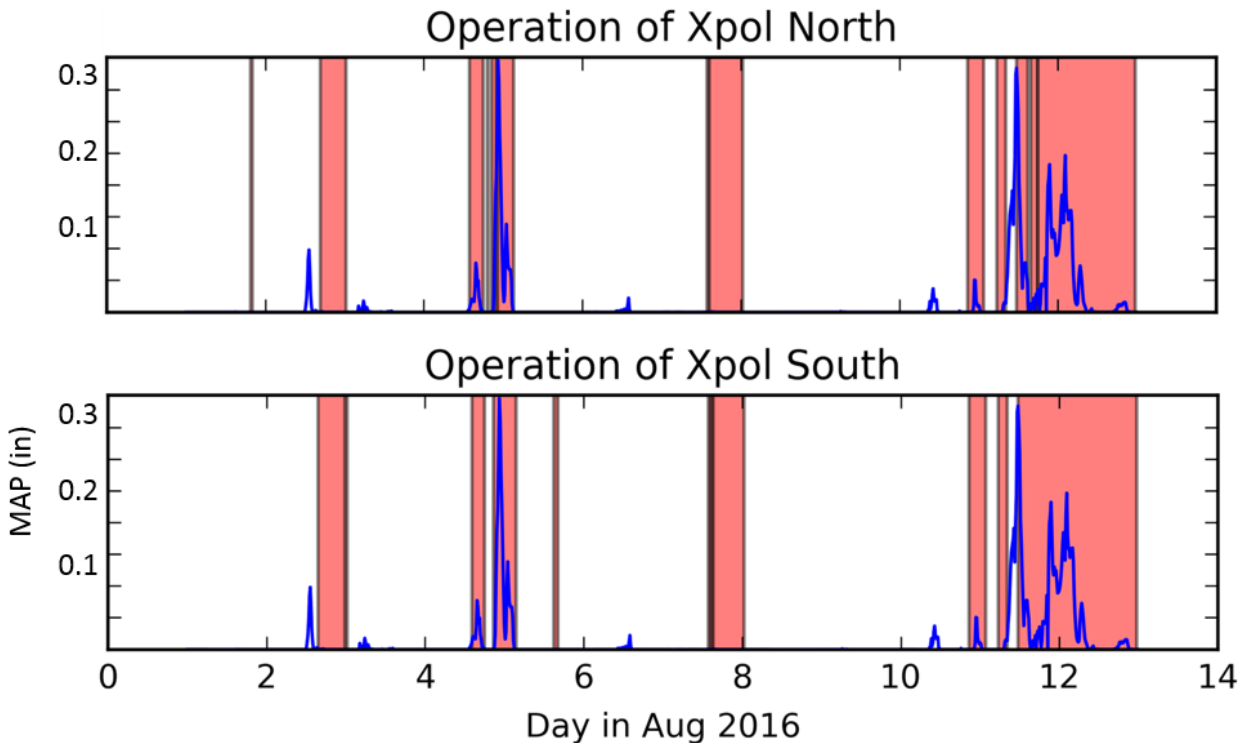

Figure 5.1: Charts indicating the operation time of the Xpol radars during phase 2 of the SMAPVEX-16 experiment, blue indicating MRMS-indicated mean-areal precipitation, and red indicating that the Xpols were operating.

Rain Gauge Accumulations

Five permanent Iowa Flood Center rain gauges reside within the experimental domain, in and around the South Fork Iowa River basin. During the campaign, 15 gauges from the Agricultural Research Service (ARS) were also stationed around the experimental watershed. These 20 gauges served as a reference source of ground data, when trying to test radar processing algorithms, all the way to rainfall accumulation.

During phase 2 of the SMAP campaign, the 20 rain gauges across the domain collected between 50 and 180 mm (2 and 7 in) of rainfall. Kriging interpolation on the available rain gauges was used to provide a sanity check on the accumulated radar estimates, based on the point-measurements of 2-week rainfall accumulation. Figure 5.2 indicates the spatial estimates of

rainfall as well as the estimated error standard deviation of the interpolation method. It can also be seen that the radar based accumulation agrees remarkably with the interpolated gauge-data.

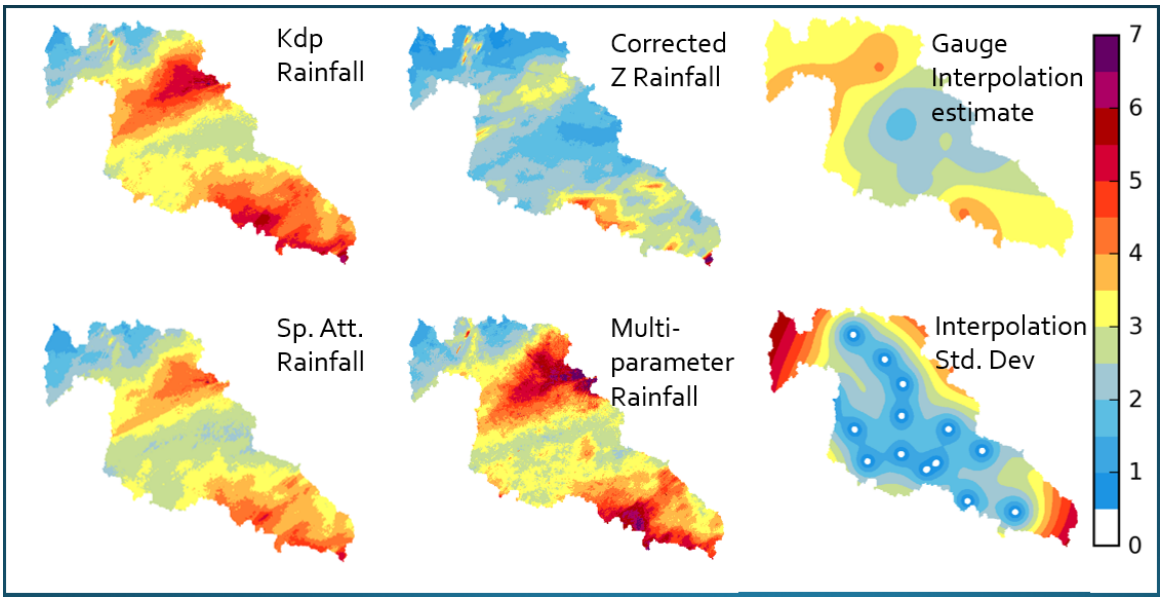

Figure 5.2: Gauge-interpolated, with estimated standard deviation, and radar-estimated rainfall estimates across the experimental watershed (inches).

Parsivel Digital Video Disdrometers [Automated Parsivel Unit or APU] were also deployed next to each radar unit. These instruments recorded continuously throughout phase 1 and phase 2. Figure 5.3 displays the 1-hr accumulation results from the disdrometers. Figure 5.4 compares the running total of these accumulations to those from the Xpol radars.

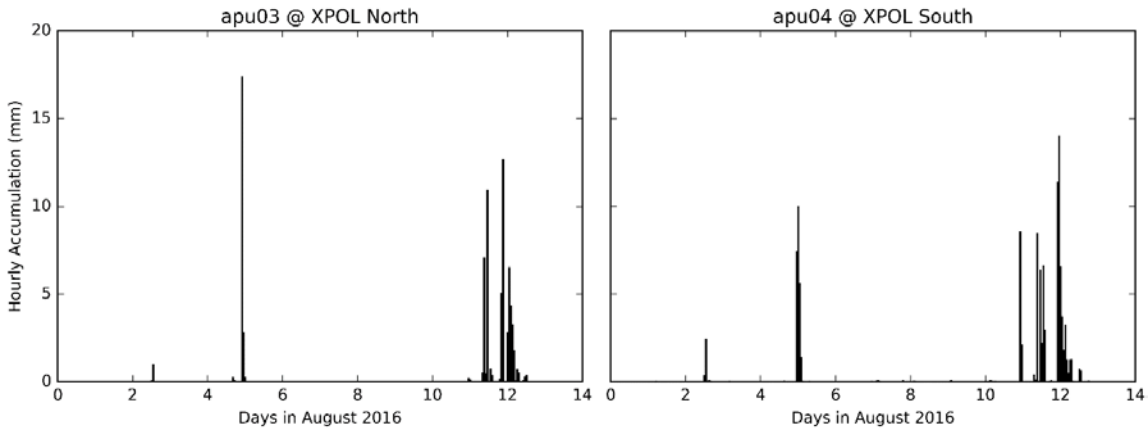

Figure 5.3: Hourly rainfall accumulations observed by the two APU disdrometers during phase 2 of the experiment.

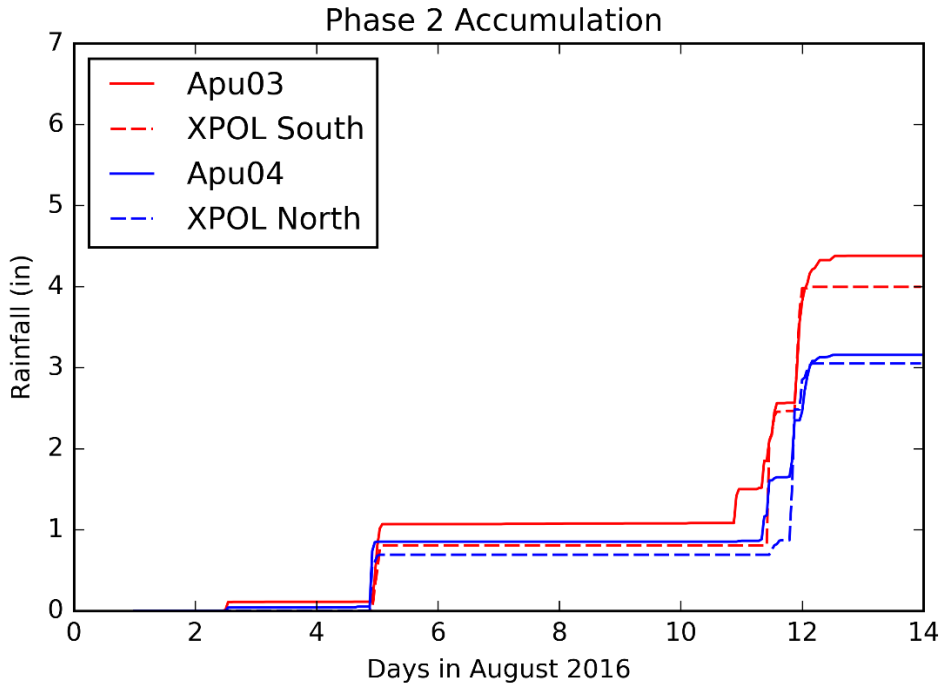

Figure 5.4: Time series comparison of accumulation between X-band radars and disdrometers.

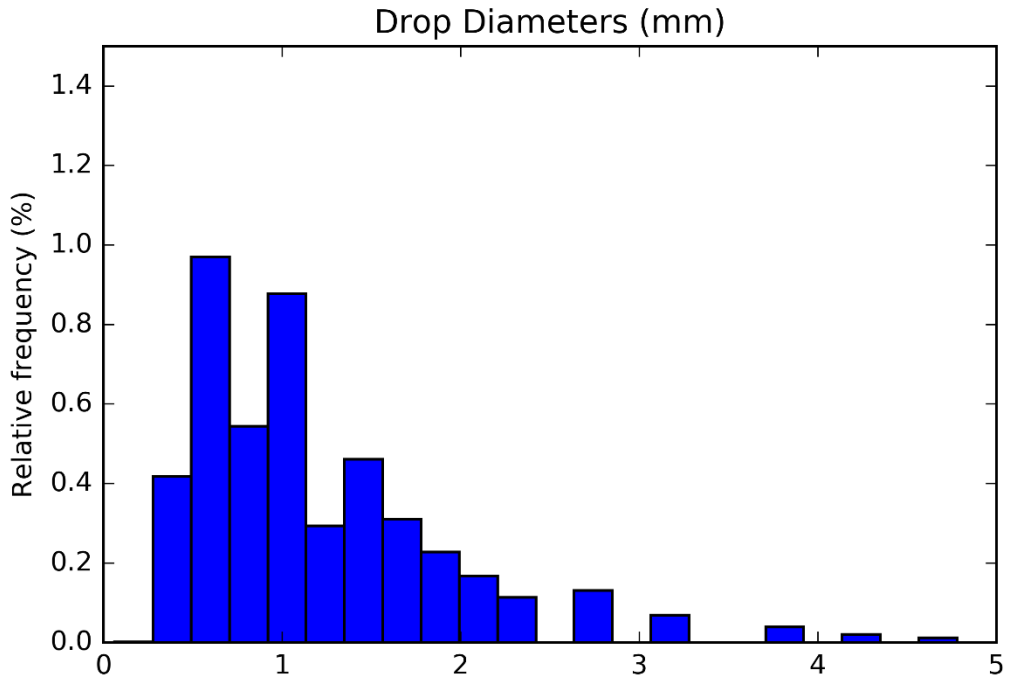

Figure 5.5: Drop size distribution observed on the night of August 4, 2016 at Xpol South's location.

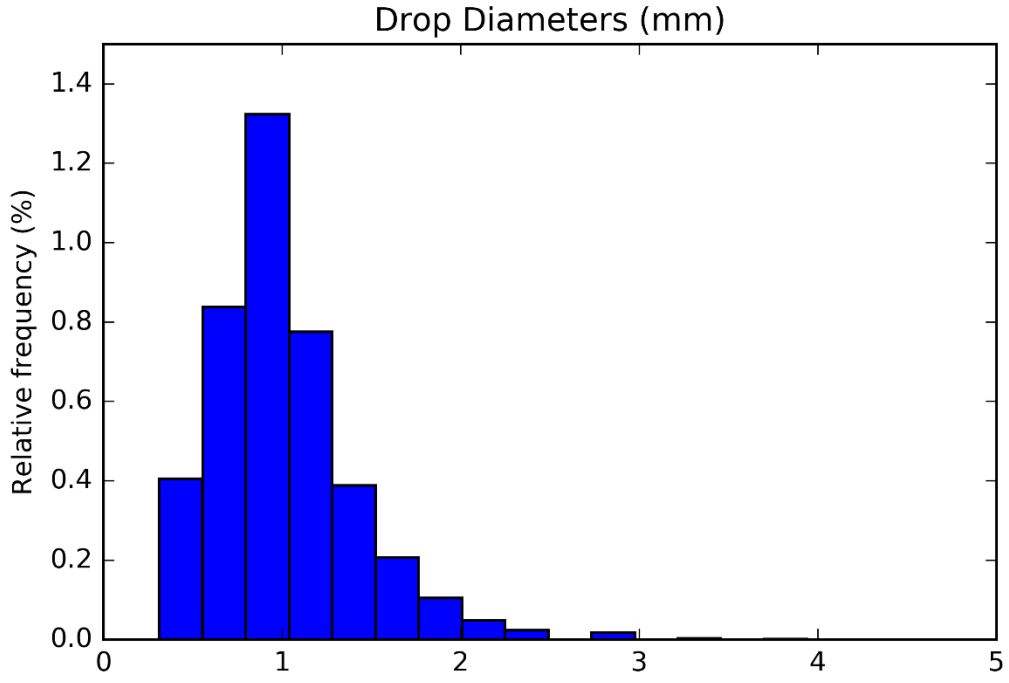

Figure 5.6: Drop size distribution observed on the night of August 11, 2016 at Xpol South's location.

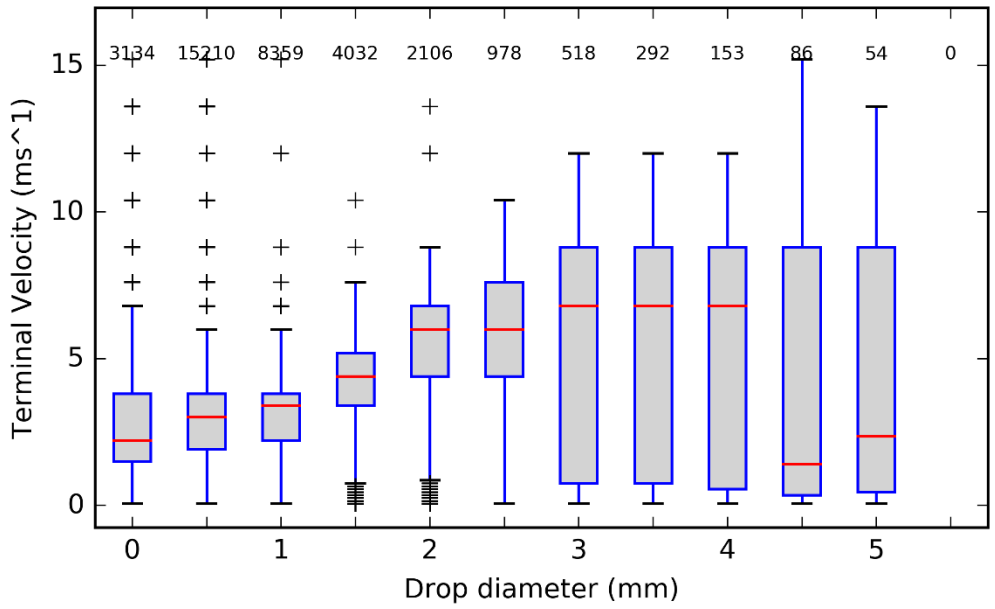

Figure 5.7: Drop velocity distribution conditioned on drop size, observed on the night of August 4, 2016.

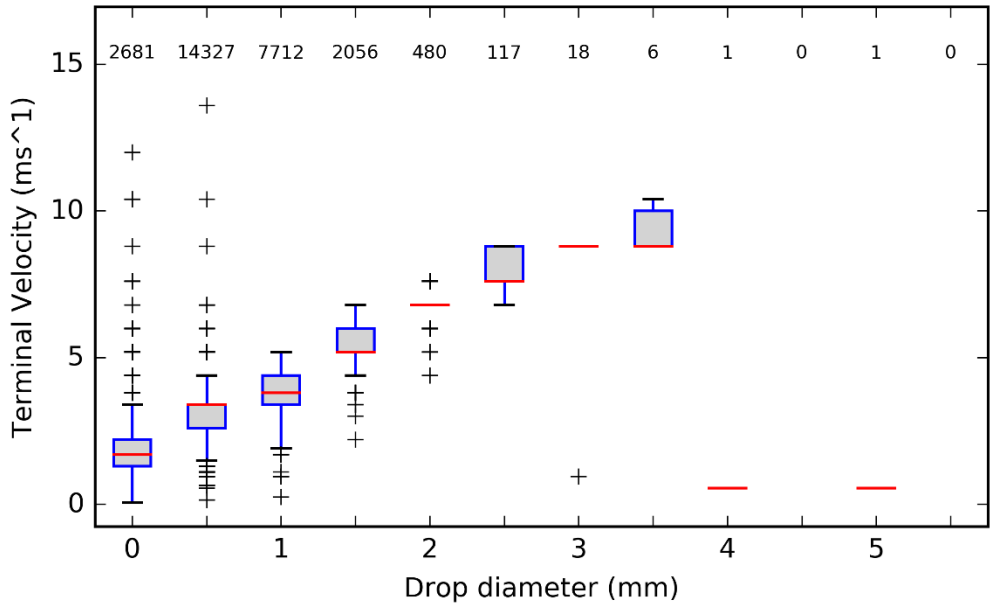

Figure 5.8: Drop velocity distribution conditioned on drop size, observed on the night of August 11, 2016.

Figures 5.7 and 5.8 suggest that terminal velocity vs drop diameter curves which can be reasonably approximated by power law. This is an assumption made in estimating rainfall rate from the Rayleigh scattering law, from either the backscatter or the extinction cross section.

Radar Rainfall Accumulations

After the rainfall data from the XPOL's are processed, merged, and interpolated to 1-minute and 50m resolution in space and time, hourly rainfall accumulations are calculated. Hour accumulation was selected because it is a good compromise between the short time scales of a small watershed, appropriate for the temporal resolution of a tipping-bucket rain gauge. Rainfall was available from the gauges at an interval of 15 minutes as well.

In the SMAP campaign domain, there were 20 rain gauges available for collecting rainfall data at locations inside and outside of the South Fork Iowa River watershed. An initial look at the radar-gauge agreement can be done with the help of conditional boxplots. Figures 5.9-5.13 investigate the agreement, given 1-hour accumulation time, and given a rainfall estimate from K_{dp}, A_h, or corrected Z_h. Since the ground-based rain gauges are commonly viewed as a reference instrument for other methods of precipitation estimation, the boxplots in Figures 5.9-5.13 are conditional on observations within a bin of hourly accumulation. For the two weeks of SMAP-VEX phase 2, there were a limited number of occurrences of heavy rainfall, so the number of observations assigned to each bin is printed on the upper x-axis of the plot. It can be seen that the vast majority of hourly accumulations are below 10 mm, or ¼ inch. For these rainfall products, hourly accumulation was calculated by advecting the rainfall field using the advection correction method, to have data for both radars to have temporal resolution of 1 minute. These data were spatially merged over the experimental domain from the two radars,

averaging in the overlapped sectors. Finally, the data were accumulated for the entire hour, each minute slice added together, and spatial pixels over the gauge locations served as the accumulation estimate. Appendices D and E describe these processes.

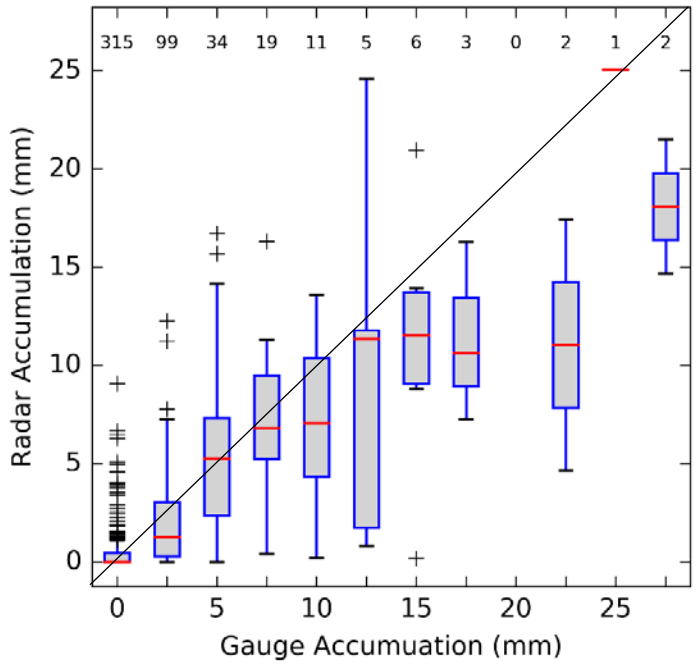

Figure 5.9: 1-hr Accumulated rainfall from K_{dp}-derived from the moving-window least-squares method: Numbers on the upper x-axis display the number of samples in each threshold bin.

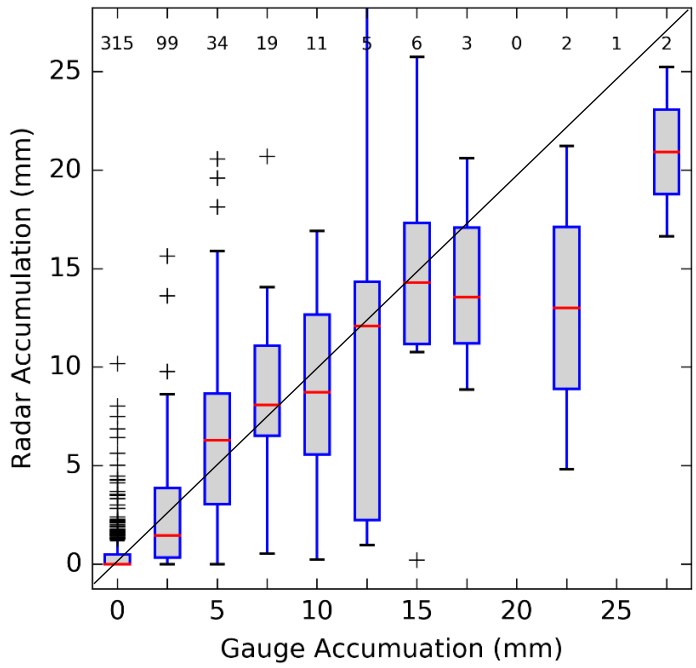

Figure 5.10: Specific Attenuation-derived rainfall accumulation vs gauge accumulation for all gauges in the basin, and all rain-producing 1-hr periods during Phase 2.

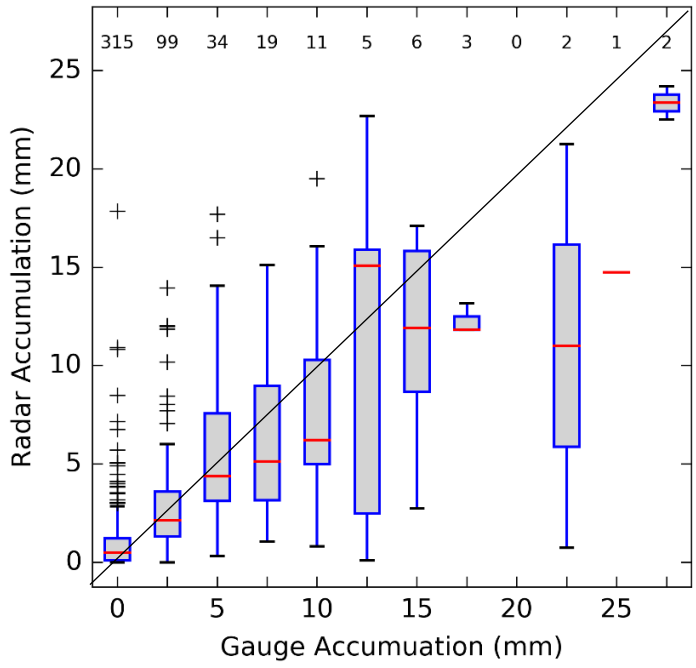

Figure 5.11: Corrected Reflectivity-derived rainfall accumulation vs gauge accumulation for all gauges in the basin, and all rain-producing 1-hr periods during Phase 2.

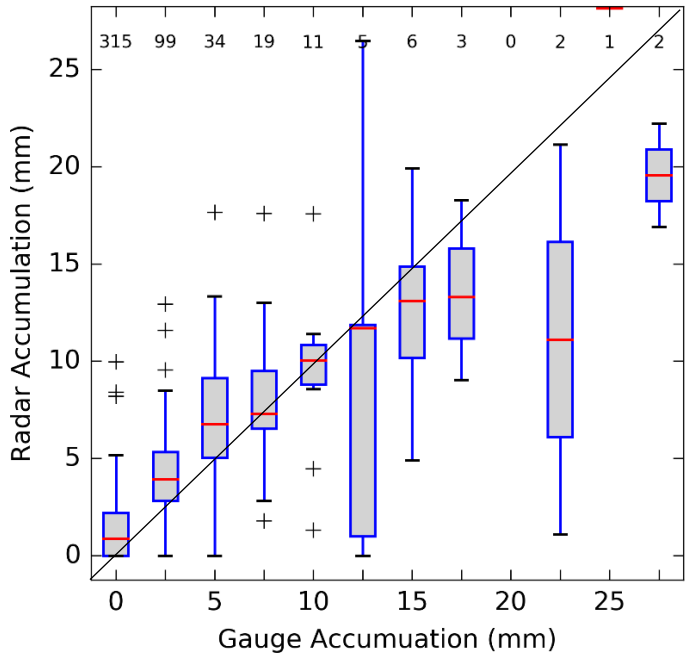

Figure 5.12: Kalman-filter K_{dp} derived rainfall accumulation.

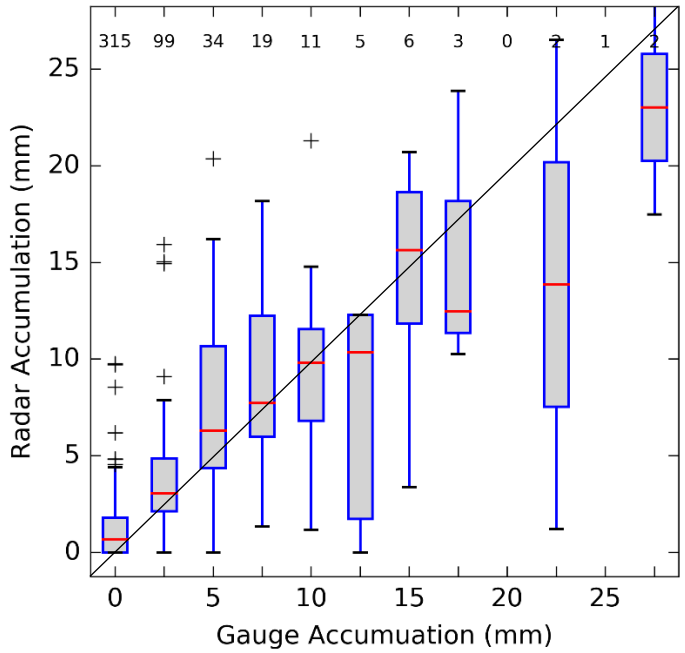

Figure 5.13: Multi-parameter rainfall estimate suggested by Anagnostou et al (2004) used to compare with gauge-estimated rainfall.

The boxplots offer a summary of the radar-gauge data which indicates the dispersion of radar-algorithm derived rainfall estimates conditional on the amount of rainfall collected by the gauge. The red dashes in Figures 5.9-5.13 indicate the conditional median, the length of the box indicates the values higher than the first quartile, but less than the third quartile, and the whiskers extend to the last data point within 1.5 times the inter-quartile range from the median. Crosses indicate data lying beyond 1.5 times the interquartile range from the median. These data were collected such that 20 gauges provided 41 values of accumulation, leading to 820 observations across the domain. 423 of these observations had zero accumulation at the rain gauge, which is not included in Figures 5.9-5.13. Numerical approaches for evaluating the precipitation products were inspired by the work of Cunha et al. (2015). The results of the evaluations are in the form of regression slope of the gauge-vs-radar plots, correlation between gauges and radar, the bias of the radar product relative to the gauges as reference, and the M.S.E. in Figures 5.14-5.17.

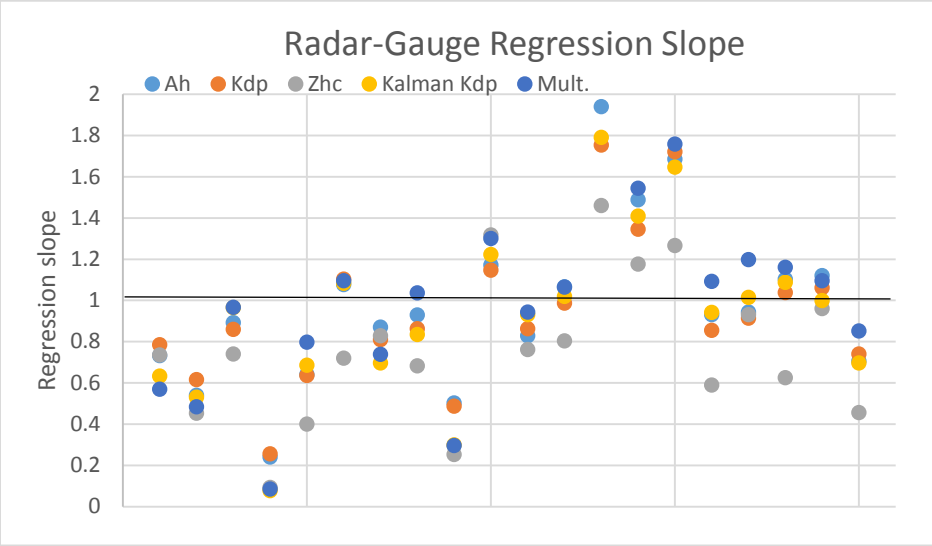

Figure 5.14: Regression slope in 1-hr accumulated rainfall observations at the 20 locations.

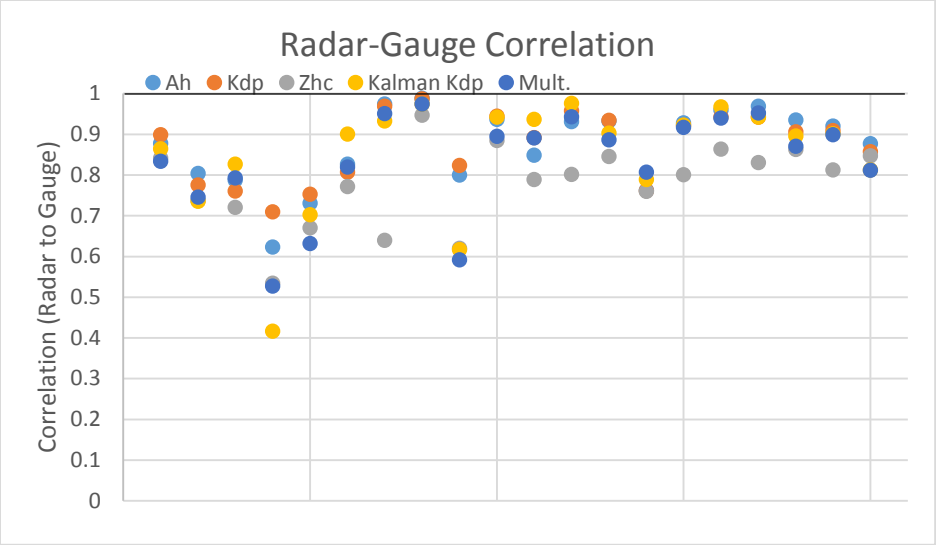

Figure 5.15: Correlation between radar and gauge observations at the 20 locations.

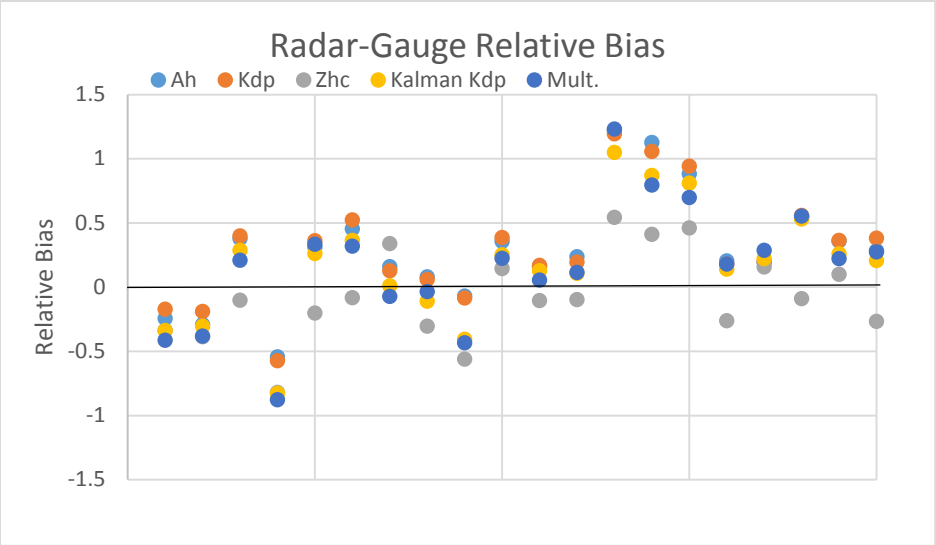

Figure 5.16: Relative Bias of the radar products' estimates of accumulated rainfall, relative to the gauges as a reference.

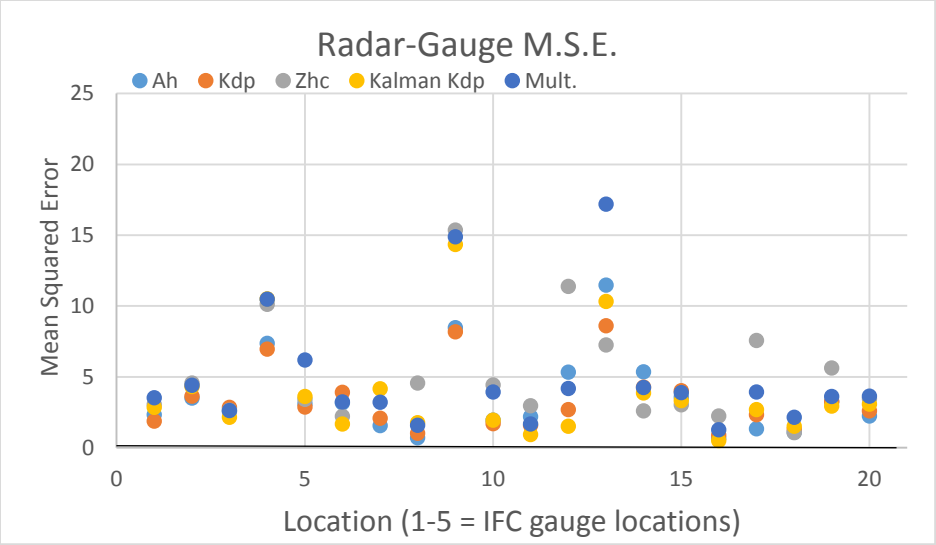

Figure 5.17: Mean-Squared Error of the radar products' estimates of accumulated rainfall, relative to the gauges as a reference.

Table 5.1: All-gauge average correlation, relative bias, and mean squared error for each rainfall estimator.

	Corrected Z	Regression Kdp	Kalman Filter Kdp	Specific attenuation	Multi-Parameter
Corr.	0.710	0.873	0.848	0.819	0.834
Rel. Bias	-0.33	0.305	0.176	0.035	0.165
MSE	8.369	3.338	3.905	4.042	4.997

Figures 5.18-5.22 illustrate the radar-gauge comparison on a gauge-by-gauge basis. The green line represents 1 to 1 correspondence, and the red line represents the least-squares regression fit of the comparison. The first row of 5 gauges in Figures 5.18-5.22 represent the IFC dual-tipping bucket gauges, and the remaining 15 are from the ARS gauge comparisons.

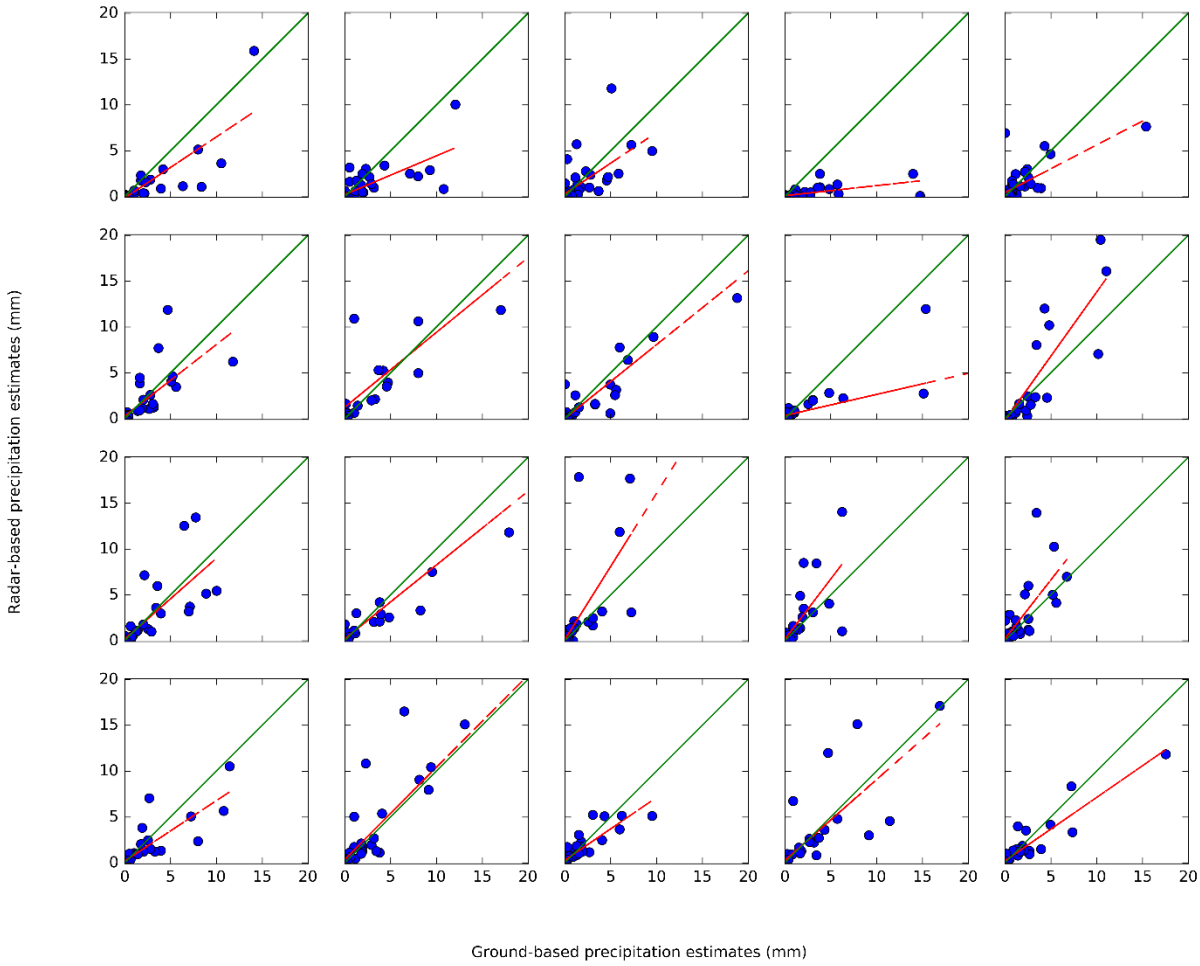

Figure 5.18: Gauge Comparison of 1-hr rainfall as a function of corrected reflectivity at all 20 gauges, calculated by integrating the specific attenuation, from the ZPHI method.

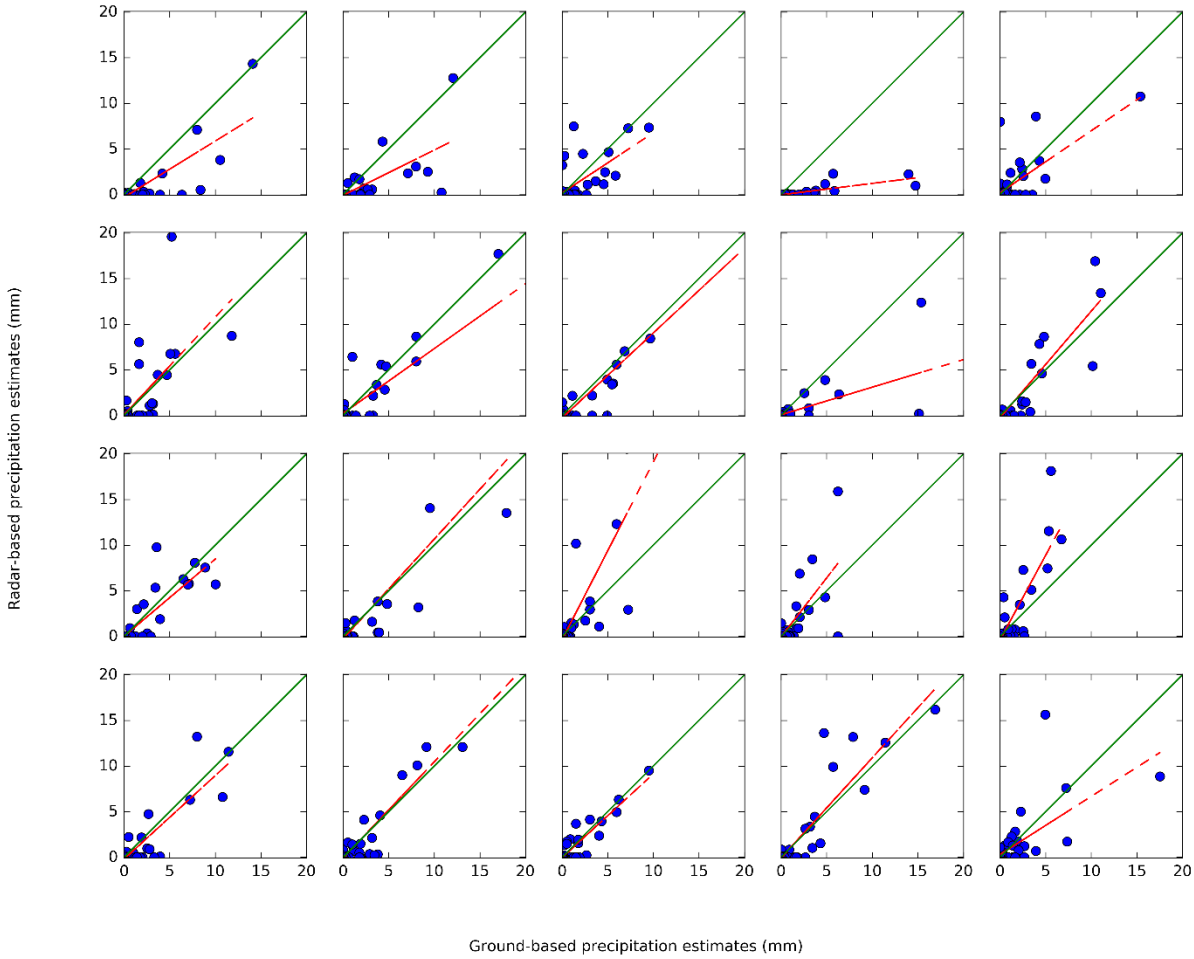

Figure 5.19: Gauge comparison of 1-hour rainfall accumulation as a function of Specific attenuation, Calculated by the ZPHI method, and K_{dp} estimated by moving-window least-squares regression.

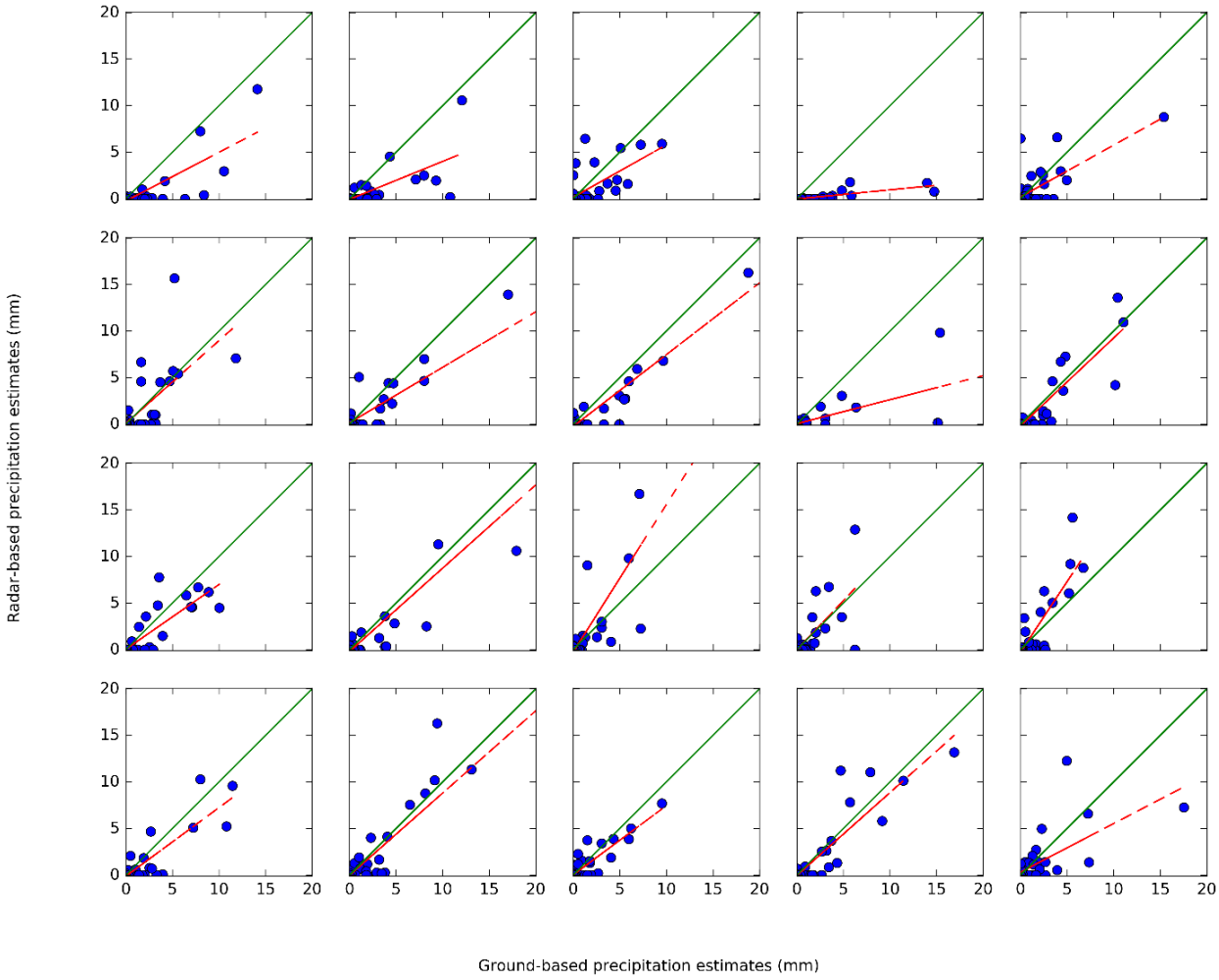

Figure 5.20: Hour accumulation comparison based on the moving-window least-squares regression method of calculating K_{dp}.

The multi-parameter method assimilates information from other dual-pol moments, but still heavily relies on K_{dp}. Corrected Reflectivity and Z_{dr} are used in calculation of rainfall, and this product performs nearly as well as Kalman-filter K_{dp}. The multi-parameter rainfall algorithm's performance is shown in Figure 5.22.

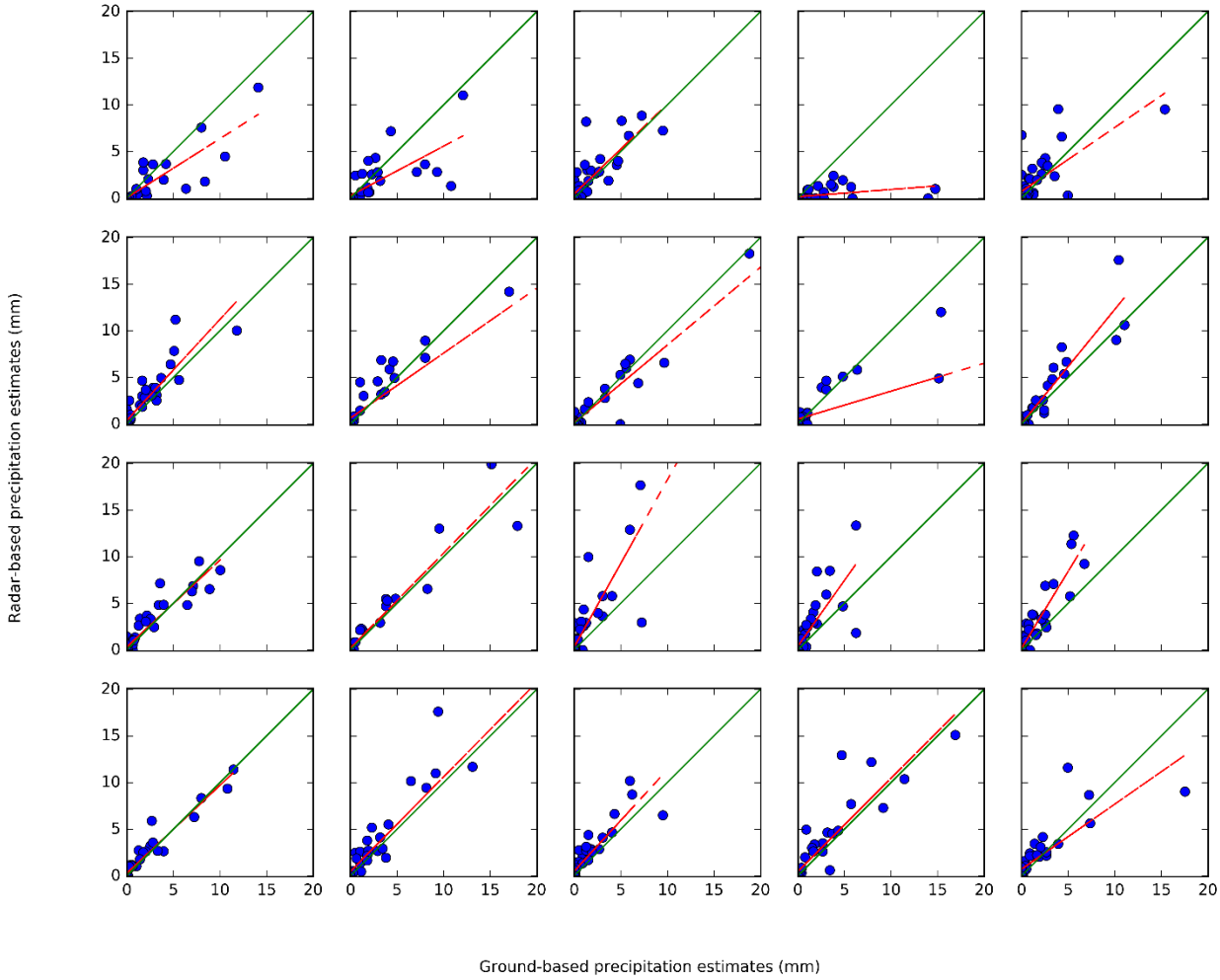

Figure 5.21: 1-hour accumulation comparison for Kalman-filtered K_{dp}.

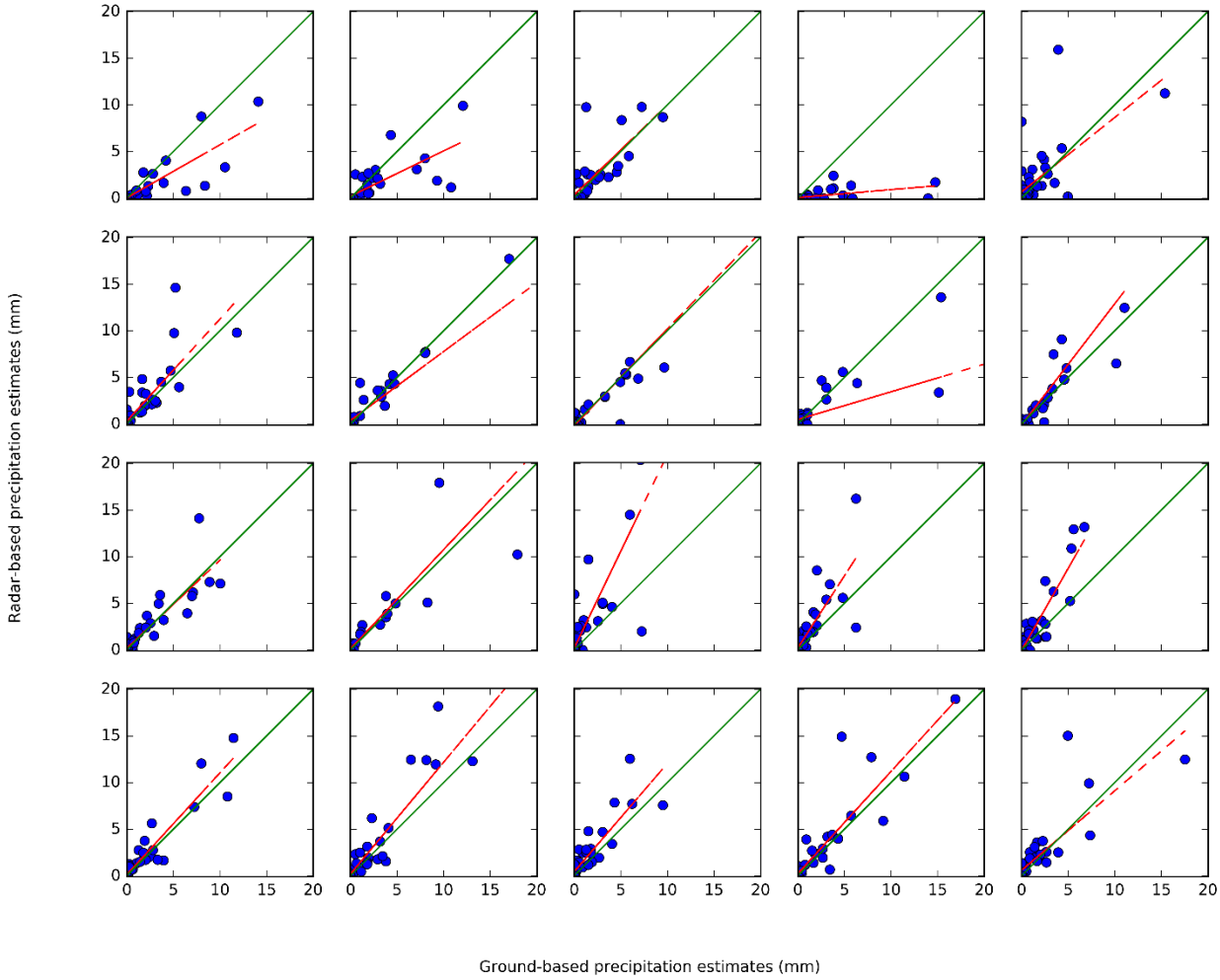

Figure 5.22: 1-hour accumulation comparison using the multi-parameter estimation method suggested by Anagnostou et al (2004).

6. DISCUSSION AND CONCLUSIONS

The results in chapter 5 suggest there are ways to effectively overcome the attenuation effects suffered by X-band radars, and estimate rainfall with high correlation to ground references, low bias, and acceptable discrepancy over a watershed like the South Fork Iowa River. These steps for overcoming attenuation were assembled into a radar-rainfall algorithm for the Iowa Flood Center's X-pol radar network. The best-performing methods exploited the self-consistency relationships between different radar moments. In other words, each radar product says at least one specific thing about the rainfall the radar pulse encounters. The best algorithms utilize the strong suits of these individual products to infer the rainfall rate.

Applying the Kalman filter technique for computing K_{dp} caused the dispersion of radar estimates to decrease slightly. We also notice in Figure 5.16 that the Kalman filter technique reduces the relative bias at most of the rainfall gauge locations. The variability and bias expanded with the corrected reflectivity estimates of rainfall. In fact, corrected reflectivity performed the worst of all the products. The estimation of specific attenuation had its own uncertainty involved. Since correcting reflectivity is solving an ordinary differential equation, the uncertainty propagates to the rainfall estimates rather severely.

On a gauge-by-gauge basis, some locations correlate more strongly to the radar estimations than others. Figure 5.15 indicates the correlations of individual gauges with the radar estimates. Some individual gauges stand out in Figure 5.15 as low spots, usually coinciding with cases where dual coverage from the radars was unavailable. It is also apparent that estimating rainfall directly from K_{dp} or specific attenuation is preferable to correcting reflectivity and then estimating rainfall.

The limits of the axes in Figures 5.18-5.22 are from 0 to 20 mm, as the short 2-week study period available did not allow for very many hourly totals of rainfall larger than an inch. Again, we can see a negative bias and large variability in the radar estimates in the corrected reflectivity cases. Specific attenuation and K_{dp} lead to better results, with the regression slope closer to 1, and the variability smaller. The moving-window least-squares methods are not as true to the spatial variability of rainfall cells. Those methods also neglect truly accounting for the backscatter differential phase shift in a theoretically sound way, which Kalman filtering does.

Three of the 20 rain gauges did not have coverage from both radar units. All of them were permanent Iowa Flood Center rain gauge stations, and are the first, second, and fourth plots in the first row of the arrays in Figures 5.18 – 5.22 gauge number 4 in the first row shows the heaviest toll of single-radar coverage. Gauge number 4 was only visible from Xpol South, but it was 38 km away, which is nearly on the edge of the visibility range. Gauges 1 and 2 are not in that extreme of a lack of radar coverage, but do indeed show a negative bias. Gauges 13, 14, and 15 were ARS gauge locations. These gauges show a positive bias in radar rainfall. This result has two possible explanations.

The first explanation is that the radar simply overestimated the rainfall, making inferences based on observations far above the ground, which were not true close to ground level. However, these locations are outside the area where ground clutter enhancement of accumulated rainfall is expected.

The other explanation is that the gauge is under-reporting the total rainfall due to bio-fouling, or mechanical issues, as this was the data for phase 2 of the experiment, and the gauges had been deployed for 2 months leading up to that time.

In conclusion, it was shown that algorithms relying on phase-based estimates of rainfall perform slightly better in the sense that they exhibit low mean squared error, and correlate well with the gauge estimates. Although the corrected reflectivity was not the best product, it still displayed low relative bias. Hopefully, researchers will use this thesis as a guide to estimating rainfall from X-band radars, and actionable hydrologic alerts and warnings can be made because of it.

REFERENCES

Anagnostou, E. N., M. N. Anagnostou, A. Kruger, W. F. Krajewski, and B. Miriovsky, 2004: High-resolution rainfall estimation from X-band polarimetric radar measurements. *J. Hydrometeor*., **5**, 110–128.

Atlas D., and Ulbrich C. W., 1977: Path and area-integrated rainfall measurement by microwave attenuation in the 1-3 cm band. *J. Appl. Meteorol.* **16**, 1322-1331.

Bringi, V. N., and V. Chandrasekar, 2001: Polarimetric Doppler weather radar: principles and applications. *Cambridge University Press*, 636 pp.

Colliander A., M. H. Cosh, S. Misra, T. J. Jackson, W. T. Crow, S. Chan, R. Bindish, C. Chae, C. H. Collins, S. H. Yueh, 2017: Validation and scaling of soil moisture in a semi-arid environment: SMAP validation experiment 2015 (SMAPVEX15). *Remote Sensing of the Environment* **196**, 101-112.

Cunha L., J. A. Smith, W. F. Krajewski, M. L. Baek, and B. C. Seo, 2015: NEXRAD product evaluation for IFloodS. *Journ of Hydrometeor*, **16**, 1676-1699.

Diederich, M, A. Ryzhkov, C. Simmer, P. Zhang, and S. Trömel, 2015: Use of specific attenuation for rainfall measurement at X-band radar wavelengths. Part I: radar calibration and partial beam blockage estimation. *Journ of Hydrometeor*, **16**, 487-502.

Doviak, R., & Zrnic, D., 2006: Doppler radar and weather observations (2nd ed.). Reprint, Mineola, NY: Dover. 562pp.

Georgiou, S., 2010: Estimation and assessment of differential and specific differential phase with the IDRA X-band Doppler polarimetric radar. M.S. thesis. Delft University of Technology. 105 pp.

Hitschfeld, W., and J. Bordan, 1954: Errors inherent in the radar measurement of rain fall at attenuating wavelengths. *Journ. of Meteor.*, **11**, 58–67.

Hubbert, J. V., and V. N. Bringi, 1995: An iterative filtering technique for the analysis of coplanar differential phase and dual-frequency radar measurements. *J. Atmos. Oceanic Technol.*, **12**, 643–648.

Huff, F. A., and W. L. Shipp, 1969: Spatial correlations of storm, monthly and seasonal precipitation. *Journ.of App.Met.*, **8**(4), 542-550.

Kalman, R. E., 1960: A new approach to linear filtering and prediction theory. *Trans. ASME, Journ. Basic Eng.*, **82**, 1, 35-45.

Keenan, T. D., L. D. Carey, D. S. Zrnic´, and P. T. May, 2001: Sensitivity of 5-cm wavelength polarimetric radar variables to raindrop axial ratio and drop size distribution. *J. Appl. Meteor*., **40**, 526–545.

Lee, G., Zawadzki, I., Szyrmer, W., Sempere-Torres, D., and Uijlenhoet, R., 2004: A general approach to double moment normalization of drop-size distributions, *Journ. of App. Met.* **43**, 264-281.

Mandapaka, P. V., W. F. Krajewski, G. J. Ciach, G. Villarini, J. A. Smith 2009: Estimation of radar-rainfall error spatial correlation. *Adv. In Water Resources.* **32**, 7, 1020-1030.

Market, P. S., A. R. Lupo, C. E. Halcomb, F. A. Akyz, and P. Guinan, 2001: Overview of the 7 May 2000 extreme rain event in Missouri. preprints, symp. on precipitation extremes: prediction, impacts, and responses, Albuquerque, NM, *Amer. Meteor. Soc*., 162–165.

Matrosov S., K. A. Clark, B. E. Martner, A. Tokay, 2002: X-band polarimetric radar measurements of rainfall. *Journ. of App. Met.* **41**, 941-952.

Marshall, J.S., and Palmer W. (1948). The distribution of raindrops with size. *J. Meteor.* **5**, 165-166.

McNairn, H. T.J. Jackson, C. Wiseman, S. Belair, A. Berg, P. Bullock, A. Colliander, M. Cosh, S-B. Kim, R. Magagi, M. Moghaddam, I. G. Njoku, J. R. Adams, S. Homayouni, E. R. Ojo, T. L. Rowlandson, J. Shang, K. Goita, M. Hosseini, 2015: The soil moisture active passive validation experiment 2012

(SMAPVEX2012): prelaunch calibration and validation of the SMAP soil moisture algorithms. *IEEE Transactions on Geoscience and Remote Sensing*. **53**, 5, 2784-2801.

Mishra, K.V., W.F. Krajewski, R. Goska, D. Ceynar, B.-C. Seo, A. Kruger, J. J. Niemeier, M. B. Galvez, M. Thurai, V. N. Bringi, L. Tolstoy, P. A. Kucera, W. A. Petersen, J. Grazioli, and A. L. Pazmany, 2016: Deployment and performance analyses of high resolution Iowa XPOL radar system during the NASA IFloodS campaign. *Journ. of Hydrometeor.*, **17**, 455-479.

Oguchi T., 1983: Electromagnetic wave propagation and scattering in rain and other hydrometeors. *Proc. IEEE.* **71**, 1029-1078.

Panciera, R., J. P. Walker, T. J. Jackson, D. A. Gray, M. A. Tanase, D. Ryu, A. Monerris, H. Yardlwy, C. Rudiger, y. Wu, Y. Gao, and J. M. Hacker, 2014: The soil moisture active passive experiments (SMAPEx): toward soil moisture retrieval from the SMAP mission. *IEEE Transactions on Geoscience and Remote Sensing*. **52**, 1, 490-507.

Park, S., M. Maki, K. Iwanami, V.N. Bringi, and V. Chandrasekar, 2005: Correction of radar reflectivity and differential reflectivity for rain attenuation at X band. part I: theoretical and empirical basis. *Atmos. Oceanic Technol.*, **22**, 1621-1632.

Park S., M. Maki, K. Iwanami, V.N. Bringi, and V. Chandrasekar, 2005: Correction of radar reflectivity and differential reflectivity for rain attenuation at X band. part II: evaluation and application. *Atmos. Oceanic Technol.*, **22**, 1633-1635.

Pruppacher, H. R., and K. V. Beard, 1970: A wind tunnel investigation of the internal circulation and shape of water drops falling at terminal velocity in air. *Quart. J. Roy. Meteor. Soc.*, **96**, 247– 256.

Ryzhkov, A., M. Diederich, P. Zhang, and C. Simmer, 2014: Potential utilization of specific attenuation for rainfall estimation, mitigation of partial beam blockage, and radar networking. J. *Atmos. Oceanic Technol.*, **31**, 599–619.

Sachidananda, M. and D. S. Zrnic`, 1986: Differential propagation phase shift and rainfall rate estimation. *Radio Sci*., **21**, 235-247

Schneebeli, M., and A. Berne, 2012: An extended Kalman filter framework for polarimetric X-band weather radar data processing. *J. of Atmos. and Oceanic Tech.* **29**, 711-730.

Schneebeli, M., J. Grazioli, and A. Berne, 2014: Improved estimation of the specific differential phase shift using a complilation of Kalman filter estimates. *IEEE Trans. On Geosci. And Rem. Sens.* **52**, 8, 5137-5149.

Song, J., K. Liao, R. L. Coulter, and B. M. Lesht, 2005: Climatology of the low-level jet at the southern Great Plains atmospheric boundary layer experiments site. *Journ. of App. Met.* **44**, 1593-1606.

Testud, J., E. Le Bouar, E. Obligis E, and M. Ali-Mehenni, 2000: The rain profiling algorithm applied to polarimetric weather radar. *J. Atmos. Oceanic Technol*., **17**, 332–356.

Trabal, J. M., E. Gorgucci, V. Chandrasekar, and D. J. McLaughlin , 2014: Evaluation of the self-consistency principle for calibration of the CASA radar network using properties of the observed precipitation medium. *IEEE Trans. on Geosci. and Remote Sensing* **52**, 1, 149-162.

Ulbrich C. W., 1983: Natural variations in the analytical form of the raindrop-size distribution. *J. Clim. App. Meteorol.* **22**, 1764-1775.

Ulbrich C. W. and Atlas, D., 1984: Assessment of the contribution of differential polarization to improved rainfall measurements. *Radio Sci.* **19**, 49-57.

Vivekanandan, J., D. N. Yates, and E. A. Brandes, 1999: The influence of terrain on rainfall estimates from radar reflectivity and specific propagation phase observations. *J. Atmos. Oceanic Technol.*, **16**, 837–845.

Zrnic´, D. S., and A. V. Ryzhkov, 1996: Advantages of rain measurements using specific differential phase. *J. Atmos. Oceanic Technol.*, **13**, 454–464.

Appendix A. Calculating the Radar Moments

One way or another, all radar-derived products depend on aspects of the electric field of a traveling electromagnetic pulse. The magnetic field vector also exists, but is not focused on as much because it is very small in scale compared to the electric field component. Phasor notation is a convenient way to describe the size and direction of an electric field vector due to a pulse traveling radially from the antenna in the direction *r*.

$$\vec{E} = \frac{\vec{A}(\theta,\phi)}{r} e^{i2\pi f\left(t-\frac{r}{c}\right)+i\psi}, \tag{A.1}$$

where *A* is the wave amplitude, *f* is frequency, *c* is the speed of light $3*10^8$ ms^{-1}, *r* is the range distance covered by the wave, *t* is time, and ψ is the transmitter phase angle. *E* and *A* are written as vector quantities here because that style of treatment is useful when considering dual-polarimetric capable radars.

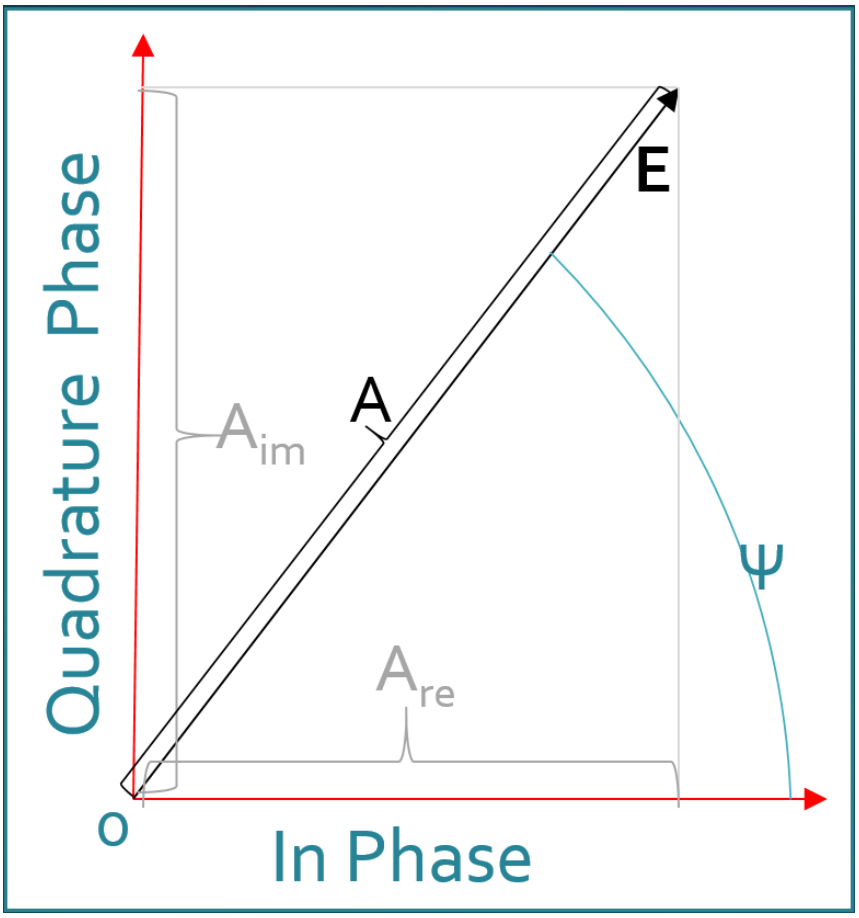

Figure A.1: An electromagnetic wave propagating through space, represented as a phasor diagram. The in-phase component represents the strength of the electric field at some time in space. The Quadrature phase component is an imaginary quantity, 90 degrees out of phase.

The power density reflected from some target in a medium is related to the electric field vector. Assuming Rayleigh scattering is not violated, we can get realistic estimates of how much power is returned per unit volume of air in the range resolution volume. This power density is described in equation A.2. Its rate of change in time and space is more closely related to the popular radar moments like reflectivity, Doppler velocity, and differential phase shift.

$$S = \frac{1}{2}\frac{\vec{E} * \vec{E}^{*}}{\eta_0} = \frac{1}{2}\frac{\left|\vec{A}\right|^2}{\eta_0 r^2}, \qquad \text{(A.2)}$$

where E^* is the complex conjugate of E. This power density is a function of space and time, and is collected by the receiving antenna, and transferred to voltages in electric channels within the radar unit. The magnitude and rates of change of these voltages are used to make rainfall rate estimations.

A revolutionary observation of water droplets in a wind tunnel (Pruppacher and Beard 1970) revealed the tendency of larger raindrops to become wider as their volume increases. This is due to an imbalance between water's surface tension, and shearing forces due to aerodynamic drag on falling raindrops. Shown in Figure A.4, aerodynamic drag inevitably leads to geometric anisotropy with respect to the face of falling raindrops as seen from an approaching EM wave. This geometric anisotropy leads to different thicknesses of the drop in places, as well as different degrees of liquid interface curvature relative to horizontally and vertically polarized incoming waves. Polarimetric radar was suggested as a way to take advantage of this anisotropy, in a search to better-quantify rainfall rates. Polarimetric radar is all about spatial orientation of the electric field component of an E-M wave, shown in Figures A.2, and A.3. Depending on the media characteristics along the propagation path, waves polarized vertically may react differently than waves polarized horizontally. If these two polarizations are emitted simultaneously, and at the same frequency, then the electric field component is the vector sum of these two polarizations, and in this example, would be oriented 45 degrees from vertical. If the pulses are emitted at different times, or characteristics of the propagation medium affect the two

polarizations differently, then the electric field vector may rotate as the pulse propagates through space. A special case of this phenomenon is called "right hand circular" polarization, and is utilized by some radar units.

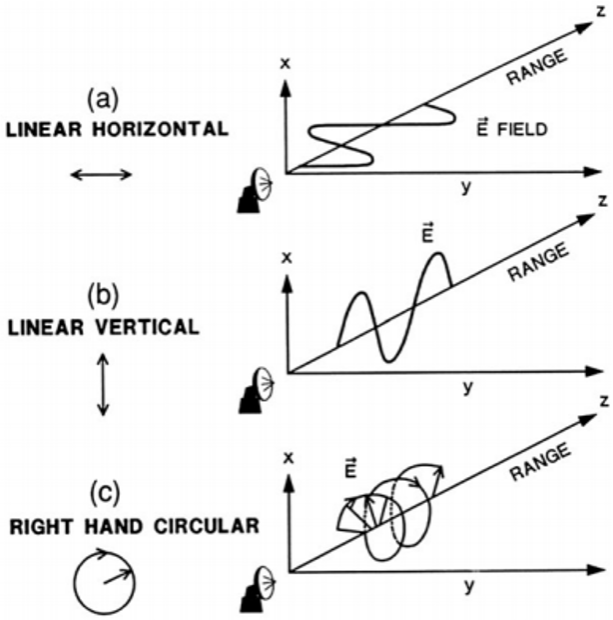

Figure A.2: an illustration of the spatial concept of a polarized electromagnetic wave, from Doviak and Zrnic (2006).

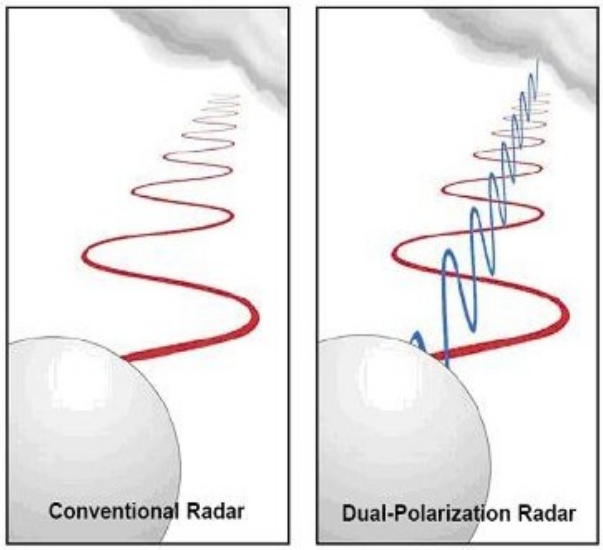

Figure A.3: Illustration of dual-polarization: The waves represent the electric field component of an E-M wave. Red is horizontally polarized, blue is vertically polarized. Credit: washingtonpost.com.

The usefulness of dual-pol moments is that operators can choose the polarization directions coming from the radar antenna, and analyze the returning signal characteristics to infer something about the propagation medium e.g. presence or intensity of precipitation. Researchers generally agree that dual-polarization capability improves estimation of rainfall rate via radar. (Ulbrich and Atlas 1984)

Equations A.3-A.7 show the expressions for the strength of the electric field, with the components in the horizontal and vertical polarizations as vector elements.

$$\begin{bmatrix} E_h^r \\ E_v^r \end{bmatrix} = \frac{e^{-ik_0 r}}{r} \begin{bmatrix} -1 & 0 \\ 0 & 1 \end{bmatrix} \begin{bmatrix} S_{hh} & S_{hv} \\ S_{vh} & S_{vv} \end{bmatrix}_{FSA} \begin{bmatrix} E_h^i \\ E_v^i \end{bmatrix} \tag{A.3}$$

$$S_{hh} = \frac{k_0}{4\pi}\left(\frac{\varepsilon_r - 1}{\varepsilon_r + 2}\right) 3V\cos(\phi_s) \tag{A.4}$$

$$S_{hv} = \frac{k_0}{4\pi}\left(\frac{\varepsilon_r - 1}{\varepsilon_r + 2}\right) 3V(-\sin(\phi_s)) \tag{A.5}$$

$$S_{vh} = \frac{k_0}{4\pi}\left(\frac{\varepsilon_r - 1}{\varepsilon_r + 2}\right) 3V\cos(\theta_s)\sin(\phi_s) \tag{A.6}$$

$$S_w = \frac{k_0}{4\pi}\left(\frac{\varepsilon_r - 1}{\varepsilon_r + 2}\right) 3V\cos(\theta_s)\cos(\phi_s), \tag{A.7}$$

where k_0 is the wavenumber, V is the volume of the non-spherical scatterers, θ_s and ϕ_s describe the raindrop canting angle in space. The square of the above power densities observed by the radar is proportional to the so-called back-scattering cross-section.

The backscattering cross section is a convention used to quantify size of an object needed to scatter the same power back to the radar from a given distance, and a given power density, as if it was an isotropic scatterer. An isotropic scatter radiates in all directions, without the focusing qualities of a parabolic antenna. It is an idealized situation, used in electromagnetic theory discussions to serve as a reference power level compared to that of some antenna.

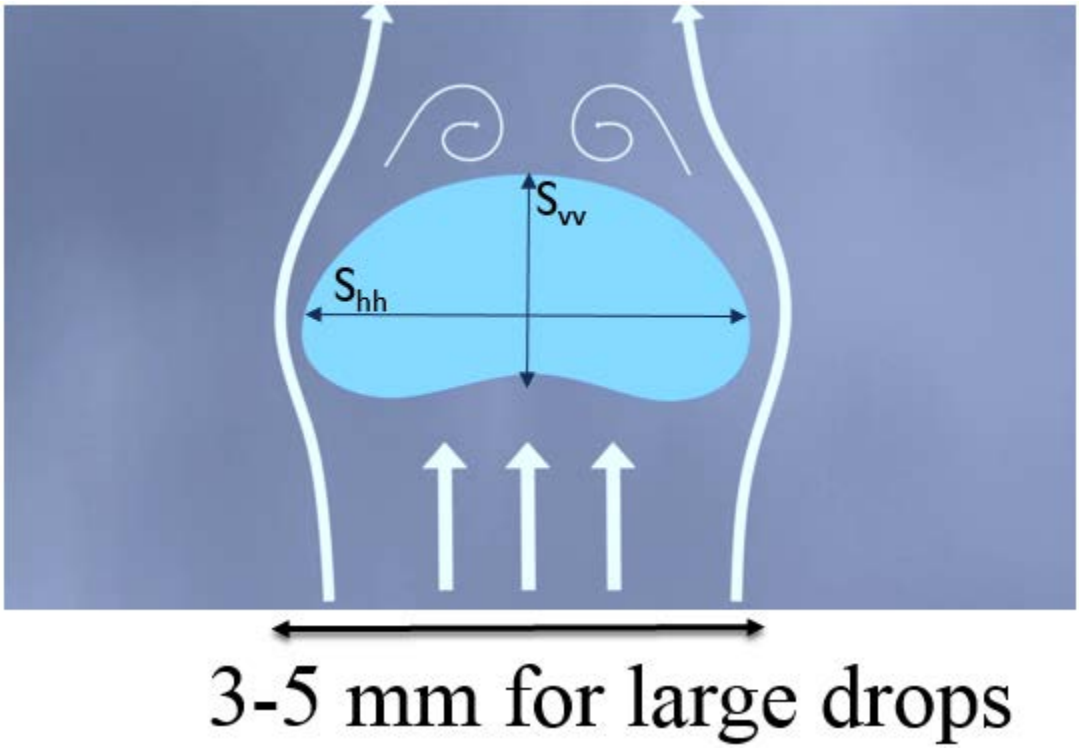

Figure A.4: Diagram showing aerodynamic drag, which deforms large raindrops. The horizontal scattering power density Shh comes from the horizontal axis, and the vertical scattering power density Svv comes from the vertical axis.

We obtain the classical radar equation by considering the power density at the moment of backscatter, and at the reflector location, and predicting its power signature after the pulse propagates back to the radar antenna. There are three important components to this: constant terms, radar system characteristics, and target characteristics. The constants come from unavoidable beam spreading with distance, the system characteristics are predictable, and are based on the physical parameters of the antenna and carrier wavelength, and most importantly, the target characteristics are what we infer. What we receive at the radar is power density, shown in equation A.8.

$$P_r = \left(\frac{P}{A}\right)_{raindrop} \sigma_{raindrop} \left[losses \propto \frac{1}{4\pi r^2} \right] \left[A_{eff} \propto \frac{G\lambda^2}{4\pi} \right], \tag{A.8}$$

where A is the cross-section area of the radar beam as a function of range, G is the antenna Gain, and P is the power transmitted, equation A.8 reduces to a very general form of the radar equation

$$\mathrm{P}_r = \frac{P_t G^2 \sigma_t \lambda^2}{64\pi^3 r^4}\ , \tag{A.9}$$

where σ_t depends on the hydrometeors in the propagation medium, scattering the pulse back to the radar. All other parameters are either measured or a designed characteristic of the radar system. In order to understand how σ_t relates to the actual size of a scatterer, Rayleigh scattering is assumed, where the scattering cross section is proportional to the size of a spherical target.

$$V * \sigma = \frac{c\tau\pi\theta_{beam}^2}{2(4)(2\ln 2)} * \frac{\pi^5 |k|^2 D^6}{\lambda^4}, \quad \text{(A.10)}$$

where k is the dielectric constant of the target material, D is the diameter of a spherical scattering body, and λ is the wavelength of the incident radiation.

The size of the radar resolution volume depends on the pulse interval time τ, and the beam width, θ_{beam}, using the small angle approximation. The length is the distance traveled by the pulse in time τ, and its width is defined by the angle outward from the beam center, where the intensity of the electromagnetic pulse is ½ that at the center.

The Rayleigh scattering assumption is valid in practice when the wavelength is much larger than the size of the scatterer. In the real world, this is not always valid, and the consequences of this are the motivation for developing certain steps in and X-band radar-rainfall algorithm.

For a resolution volume consisting of many particles, we are interested in the sum of the backscattering cross sections in that volume. Therefore, we replace σ_t with the sum of σ_t times the volume of space illuminated by the radar beam. The depth of the volume is the distance a pulse travels in its pulse interval time, and the area is a near-cylinder with diameter equal to the distance from maximum radiation intensity to 1/2 maximum radiation intensity. This definition is by convention.

$$\sigma_t \approx \sum_i \sigma_i = \frac{\pi^5 |k|^2}{\lambda^4} \sum_i D_i^6, \quad \text{(A.11)}$$

To break down the definition of σ_t further requires a probability model of how common or rare a given raindrop diameter is in the real world. This topic is important, and covered in chapter 4. A commonly used version of the radar equation for hydrologists is described in A.12.

$$P_t = \frac{\pi^3 P_t G^2 \theta_{beam}^2 c\tau |k|^2 Z_e}{1024(\ln 2) r_0^2 l^2 l_r}, \tag{A.12}$$

where l involves a weighting function along the length of the resolution volume, and Z_e is the equivalent reflectivity, or the range-adjusted power density at the reflecting target. Z_e is one of the most popular and well-known parameters used to estimate rainfall rate, especially after the work of Marshall and Palmer (1948). This is all possible because the radar is capable of estimating the received power from the scattering matrix components.

At each radar range gate, the radar collects samples from every point inside the resolution volume, which arrive as a time series because of light's constant speed through the medium. The numerous time series are summed together to reflect the characteristics of all reflectors in the resolution volume. The effect is just like ensemble averaging, and is described in equation A.13

$$P_{h,v}^r(r) = \sum_{m=1}^{M} \left| S_{h,v}(m,r) \right|^2, \tag{A.13}$$

where M is the number of signals taken for averaging, m is the number of a particular signal observation, and r is radar range. This is why Z_e is considered an amplitude-based product, as it is estimated by the ensemble-averaged amplitude of the E-M wave backscattered by a target.

Propagation Effects

Although the scattering qualities of the propagation medium can shed insight on the presence of rainfall, the way the electric field changes in space also can indicate rainfall intensity. This information is also very useful when estimating the velocity of reflecting particles, as the Doppler Effect will change the phase of a returning wave from a moving source. Of particular interest is how the phase of the received vertically and horizontally polarized signals change in space. As a consequence of Faraday's law, the electromagnetic wave moving through an intrusion in the medium with a different refractive index, and electrical permittivity, will slow down, and its phase will lag slightly compared to a situation where the intrusion was not present. By exploiting this effect in two different polarization channels, the geometric anisotropy of large raindrops can be backed out.

The Transmission Matrix, **T**, is the focus of the following section because it reflects the effects of the wave propagating through the storm, the effects on phase by backscattering, and the phase difference internal to the radar system.

The Relations in (A.3-A.7) describe the behavior of an incoming E-M wave scattering back to the radar antenna from one location in particular. Now, we are interested in how to relate the range derivative of the electric field strength to the exact way the radar emitted the wave. Bringi and Chandresekar (2001) describe the process where researchers try to solve for a theoretical matrix **B** which when defined at any distance from the radar describes the conditions the wave encountered on its way to the resolution volume. This scheme is known in the literature as the "transmission matrix" or "T-matrix" method. Elements of this matrix describe phase-shifting, attenuation, and the degree of polarization of the pulse after while it propagates downrange.

$$\frac{d}{dr}\begin{bmatrix} E_h^r \\ E_v^r \end{bmatrix} = \mathbf{B}\begin{bmatrix} E_h^t \\ E_v^t \end{bmatrix} \tag{A.14}$$

$$\begin{bmatrix} E_h^r(r) \\ E_v^r(r) \end{bmatrix} = \mathbf{T}\begin{bmatrix} E_h^t(0) \\ E_v^t(0) \end{bmatrix} \tag{A.15}$$

B is used as a place holder to set up the relations in equation A.14. By integrating equation A.14, we arrive at a description of the electric field vectors throughout space, as a function of their initial conditions, and the matrix **T**, which contains information directly related to medium properties, affecting the pulse as it propagates through heterogeneous media. Solving equations A.1.15 and A.1.16 assumes a single scattering particle, which is not realistic.

$$\begin{bmatrix} E_h^r \\ E_v^r \end{bmatrix} = \frac{1}{r}\mathbf{T}\begin{bmatrix} -1 & 0 \\ 0 & 1 \end{bmatrix}\mathbf{S}_{FSA}\begin{bmatrix} E_h^i \\ E_v^i \end{bmatrix} \tag{A.16}$$

The elements of **T** are also influenced by a collection of reflecting particles, rather than one. To be totally correct, we would need to account for each individual drop's scattering matrix. However, to get a nearly-as-correct result, we can perform ensemble averages and define **T** based on the cumulative characteristics of the thousands of drops within the resolution volume. However, one consequence of this approach is that we are required to make assumptions about the statistical distribution of canting angles. These distributions could have a nonzero mean if there are high winds present.

The final solution for **T** is developed in Oguchi (1983). The elements of **T** are calculated by ensemble averages of power received in a particular pattern highlighted by Oguchi. The following collection of equations describes how to estimate the transmission matrix.

$$T_{hh} = e^{\lambda_1 r}\cos^2(\phi_s) + e^{\lambda_2 r}\sin^2(\phi_s) \tag{A.17}$$

$$T_{vv} = e^{\lambda_1 r}\sin^2(\phi_s) + e^{\lambda_2 r}\cos^2(\phi_s) \tag{A.18}$$

$$T_{vh} = T_{hv} = (e^{\lambda_1 r} - e^{\lambda_2 r})\sin(\phi_s)\cos(\phi_s) \tag{A.19}$$

$$\phi_s = \frac{1}{2}\arctan\left(\frac{2\langle S_{hv}\rangle}{\langle S_{hh}\rangle - \langle S_{vv}\rangle}\right) \tag{A.20}$$

$$\lambda_1 = -i\left[k_0 + \frac{i}{2}\left(\langle S_{hh}\rangle + \langle S_{vv}\rangle + \gamma\right)\right] \tag{A.21}$$

$$\lambda_2 = -i\left[k_0 + \frac{i}{2}\left(\langle S_{hh}\rangle + \langle S_{vv}\rangle - \gamma\right)\right] \tag{A.22}$$

$$\gamma = \sqrt{\left(\langle S_{hh}\rangle - \langle S_{vv}\rangle\right)^2 + 4\langle S_{hv}\rangle\langle S_{vh}\rangle}, \tag{A.23}$$

where ϕ_s is the canting angle of the drops, λ is the depolarization coefficient for the horizontal or vertical channel, and γ reflects the cross-coupling between the two received signals. (Bringi and Chandrasekar, 2001) Very specific signal characteristics are used to estimate the elements of the transmission matrix, and these estimates are used heavily in estimating differential propagation phase shift, Ψ_{dp}, based on the received in-phase and quadrature phase of an incoming signal. The following equation relies on phasor notation to explain the values contributing to an estimate of $\Psi_{dp.}$

$$\psi_{dp} = \arg\left(e^{2(\lambda_2 - \lambda_1)}\right) + \arg\left(\langle S_{hh}\rangle\langle S_{vv}\rangle\right) \quad , \tag{A.24}$$

where arg(*) signifies the angle of a phasor with respect to a reference.

The key point of equation A.24, is that if the necessary assumptions are met, Ψ_{dp} can be apportioned into a component of phase shifting due to the propagation through heterogeneous media, a component of phase shift from backscattering, and phase shift due to the radar system.

$$\psi_{dp} = \phi_{dp} + \delta_{dp} + c_{hardware}, \tag{A.25}$$

where Φ_{dp} is the phase shift due to propagating through the medium, δ_{dp} is the backscatter phase shift, and $c_{hardware}$ is a constant phase shift due to the radar hardware itself, generally constant.

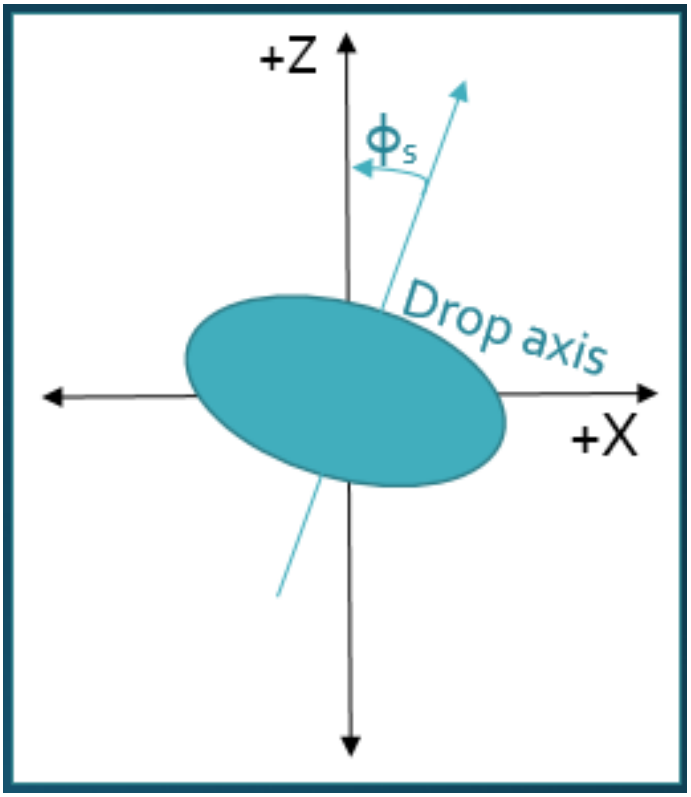

Figure A.5: Illustration of a raindrop's canting angle, ϕs.

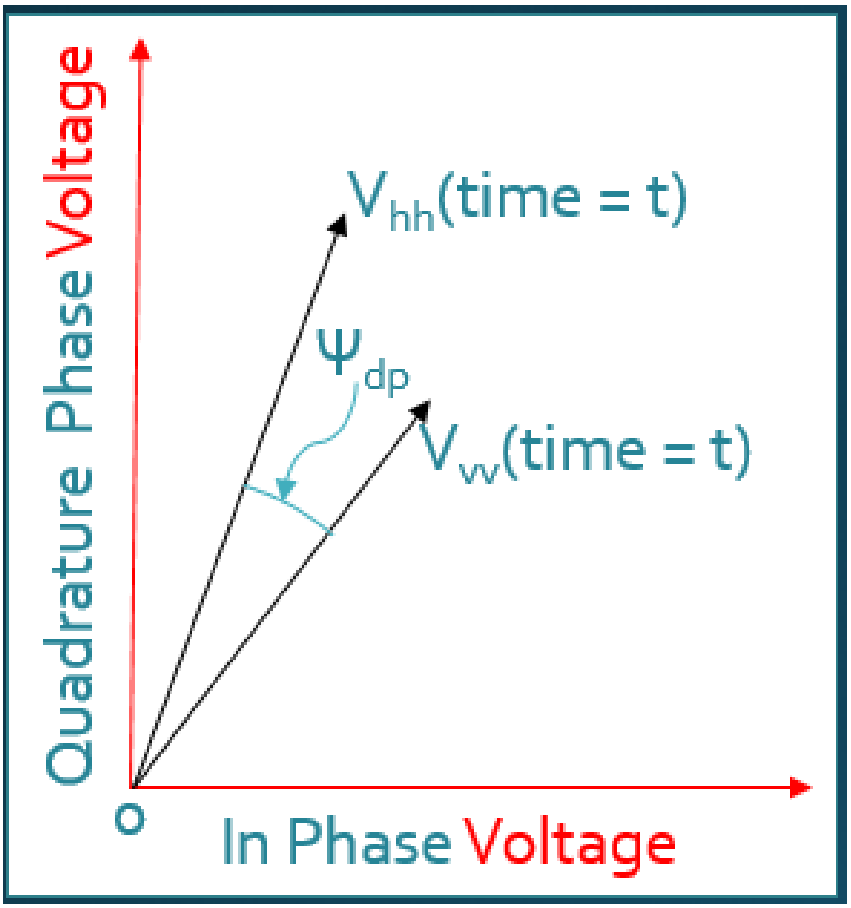

Figure A.6: An illustration of the calculation of Ψdp using phasor conventions, assuming canting angle is near zero.

The components of equation A.24 are chosen such that if the canting angle is set very small, and the drops are nearly spherical, the result of equation A.16 resembles that of A.3. The effects of phase shift are therefore said to be separate from those of scattering. Most of the interest in the transmission matrix lies in how Φ_{dp} changes with distance from the radar. Therefore, K_{dp}, the range derivative of Φ_{dp}, is often related to rainfall rate through some empirical relation. Since these estimates are phase-based rather than amplitude-based, they are used in a self-consistency framework, discussed more in depth in Trabal et al. (2014), which provides a reference for correcting the effects of attenuation in amplitude-based estimates.

Appendix B. Masking Noisy Data

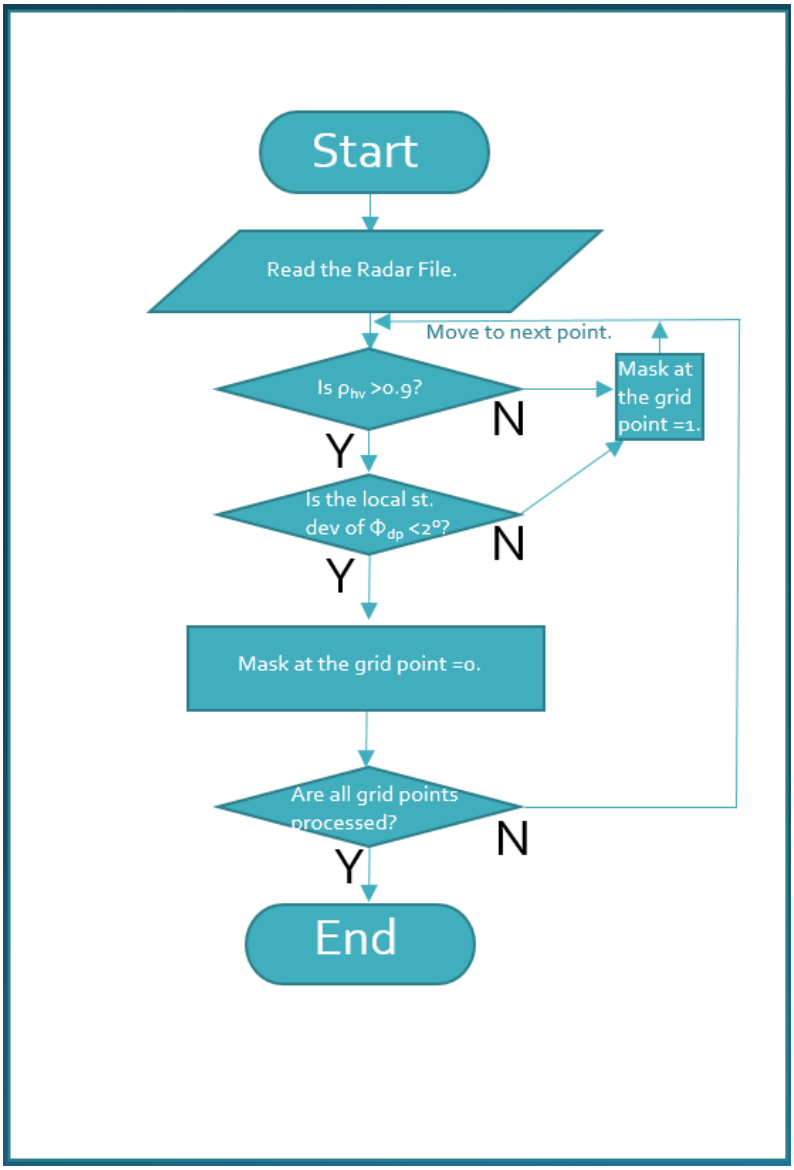

Figure B.1: Flowchart of the radar data masking of ground clutter and noisy Φdp data.

Appendix C. Cartesian Conversion

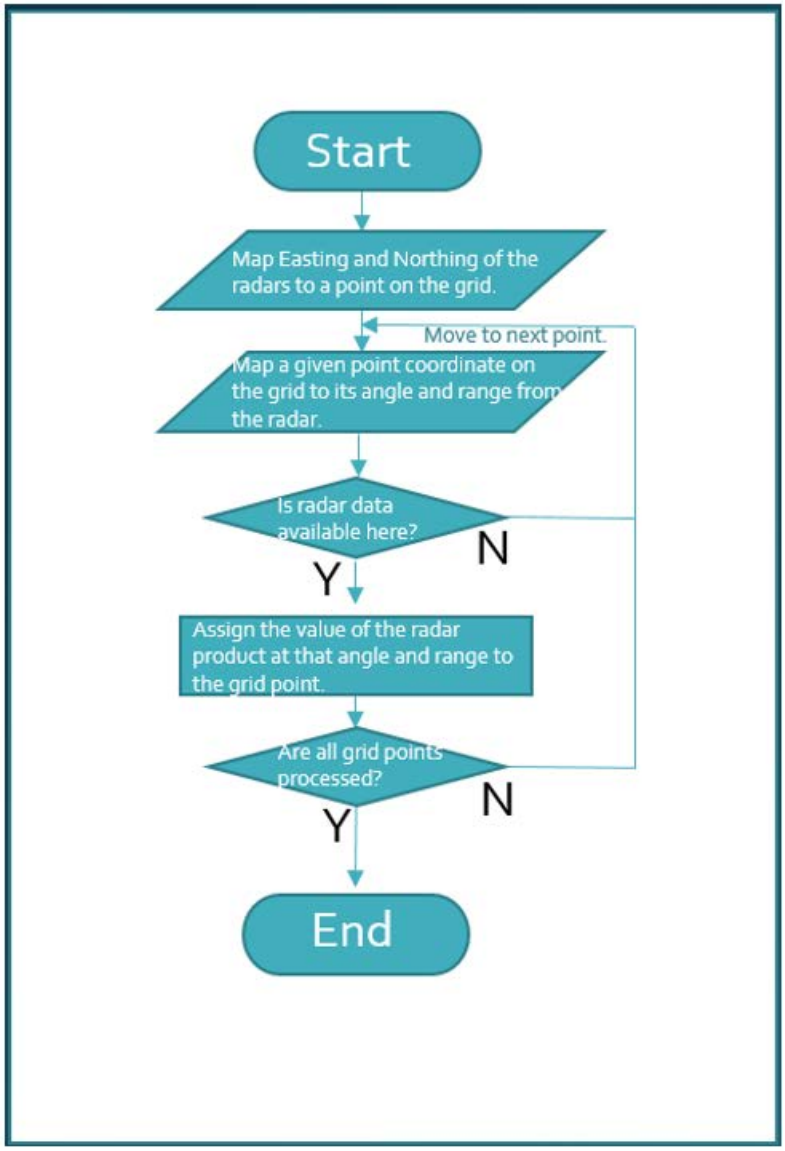

Figure C.1: Flowchart of the conversion from polar coordinates to Cartesian Coordinates.

Appendix D. Advection Correction

The purpose of executing an advection correction routine is rooted in the need for observations which are nearly continuous in time and space. The radar beam can be considered like a one dimensional line, scanning over a two dimensional area. For any given location in the SMAP-VEX domain, the radar only observes a 1.4 degree wide path. Therefore, if we are interested in all locations within the 2-D domain, we can consider each radar observation as a snapshot, with 2-3 minute latency in between. Advection correction allows researchers to "fill in" the observation gaps between snapshots by assuming that over short time periods, the evolution of rainfall fields is dominated by advecting cells, rather than convecting cells. An advection method similar to that used in Cunha et al. (2015) to generate a product on 5 minute intervals was modified to fit the smaller scale of the experiment domain, a 1- minute interval, and the two-radar configuration. The following steps are used for advection correction.

First, radar data taken on a polar coordinate system must be transformed to a Cartesian grid. This transformation simplifies the operations associated with advecting rainfall cells. A simple lookup table can be generated using geometry to link locations within the Cartesian grid to an azimuth and range relative to the radar. The table of these links assigns rainfall rate estimates from reflectivity, K_{dp}, or specific attenuation to Cartesian grid points. Next, the algorithm projects the rainfall field in the direction of a series of pre-defined advection vectors. These vectors represent the possible wind velocities a researcher can expect during rainfall. The resulting rainfall field which correlates most closely with the rainfall field from the next timestamp yields the optimal advection vector.

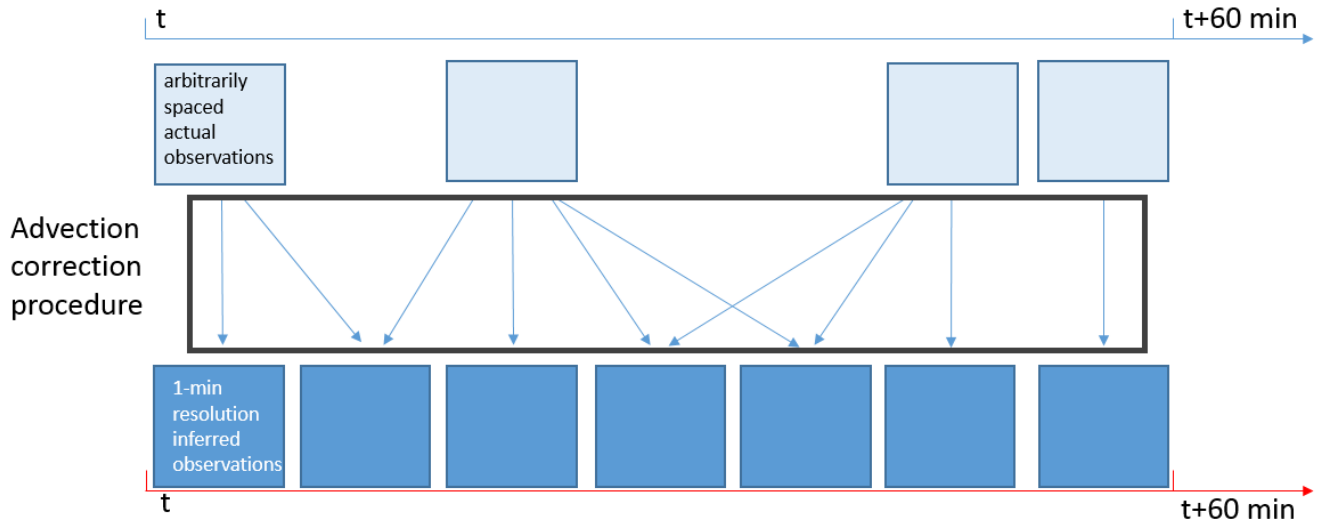

Figure D.1: Schematic representing the Advection-correction routine, where data is created on a uniform time interval.

Using calculated advection vectors described above, gaps in temporal observations were "filled in" by interpolating the rainfall field's movement over the gap in observation, shown as a schematic diagram in Figure D.1. The process scales the vector in relation to the latency between rainfall observations. When observations are available before and after a particular time, the process assigns weights to the contribution to the estimate by the proximity in time relative to the previous and next radar observation. Timestamps before the first observation in the event are estimated by advecting backward in time from the first observation of the event. Timestamps after the last observation are estimated by advecting forward in time from the last observation. The process repeats for both radars in the network, with independent sets of advection vectors.

Appendix E. Spatial Merging

The literature provides examples of merging data from networks of radars. (Ryzhkov et al., Diederich et al.) This approach is especially useful at X-band, where localized heavy rainfall can attenuate the returning radar pulse. However, a radar network can overcome some of these shortcomings. At grid locations with overlapping coverage, the process assigned simple averages of the radar estimates to each cell. Locations covered by at least one radar were assigned the accumulation value from the radar providing coverage. Points on the grid without coverage were left at zero accumulation.

A standardized observation interval is necessary for spatially merging a network of radar observations, which may not necessarily record at the same time. A schematic is given in Figure E.1, which illustrates the accumulation process once they are brought to a uniform observation interval.

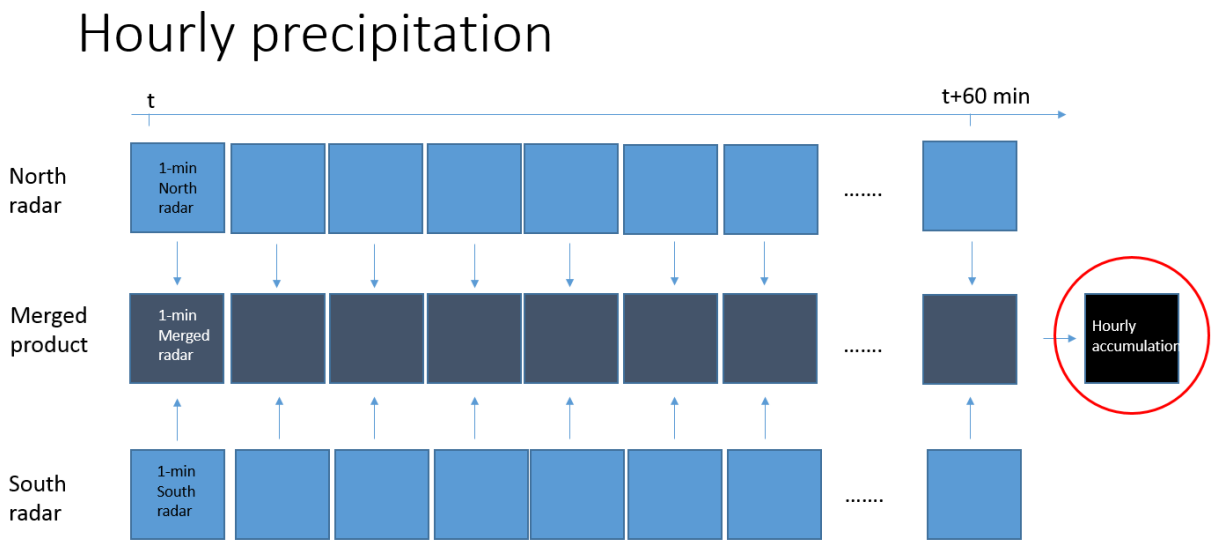

Figure E.1: Schematic representing the merging of Advect-corrected data from both radars onto one shared domain.

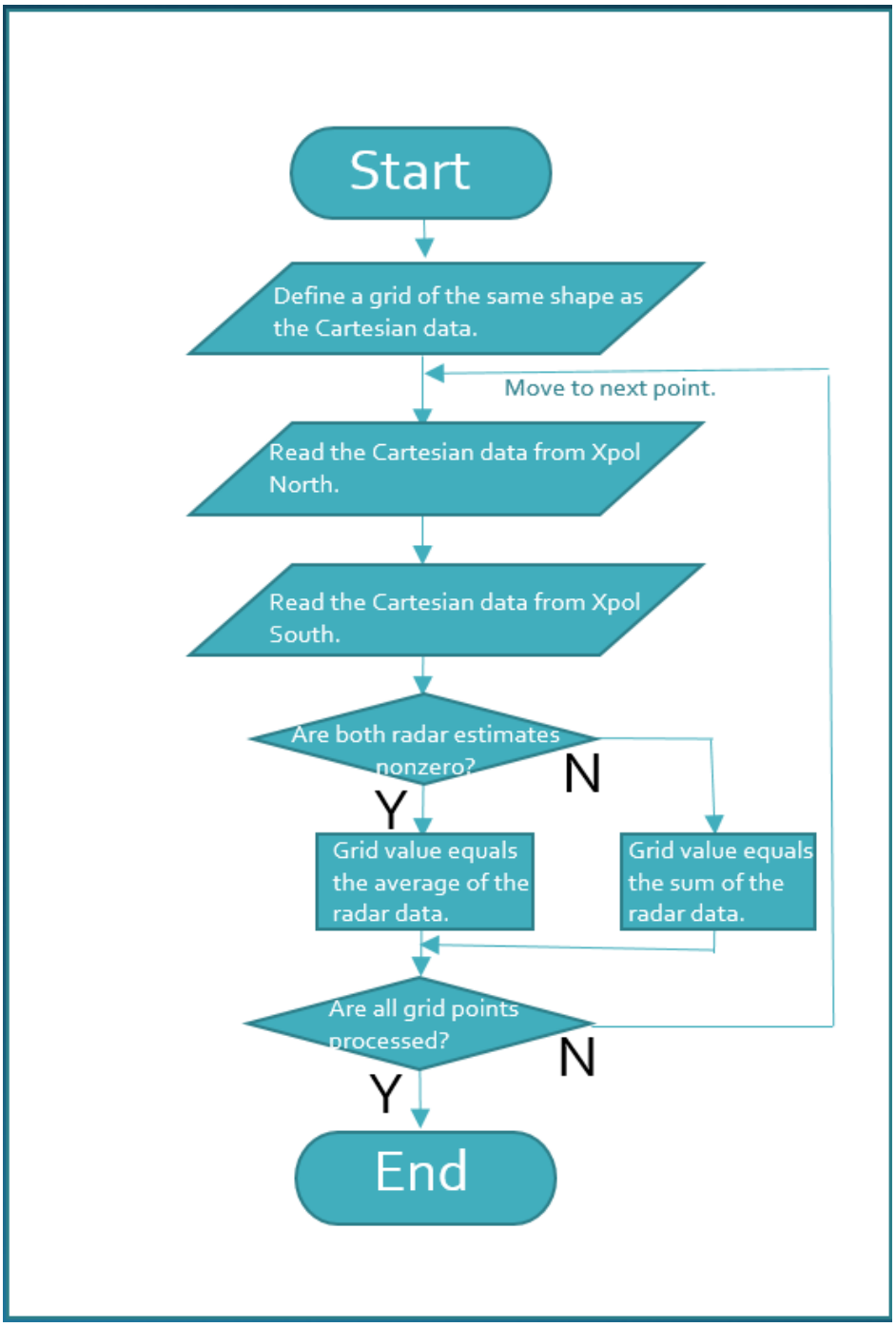

Figure E.2: Procedure for mosaicking data from the two Xpol radars.

Appendix F. Scanning Capability of the Xpol Radar Network

Knowing the spatial extent of rainfall, and its variability across the domain is crucial for most hydrological studies. The majority of radar scans during the SMAP campaign were plan-position-indicator [PPI] scans. These map a spatial location, a range and an azimuth angle, to a rainfall moment. The result is a 2-D map of rainfall with range resolution of 75m and 1 degree, observed once every 2.5 minutes. Since the Xpol radar units are mounted on trailers, their antennae are never more than 3m above the ground. Therefore, the elevation angle was selected to alternate between 3 and 4 degrees.

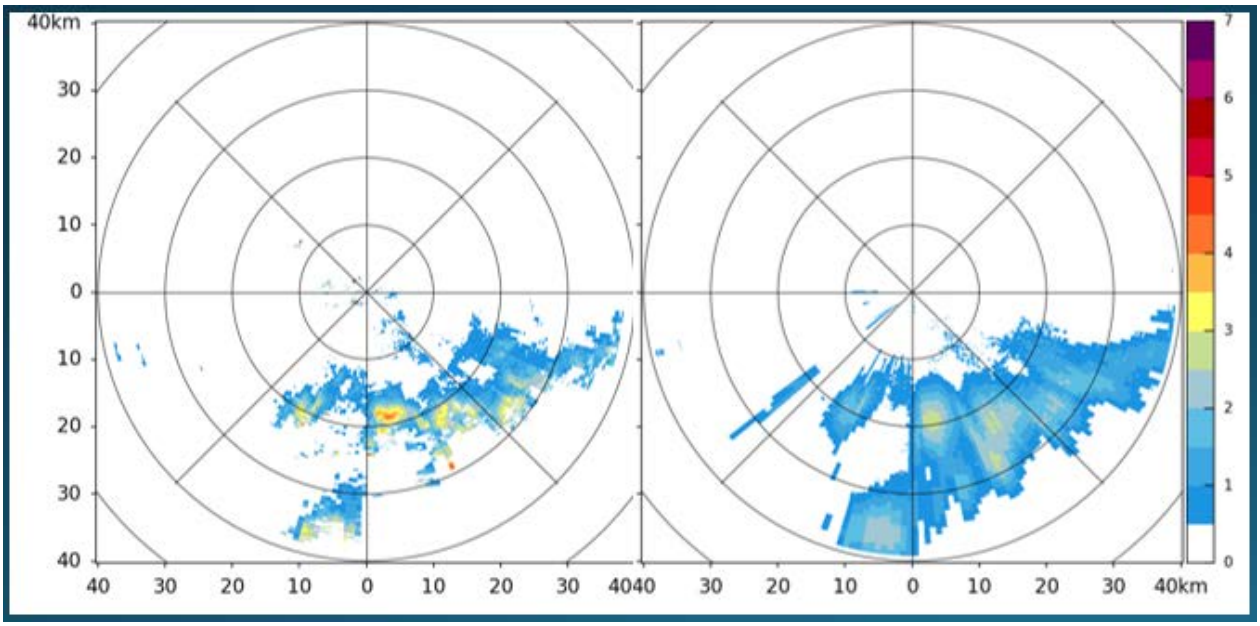

Figure F.1: Side-by-side examples of PPI scans, showing the rainfall rate (in/hr) from Kalman Filtering K_{dp} (left) and K_{dp} estimated from results of a FIR filter (right). Xpol North is at the center of each PPI plot.

Radar RHI Scans: Cross Sections of the Storm

In addition to the vertical scans, the Xpol radars were programmed to point toward one another, and scan from 0 to 18 degrees. This produces a scan which sheds information on the vertical profile of storms, known as a range-height indicator or RHI scan. Figure F.2 shows an example of these scans, 4 minutes apart, and simultaneous scans during rainfall were rare during the campaign, as the radar software did not easily allow synchronization of independent radar systems.

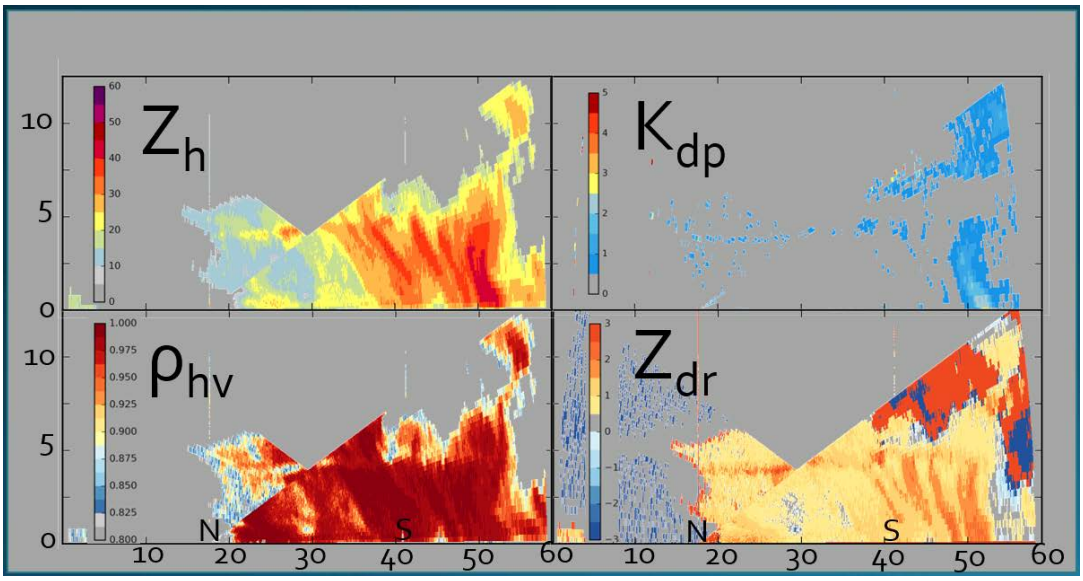

Figure F.2: RHI scans of a Convective line changing into a stratiform rainfall event. The x and y axes are in kilometers. 'N' denotes the location of Xpol North, and 'S' Xpol South.

Quality Control: Vertical and Solar Scans

Proper calibration is a vital aspect to estimating rainfall using amplitude-based dual-pol radar products. The radars in the SMAPVEX 16 experiment were calibrated by scanning vertically during a rainfall event. Since the purpose of dual-pol is to identify anisotropy in raindrops, scanning vertically, in theory, allows for a reference condition. From a ground-

perspective looking up, falling raindrops should appear to the radar as mostly round, with no systematic deviations, independent of azimuth angle. So, in many radar scans in phase 2, the antennas of both radars were pointed upward, rotated 360 degrees, and returned to normal operation.

Since this is a system-wide calibration technique, the results represent the sum of all calibration issues from transmission, to backscatter, to reception and processing. Vertical calibration results for both radars are depicted in Figures F.3 and F.4. Results from Xpol North indicate that the vertical channel observes more power than the horizontal channel, by more than 3 dB. The discrepancy for Xpol South is less than 0.5 dB. The noise in this vertical return signal was also investigated. To answer the question of whether clear-sky, or very heavy rainfall created bias in the calibration estimate, the Zdr estimates from the vertical scans were sorted by how intense the rainfall was, from very light to very heavy. This result is depicted in Figure F.5.

The results show that the dispersion is least in moderate rainfall, around 30 dbZ of reflectivity. At higher rainfalls, and when ice is mixed into the rain volume, the variability increases. At low rainfall rates, where just large cloud-droplets may be present, the variability rises again, where influence can come from dust particles, or side lobe interactions returning to the antenna. Despite the changes in dispersion, however, the central tendency of the Zdr value for a vertical scan stays consistent for different rainfall intensity levels.

Investigating the available vertical scans taken during rainfall, the discrepancy was found to vary from -2.5 dB to -4 dB, with the vertical channel reporting more power than the horizontal channel consistently. This behavior was found to correlate strongly to the magnetron temperature, Figure F.6, which was sometimes difficult to stabilize remotely. For the phase 2 data, the radar constants were adjusted in the data processing steps to account for the measured

channel discrepancies. For this reason, reflectivity and differential reflectivity are not recommended for use in estimating accumulated rainfall.

Later on in July of 2018, solar calibration was applied to the Xpol radars to investigate the calibration of the receiving system. The sun's earth-facing disc served as a source of unpolarized microwave radiation. Figure F.7 shows Xpol South had a channel discrepancy of around -0.2 dB on the receiving end.

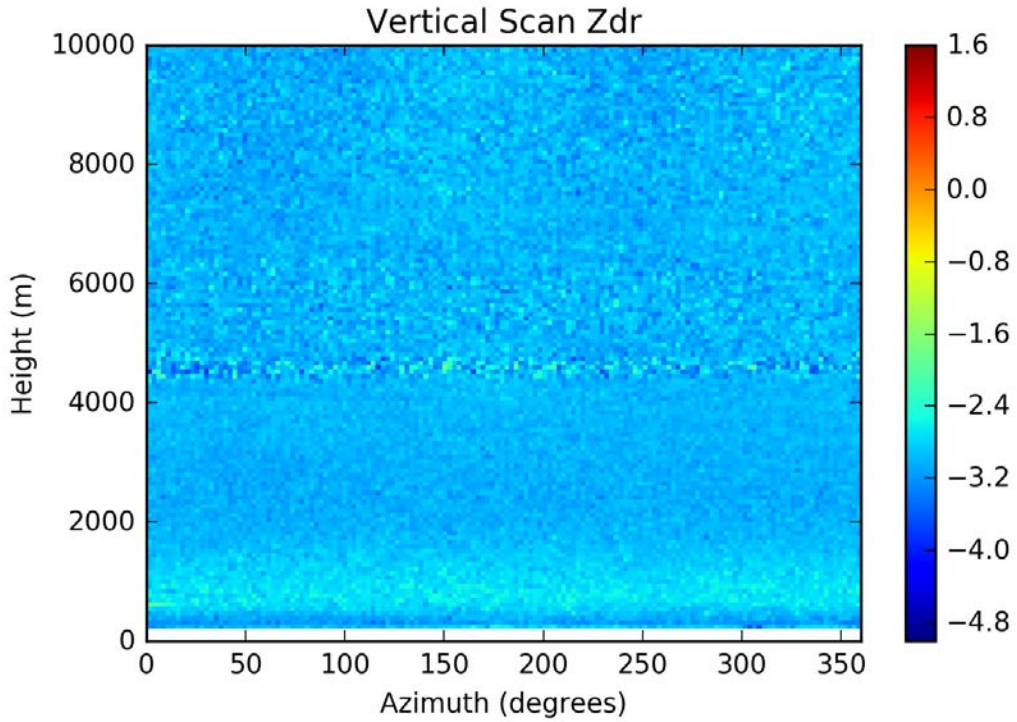

Figure F.3: Vertical Zdr calibration of Xpol North in stratiform rain, 2:00:26 UTC Aug. 12, 2016.

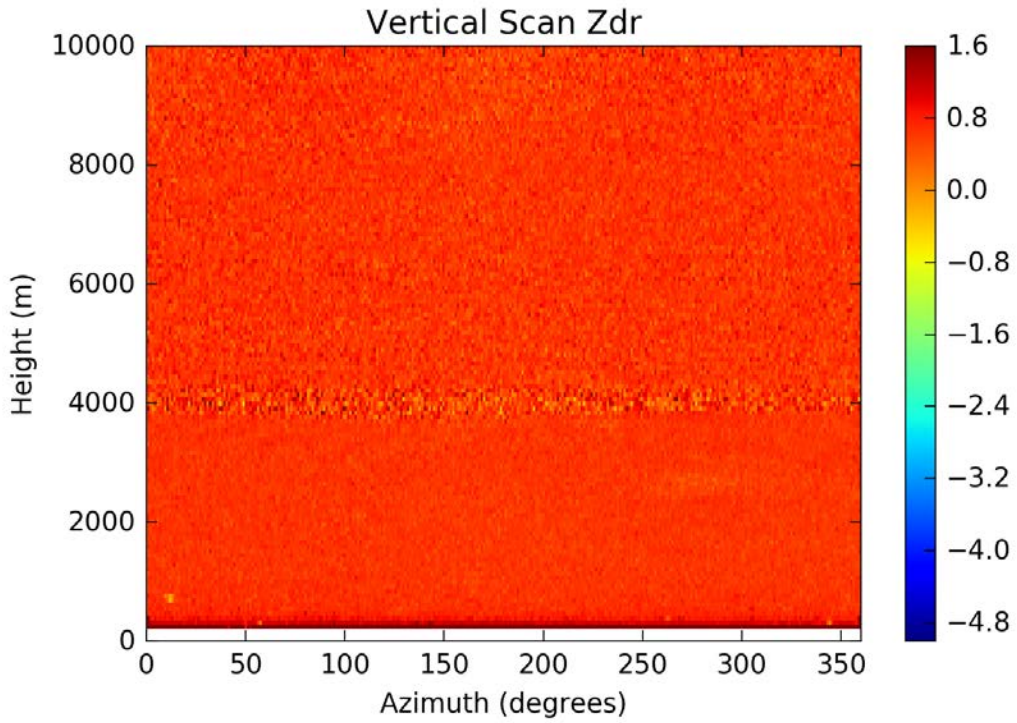

Figure F.4: Vertical Zdr calibration of Xpol South in stratiform rain, 2:42:01 UTC Aug. 12, 2016.

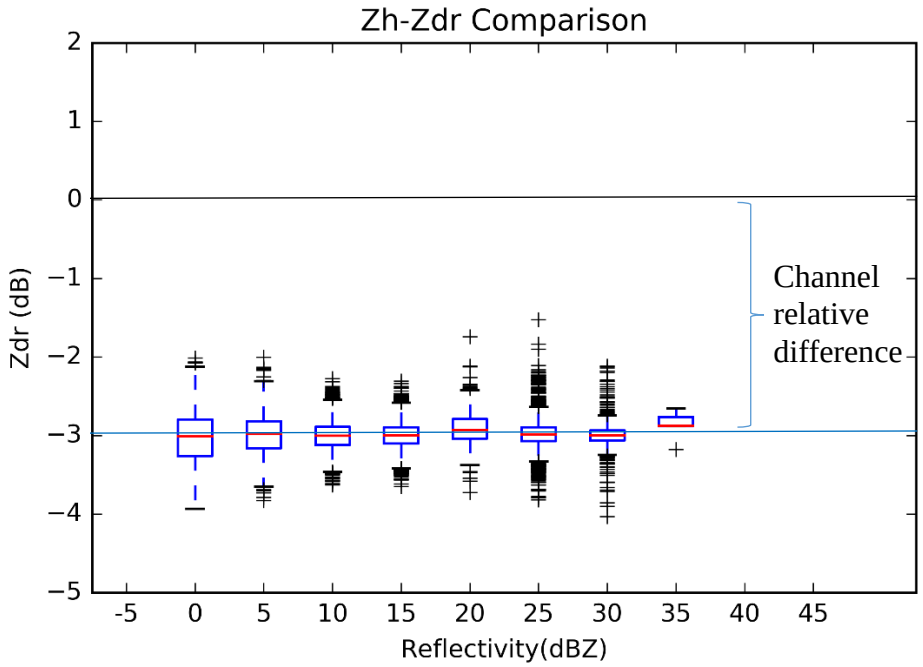

Figure F.5: Dispersion of raw vertically-scanned Zdr as a function of vertically-scanned Reflectivity on Xpol North, 2:42:01 UTC Aug. 12, 2016.

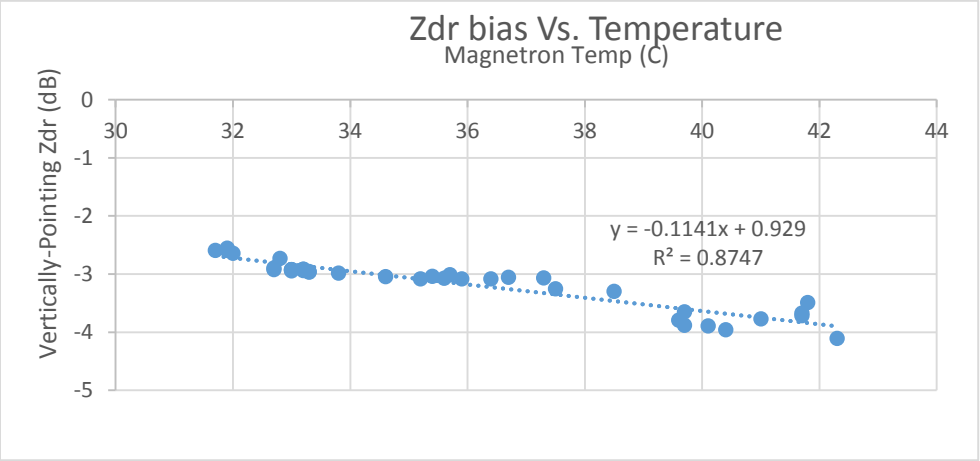

Figure F.6: Median Vertically-Pointing Zdr, from at least 1000 observations with reflectivity greater than 20 dBZ, measured by Xpol North during rain events, as a function of magnetron temperature.

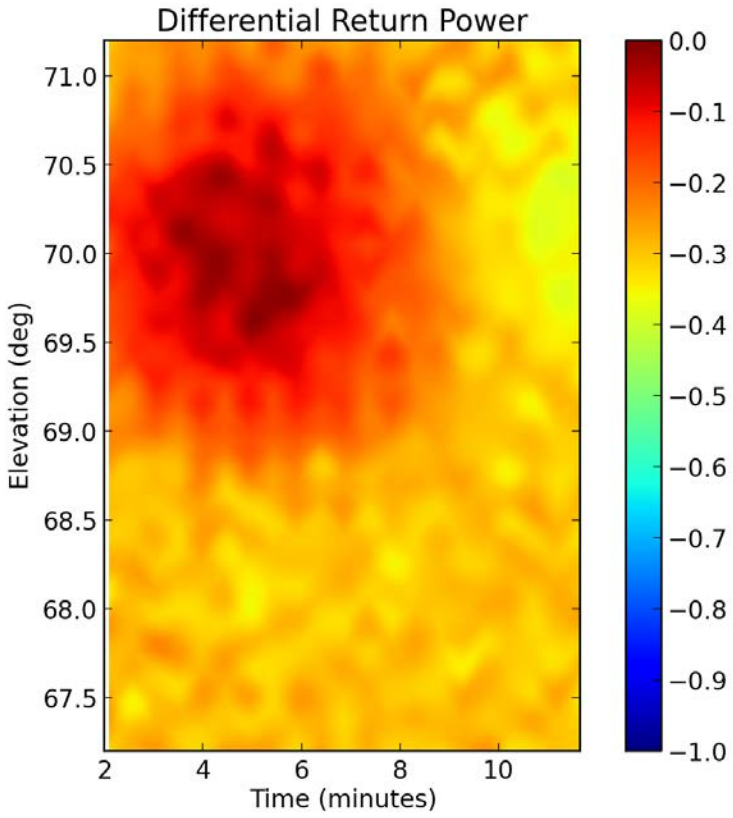

Figure F.7: Result of Solar calibration (sun in upper left) for Xpol South, in July 2018. At maximum intensity, assuming unpolarized solar light, the receiving channels were within 0.2 dB.

Appendix G. Interactive Radar Browser

An environment using the Google Maps API was assembled to act as a tool for quickly checking the performance of the various parts of the radar-rainfall algorithms. This website is capable of displaying data files from the SMAPVEX-16 campaign, projected over the experimental domain. Reflectivity, Z_{dr}, Φ_{dp} (see Figure G.2), ρ_{hv}, K_{dp}, and specific attenuation rainfall rate can be plotted in the browser for quick comparison. The rain gauge locations, the watershed boundaries, and the river network can be overlaid for an enhanced visualization of the rainfall system. This system consists of a JavaScript code, which calls python scripts to process the data, and return the graphical results to the browser.

Then, the browser methodically draws, polygons over locations in the domain, with color corresponding to the numerical value of the selected radar product. Figures G.2, G.4, and G.5 indicate the spatial extent of the scanning sectors of the radar units, covering the watershed boundaries entirely. One can also notice the gauges that lie outside the watershed boundaries, or outside the scanning sector of one of the radars. This website lives on the IIHR server 50. http://s-iihr50.iihr.uiowa.edu/rpdb/is/index.html?exp_id=1

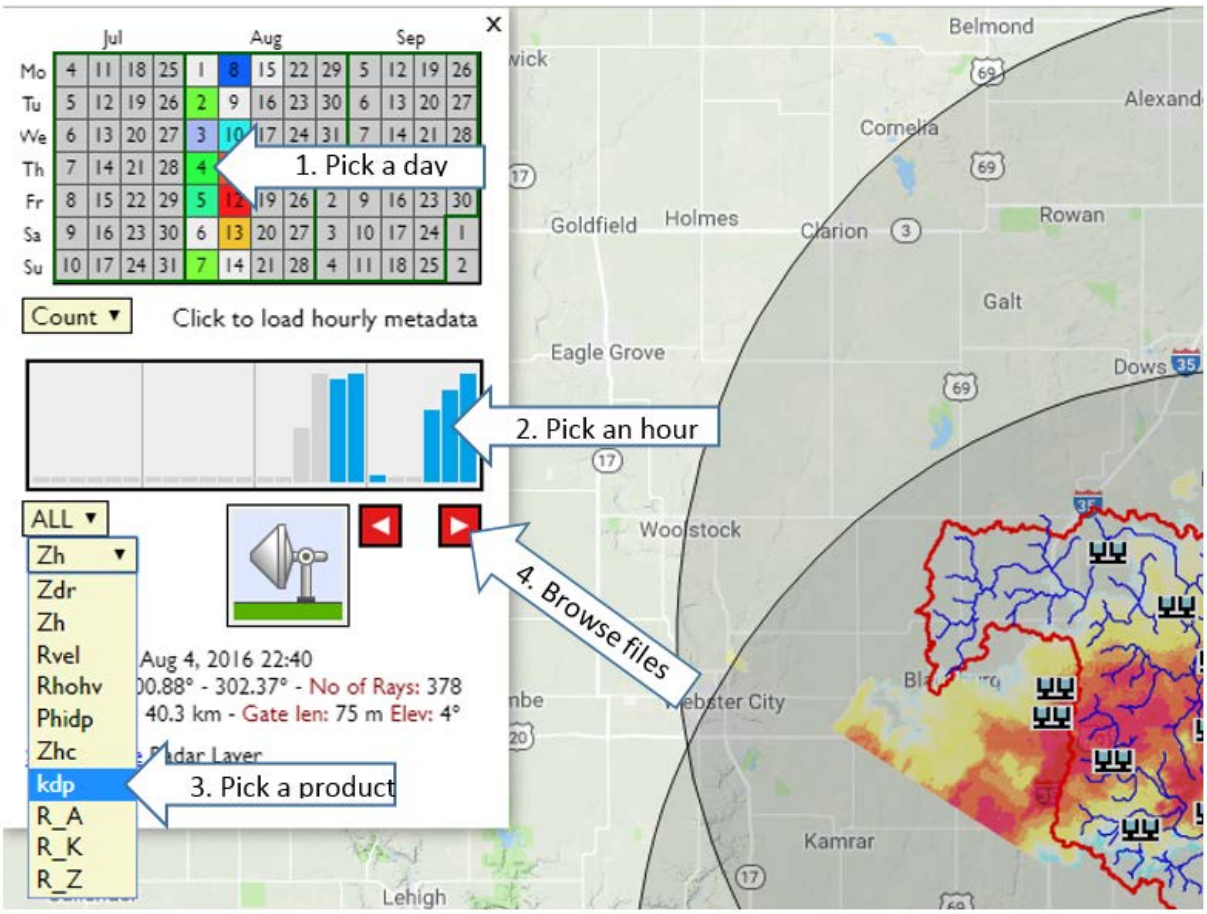

Figure G.1: The control panel for the radar Browser.

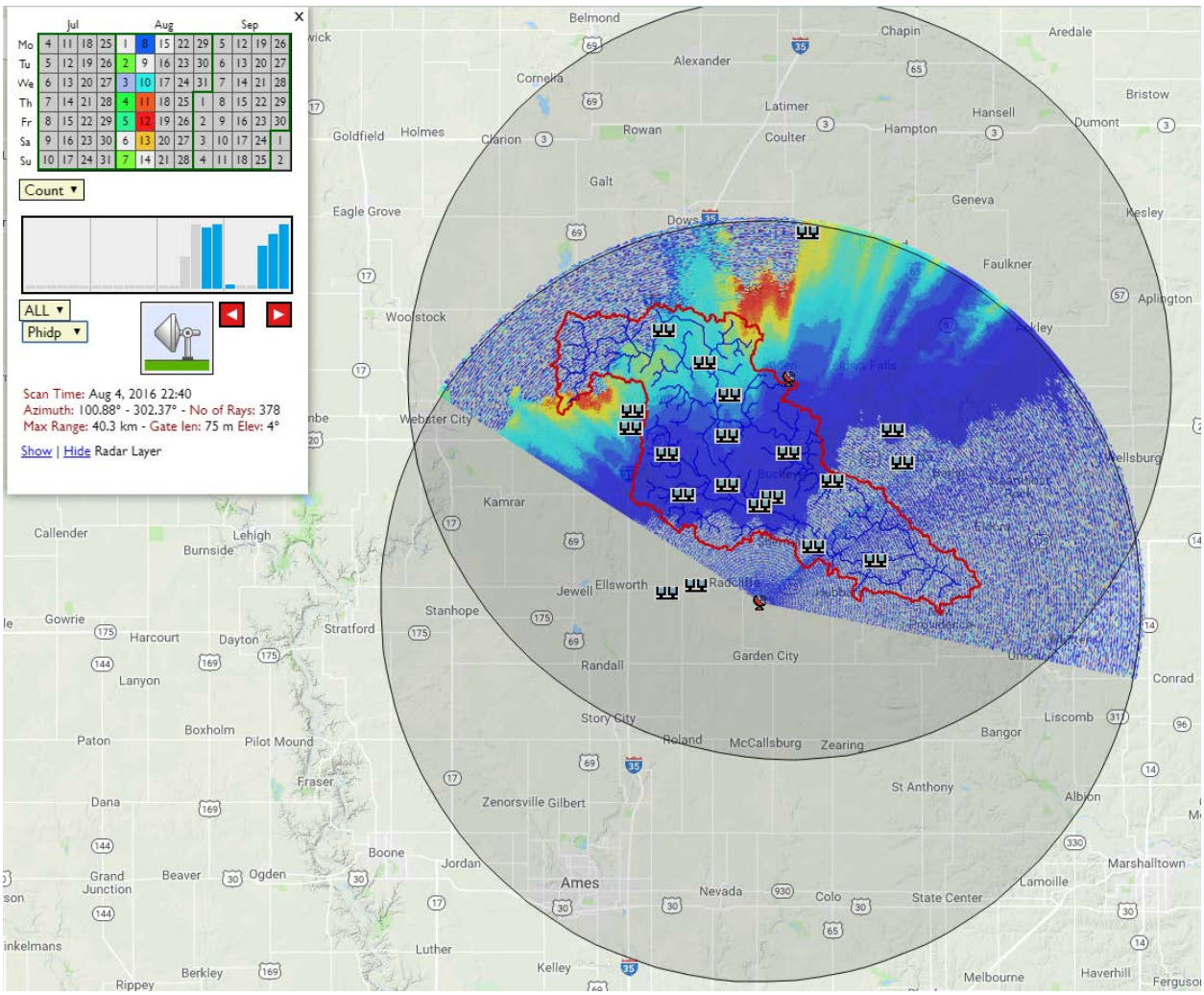

Figure G.2: A plot of Φdp from Xpol South during a convective line of thunderstorms August 4, 2016.

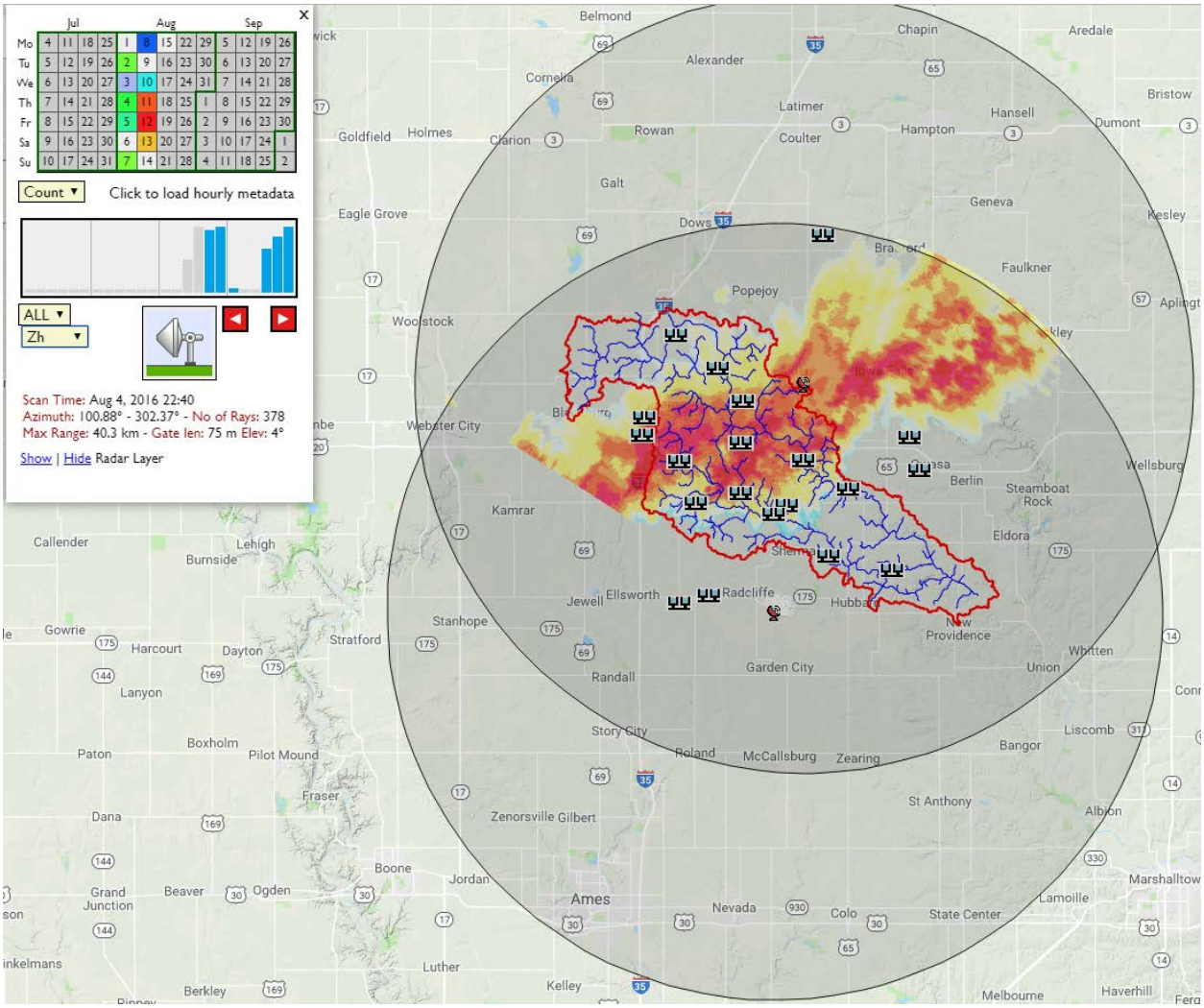

Figure G.3: A plot of Reflectivity from Xpol South during the same storm as Figure G.2.

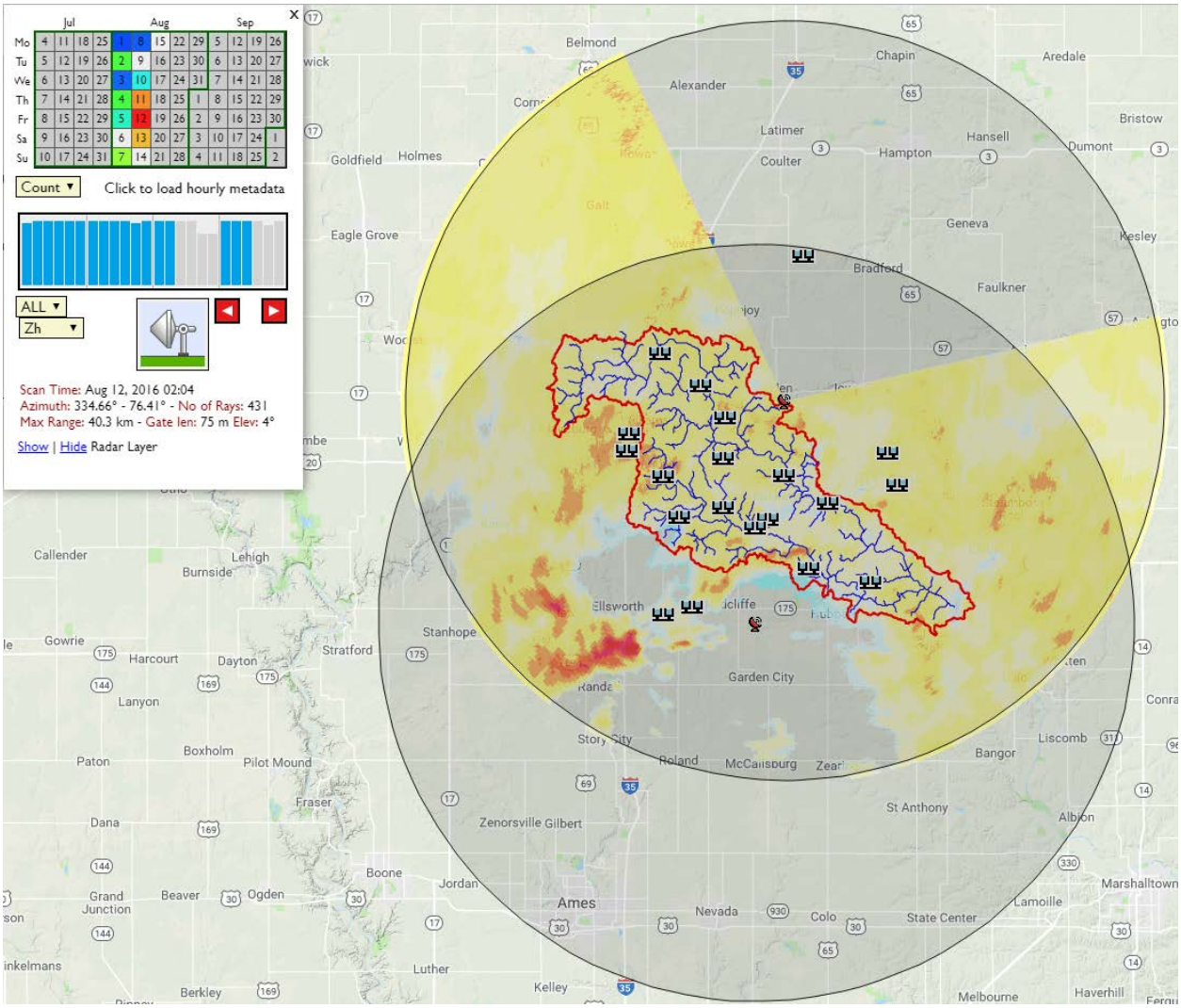

Figure G.4: A plot of reflectivity from Xpol North from stratiform rainfall on August 12, 2016.

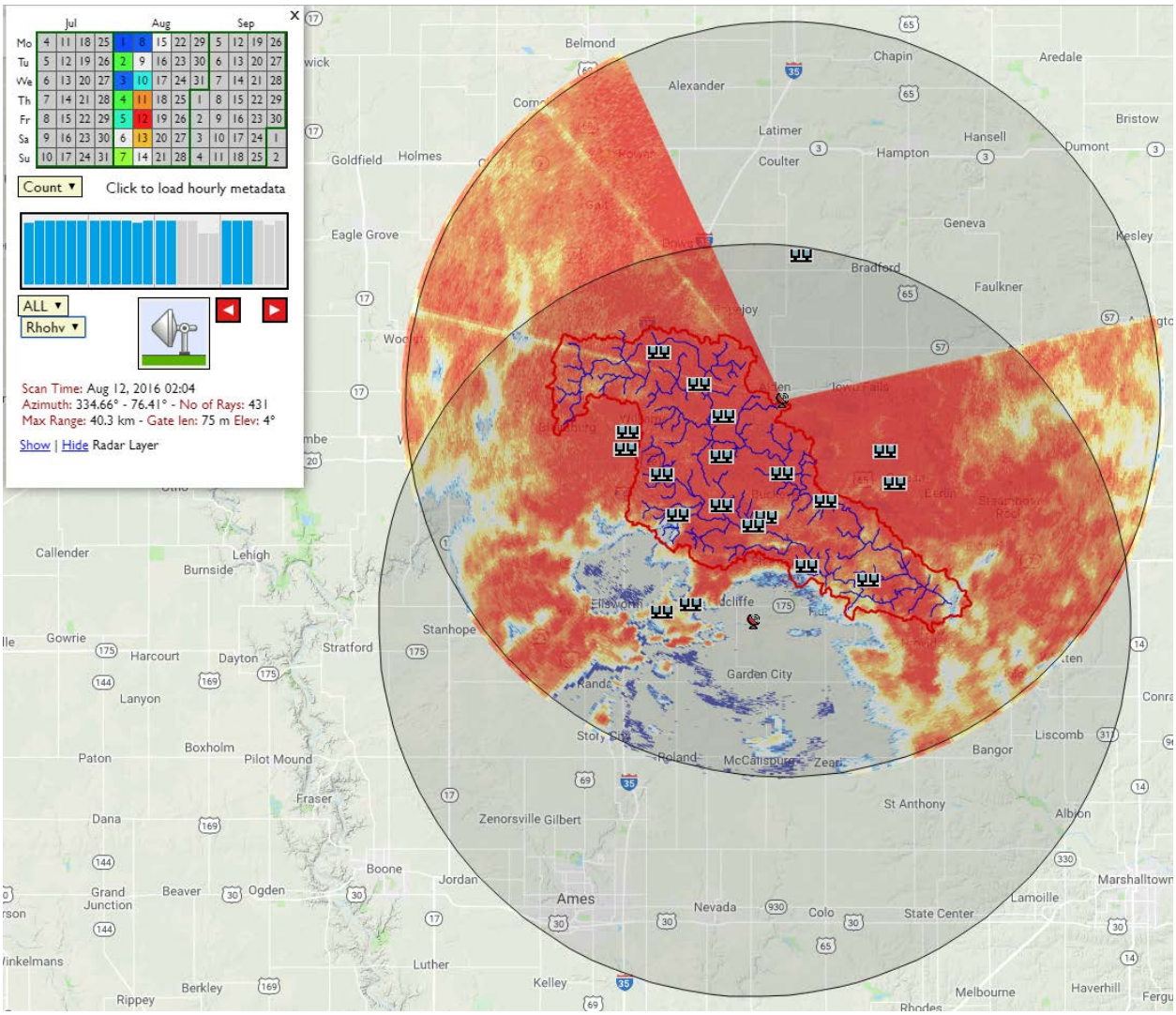

Figure G.5: A plot of ρhv from the same storm as in Figure G.4. The linear streaks indicate the presence of partial beam blockage